SIDE FORCES ON A TANGENT OGIVE FOREBODY WITH A FINENESS RATIO OF 3.5 AT HIGH ANGLES OF ATTACK AND MACH NUMBERS FROM 0.1 TO 0.7

Earl R. Keener, Gary T. Chapman,
Lee Cohen, and Jamshid Taleghani

Ames Research Center
Moffett Field, Calif. 94035

1. Report No. NASA TM X-3437	2. Government Accession No.	3. Recipient's Catalog No.
4. Title and Subtitle SIDE FORCES ON A TANGENT OGIVE FOREBODY WITH A FINENESS RATIO OF 3.5 AT HIGH ANGLES OF ATTACK AND MACH NUMBERS FROM 0.1 TO 0.7		5. Report Date February 1977
		6. Performing Organization Code
7. Author(s) Earl R. Keener, Gary T. Chapman, Lee Cohen, and Jamshid Taleghani		8. Performing Organization Report No. A-6609
		10. Work Unit No. 505-06-95
9. Performing Organization Name and Address Ames Research Center Moffett Field, California 94035		11. Contract or Grant No.
		13. Type of Report and Period Covered Technical Memorandum
12. Sponsoring Agency Name and Address National Aeronautics and Space Administration Washington, D.C. 20546		14. Sponsoring Agency Code

15. Supplementary Notes

16. Abstract

An experimental investigation was conducted in the Ames 12-Foot Wind Tunnel to determine the subsonic aerodynamic characteristics, at high angles of attack, of a tangent ogive forebody with a fineness ratio of 3.5. The investigation included the effects of nose bluntness, nose strakes, nose booms, a simulated canopy, and boundary-layer trips. The forebody was also tested with a short afterbody attached. Static longitudinal and lateral-directional stability data were obtained at Reynolds numbers ranging from 0.3×10^6 to 3.8×10^6 (based on base diameter) at a Mach number of 0.25, and at a Reynolds number of 0.8×10^6 at Mach numbers ranging from 0.1 to 0.7. Angle of attack was varied from 0° to 88° at zero sideslip, and the sideslip angle was varied from $-10°$ to 30° at angles of attack of 40°, 55°, and 70°.

The investigation was particularly concerned with the possibility of large side forces and yawing moments at high angles of attack at zero sideslip. It was found that a side force occurs, starting at angles of attack of about 33° and continuing to angles of attack as high as 80°. The side force is as large as 1.5 times the maximum normal force; the side force is repeatable with increasing and decreasing angle of attack and from test to test. The maximum side force varies considerably with Reynolds number and decreases to near zero as the Mach number increases to 0.7. The side force is very sensitive to the nature of the boundary layer as indicated by large changes with boundary layer trips. The direction and magnitude of the side force is sensitive to the body geometry near the nose. Rotating the nose tip changes the direction of the side force; nose booms and boundary-layer trips near the nose tip significantly reduce the side force, and nose strakes and small bluntness tend to eliminate the side forces. The angle of attack at which onset of side force occurs is not strongly influenced by either Reynolds number or Mach number. The short afterbody reduces the angle of onset by about 5°. Maximum normal force occurs at angles of attack near 60°, rather than at 90°.

17. Key Words (Suggested by Author(s)) Aerodynamic characteristics Subsonic Bodies High angle of attack Side forces	18. Distribution Statement Unlimited STAR Category — 02		
19. Security Classif. (of this report) Unclassified	20. Security Classif. (of this page) Unclassified	21. No. of Pages 114	22. Price* $5.25

NOMENCLATURE

The data are presented in the body axis coordinate system with the moment center located at the base of the forebody models. Since the data were computer plotted, the corresponding plot symbol, where used, is given together with the conventional symbol.

Conven-tional Symbol	Plot Symbol	Definition
C_A	CA	axial-force coefficient, $\dfrac{\text{balance axial force}}{qS}$
C_{AF}	CAF	axial-force coefficient adjusted for base pressure equal to free-stream static pressure, $(C_A + C_{p,b})$
C_m	CLM	pitching-moment coefficient, $\dfrac{\text{pitching moment}}{qSd}$
$C_{m,R}$	CRM	resultant-moment coefficient, $(C_n \sin \Psi + C_m \cos \Psi)$
C_N	CN	normal-force coefficient, $\dfrac{\text{normal force}}{qS}$
C_n	CYN	yawing-moment coefficient, $\dfrac{\text{yawing moment}}{qSd}$
CP_R	CPR	resultant-force center of pressure location, fraction of length, ℓ, from nose tip, $\quad 1 - \dfrac{C_{m,R}}{C_R}\dfrac{d}{\ell}$
$C_{p,b}$	CPB	base pressure coefficient, $\dfrac{p_b - p}{q}$
C_R	CR	resultant-force coefficient in body axis system, $\sqrt{C_N^2 + C_Y^2}$
C_Y	CY	side-force coefficient, $\dfrac{\text{side-force}}{qS}$
$|C_Y|$	ACY	absolute value of C_Y
d	D	base diameter, 15.24 cm
ℓ	L	length of forebody, 53.3 cm
M	MACH	free-stream Mach number
p		free-stream static pressure
p_b		base pressure

iii

Conventional Symbol	Plot Symbol	Definition
q		free-stream dynamic pressure
R_d	R	Reynolds number, based on model base diameter
S	S	area of forebody base
x		distance behind forebody apex along body axis
α	ALPHA	angle of attack, deg
β	BETA	angle of sideslip, deg
Θ	THETA	meridian angle measured from bottom center line; right side is positive looking upstream
ϕ_B	PHI-B	roll angle of model forebody about body axis of symmetry; clockwise is positive looking upstream
ϕ_N	PHI-N	roll angle of removable nose alone about axis of symmetry; clockwise is positive looking upstream
ψ	PSI	angle between the resultant and normal forces, resultant force inclined to the right is positive angle looking upstream, $\tan^{-1} \dfrac{C_Y}{C_N}$

Model Configuration Code

AA	afterbody attached to forebody
AD	afterbody detached from forebody (separated by 0.16 cm gap), but attached to sting
B1	nose boom, length = 2.54 cm
B2	nose boom, length = 5.08 cm
C	canopy
FT1	tangent-ogive forebody, $\dfrac{\ell}{d} = 3.5$
NB1	blunt nose, radius = 0.317 cm
NB2	blunt nose, radius = 0.635 cm
NB3	blunt nose, radius = 1.27 cm
NS	sharp nose, radius = 0

Plot Symbol	Definition
NSB1	sharp nose with 0.32 by 2.54 cm nose boom
NST1	sharp nose with 0.32 cm wide strake
NST2	sharp nose with 0.64 cm wide strake
NST3	sharp nose with 1.27 cm wide strake
T2	boundary-layer transition strip along forebody meridian, $\theta = \pm15°$, full length
T4	boundary-layer transition strip along forebody meridians, $\theta = \pm30°$, full length
T4R	boundary-layer transition strip along forebody meridian on right side, $\theta = 30°$, full length
T5	boundary-layer transition strip along forebody meridians, $\theta = \pm30°$, 2/3 body length
T6	boundary-layer transition strip along forebody meridians, $\theta = \pm30°$, 1/3 body length
T7	boundary-layer transition strip along forebody meridians, $\theta = \pm60°$, full length
T8	boundary-layer transition strip encircling model, $\frac{x}{\ell} = 0.05$
T9	boundary-layer transition strip encircling model, $\frac{x}{\ell} = 0.09$
T10	boundary-layer transition strip encircling model, $\frac{x}{\ell} = 0.14$
T11	boundary-layer transition strip encircling model at junction of nose and forebody, $\frac{x}{\ell} = 0.19$
T12	boundary-layer transition strip encircling model, $\frac{x}{\ell} = 0.28$

SIDE FORCES ON A TANGENT OGIVE FOREBODY WITH A FINENESS RATIO

OF 3.5 AT HIGH ANGLES OF ATTACK AND MACH NUMBERS

FROM 0.1 TO 0.7

Earl R. Keener, Gary T. Chapman, Lee Cohen, and Jamshid Taleghani

Ames Research Center

SUMMARY

An experimental investigation was conducted in the Ames 12-Foot Wind Tunnel to determine the subsonic aerodynamic characteristics, at high angles of attack, of a tangent ogive forebody with a fineness ratio of 3.5. The investigation included the effects of nose bluntness, nose strakes, nose booms, a simulated canopy, and boundary-layer trips. The forebody was also tested with a short afterbody attached. Static longitudinal and lateral-directional stability data were obtained at Reynolds numbers ranging from 0.3×10^6 to 3.8×10^6 (based on base diameter) at a Mach number of 0.25, and at a Reynolds number of 0.8×10^6 at Mach numbers ranging from 0.1 to 0.7. Angle of attack was varied from $0°$ to $88°$ at zero sideslip, and the sideslip angle was varied from $-10°$ to $30°$ at angles of attack of $40°$, $55°$, and $70°$.

The investigation was particularly concerned with the possibility of large side forces and yawing moments at high angles of attack at zero sideslip. It was found that a side force occurs, starting at angles of attack of about $33°$ and continuing to angles of attack as high as $80°$. The side force is as large as 1.5 times the maximum normal force; the side force is repeatable with increasing and decreasing angle of attack and from test to test. The maximum side force varies considerably with Reynolds number and decreases to near zero as the Mach number increases to 0.7. The side force is very sensitive to the nature of the boundary layer as indicated by large changes with boundary layer trips. The direction and magnitude of the side force is sensitive to the body geometry near the nose. Rotating the nose tip changes the direction of the side force; nose booms and boundary-layer trips near the nose tip significantly reduce the side force, and nose strakes and small bluntness tend to eliminate the side force. The angle of attack at which onset of side force occurs is not strongly influenced by either Reynolds number or Mach number. The short afterbody reduces the angle of onset by about $5°$. Maximum normal force occurs at angles of attack near $60°$, rather than at $90°$.

INTRODUCTION

When bodies of revolution are pitched to high angles of attack, a side force can occur at zero sideslip angle. This side force results when the separation induced vortex flow field on the lee side of the body becomes asymmetric. The occurrence of asymmetric body vortex flow has been observed for many years (refs. 1 and 2). Research on this phenomenon has increased considerably in recent years with the advent of highly maneuverable aircraft because the side force and yawing

moment might contribute to the onset of aircraft spin (ref. 3). To date, much of the research on asymmetric forces has been directed toward determining fixes for specific configurations and on studies of vortex flow fields on long slender bodies (e.g., refs. 4-9). However, a recent test of three forebody models at low Mach number and low Reynolds numbers (ref. 10) showed that large side forces can be generated on the forebody alone at zero sideslip.

Since the configuration of the forebody might play an important role in the spin characteristics of aircraft, a comprehensive wind tunnel test program has been undertaken at Ames Research Center to obtain static aerodynamic data for forebody-alone models, covering a wide range of forebody shapes and a wide range of Reynolds numbers and Mach numbers. The objective was to determine the effect of forebody on the forces and moments so that design criteria could be established for aircraft and missiles that have good aerodynamic characteristics at high angles of attack. Reports thus far generated from this test program are listed in references 11 to 13.

As part of the forebody test program, aerodynamic force and moment characteristics were measured at subsonic speeds over a large range of Reynolds numbers for a tangent-ogive forebody with a fineness ratio of 3.5. Previous tests conducted on an identical forebody at low speed and low Reynolds number (ref. 10) showed the existence of side forces and yawing moments at zero sideslip. The objectives of the present investigation were to determine the test conditions under which the side forces occur and the effects of hysteresis, repeatability, roll position, sideslip, boundary layer trips, nose bluntness, nose strakes, nose booms, and a simulated canopy. In addition, to determine the effects of the flow around the base of the forebody-alone configuration, the forebody was tested in the presence of an $\ell/d = 3.5$ cylindrical afterbody. The forebody was also tested with the afterbody attached to determine the effect on the side force of a short afterbody.

The investigation was conducted in the Ames 12-Foot Pressure Wind Tunnel; the tests covered a Mach number range from 0.1 to 0.7 and a Reynolds number range from 0.3×10^6 to 3.8×10^6 (based on model base diameter). Six-component static forces and moments were measured at angles of attack from $0°$ to $88°$.

This report presents the basic data that show the effects on the aerodynamic characteristics of the various model configurations, of Reynolds number at a Mach number of 0.25, and of Mach number up to 0.7. Selected results from this investigation were reported in reference 11.

TEST FACILITY

The aerodynamic data presented here were obtained from wind tunnel tests conducted in the Ames 12-Foot Pressure Wind Tunnel. This tunnel is a variable-pressure, low-turbulence facility with a Mach number range from 0.1 to about 0.9 and a unit Reynolds number capability up to about 26×10^6/m at a Mach number of 0.25. Eight fine-mesh screens in the settling chamber, together with a contraction ratio of 25 to 1, provide an airstream of exceptionally low turbulence.

MODEL DESCRIPTION

The forebody model is a tangent ogive with a fineness ratio (ℓ/d) of 3.5, a length of 53.3 cm, and a base diameter of 15.24 cm. A sketch of the model and its dimensions is shown in figure 1. Photographs of the models and tunnel installation are shown in figure 2. The forebody was designed with removable nose sections of various nose radii up to 1.27 cm. The model also had the following characteristics: a sharp nose with a longitudinal slot starting 1.9 cm behind the tip to accommodate short strakes (7.9 cm long), two nose booms for the sharp and blunt noses, and a simulated canopy. An $\ell/d = 3.5$ afterbody was designed to be clamped to the sting but to be free of the forebody (approximately 0.16 cm gap) so that forebody forces could be measured in the presence of the afterbody. The afterbody could also be attached to the forebody (forebody plus afterbody force). The junctions between the removable nose and the forebody and afterbody were carefully machined, so that the surface discontinuity was less than 0.025 mm, and had rearward facing steps. The removable nose sections were held by a set screw located on the leeward side and covered with carefully smoothed dental plaster. A balance-pin-access hole, located on the leeward side, was also covered with smoothed dental plaster. The afterbody was built in two halves; the parting surface was oriented perpendicular to the windward side so that the retaining bolt holes were located on the windward side. The bolt holes and the small gap on each side between the cylindrical halves were filled with smoothed dental plaster.

TEST CONDITIONS AND PROCEDURES

The investigation was conducted at Reynolds numbers ranging from 0.3×10^6 to 3.8×10^6 (based on base diameter) at a Mach number of 0.25, and at a Reynolds number of 0.8×10^6 at Mach numbers ranging from 0.1 to 0.7. The models were mounted from a floor support system that provided a high angle of attack range. Since it was not possible to pitch the model continuously from $\alpha = 0°$ to $88°$, two different sting supports were used (fig. 2). The sting shown in figure 2(b) was used for $\alpha = 0°$ to $45°$ and the sting shown in figure 2(c) was used for $\alpha = 36°$ to $88°$. Angle of sideslip was varied from $-10°$ to $30°$ at $\alpha = 40°, 55°,$ and $70°$.

Aerodynamic forces and moments on the model were measured using two internal six-component strain gage balances with two ranges. Most of the data were obtained on a balance with a normal-force range of ±8000 N; this balance was required for the large Reynolds number range, including at least 30 percent reserve for dynamic forces. The second balance (referred to as balance B) had a lower normal-force range of ±4500 N and was used to check the validity of the results at the lower Reynolds numbers. The model base pressure was measured using one pressure tube that was attached to the sting and opened into the balance cavity at the base of the model. For tests of the forebody in the presence of the afterbody, the open end of the pressure tube was located in the gap between the forebody and afterbody.

The $\ell/d = 3.5$ tangent-ogive forebody was first tested without the afterbody. Tests were made with pointed and blunt noses, with the narrowest nose strake, and with several positions of boundary-layer transition strips. The transition strips were 0.32 cm wide and composed of 0.021-cm diameter glass spherules (No. 80 mesh). A sublimation test was initially made at $\alpha = 55°$ with transition strips at $\Theta = \pm30°$ with the use of 0.015-cm diameter glass spherules (No. 100 mesh). This trip size was calculated to be correct for the lowest test Reynolds numbers, based on maximum

3

body diameter. The result was that the sublimation material was scrubbed off by the flow near the base of the model, indicating turbulent flow from the trips; however, about 2/3 of the model length seemed uneffected by the trips. Accordingly, the trip size was increased to 0.021 cm and a second sublimation test indicated little improvement. The trip size was not increased further because the particles near the nose might have acted to separate rather than to trip the boundary layer. In order to determine the effects of model asymmetries, both the forebody and its removable pointed nose tip were tested at several fixed roll-angle positions, generally in 90° increments.

Part of the testing of the forebody was done in the presence of the afterbody (afterbody clamped to the sting). All of the available nose configurations and the simulated canopy were tested in this configuration. Boundary-layer transition strips were tested in the positions listed in the figures and described in the configuration code. The effect of the $\ell/d = 3.5$ afterbody was determined by testing the forebody with the afterbody attached (fig. 2(d)).

DATA REDUCTION AND ACCURACY

The six-component force and moment data were reduced about the model moment-reference center in the body axis system. The moment center was located on the model centerline at the base of the forebody. Angle of attack and angle of sideslip were corrected for deflection of the sting and balance under aerodynamic load. Appropriate aerodynamic coefficients were corrected for model weight tares. Stream angles as large as 2° are known to have existed in the vicinity of the model due to the influence of the support system fairing on the tunnel floor (see fig. 2). No stream angle corrections were applied to the data. Mean values of the forces and pressures were recorded to electronic filtering and, in addition, three samples of all the balance and tunnel static pressure data were averaged for each data point and then reduced to coefficient form. The model base pressure, measured by one pressure tube, was used to compute an approximate base axial force. The base axial force was subtracted from the total balance axial-force measurement, so that the coefficient presented (C_{AF}) is for the axial force ahead of the body base.

Data repeatability was estimated by reviewing repeat points and is as follows:

$$\alpha = \pm 0.03° \qquad\qquad C_N = \pm 0.04$$
$$\beta = \pm 0.03° \qquad\qquad C_A = \pm 0.02$$
$$R = \pm 0.02 \times 10^6 \qquad\qquad C_Y = \pm 0.03$$
$$M_\infty = \pm 0.005 \qquad\qquad C_m = \pm 0.04$$
$$C_{p_b} = \pm 0.008$$

PRESENTATION OF RESULTS

The experimental results are presented in figures 3 through 26. The figures show the effects of the many configurations and of Reynolds number on the aerodynamic characteristics at $M = 0.25$,

4

and the effects of Mach number up to 0.7 at constant Reynolds number. First, the results for the forebody tested alone are compared in figure 3 to the results for the forebody tested in the presence of the afterbody. This is followed by the presentation of the aerodynamic characteristics of the forebody (figs. 4 to 24) showing the effects of hysteresis, repeatability, Reynolds number, roll position, side-slip, boundary-layer trips, bluntness, strakes, nose booms, and canopy at $M = 0.25$, and the effect of Mach number up to 0.7. Finally, the aerodynamic characteristics of the forebody with the $\ell/d = 3.5$ cylindrical afterbody attached are presented in figures 25 and 26, which show the effects of Reynolds number and Mach number.

The following coefficients were plotted and faired using a computerized data plotting program:

C_Y	CP_R and Ψ
C_N	C_n, C_m and $C_{m,R}$
$\|C_Y\|/C_N$ and $(C_R - C_N)$	$C_{p,b}$ and C_{AF}

Most of the data are plotted versus angle of attack at zero sideslip angle; however, in a few figures the data are plotted versus angle of sideslip. Since the results for $|C_Y|/C_N$ and CP_R are spurious at low angles of attack, and undefined at $\alpha = 0$, these results have been deleted for $\alpha < 10°$. Also, the results from the low-α sting support for $\alpha = 35°$, $40°$, and $45°$ were deleted in order to provide a smooth computerized fairing of the data from the low-α and high-α support systems. It was determined that the overlapping data were usually in close agreement, so that the plotted data are a good representation of the results.

Many tests, such as for the many nose configurations, were limited to the high-α sting support and, for the most part, to $R = 0.8 \times 10^6$, where the principal effect of the many configurations on the side forces could be determined. For these tests, only C_Y, C_N, C_n, C_m and, sometimes, C_{AF} are shown.

DISCUSSION

The primary purpose of this investigation was to determine the forebody configurations and test conditions for which a side force develops at zero sideslip. The results are discussed in the following sections, starting with the results of the investigation at low speed ($M = 0.25$).

Forebody Aerodynamic Characteristics

Comparison of forebody-alone to forebody-in-presence-of-afterbody results— There was some concern that the data obtained with the forebody alone might not represent adequately the contribution of the forebody to the asymmetric side force and moment on a forebody-afterbody configuration because of possible interference between the flow around the base and the flow over the upper surface. To investigate this effect, tests were made with the forebody mounted on the balance and the afterbody attached to the sting but separated slightly from the forebody (forebody forces in the presence of the afterbody). In figure 3 the results for the forebody alone and for the

5

forebody in the presence of the afterbody (indicated by AD, for afterbody detached) are compared for $M = 0.25$ and several Reynolds numbers. The data shown are for $\alpha = 36°$ to $88°$, obtained from the high-α sting support, which includes most of the angle of attack range for asymmetric forces and moments.

The side forces from the two configurations are in close agreement at angles of attack up to $65°$; above this angle, however, there are small differences that can be attributed to base-flow effects. For example, at angles between $65°$ and $80°$, where the side forces decrease to zero, there are differences in side forces between the two configurations; the balance outputs (not shown) were more unsteady for the forebody alone. The normal forces are as much as 13 percent lower for the forebody-alone data at $\alpha \approx 55°$ where peak C_N occurs; the difference is attributed to the end effect of the base. However, at $\alpha = 88°$ the normal forces are almost identical. The base pressure coefficients ($C_{p,b}$) show small differences below $\alpha \approx 60°$ that do not much affect the forebody axial force coefficient (C_{AF}). However, at angles above $\alpha \approx 60°$ both $C_{p,b}$ andd C_{AF} are greatly affected by the base flow, which was expected.

Since the side forces were not greatly affected by the base flow, many tests were made with the forebody alone because it was more convenient. Consequently, in the following sections the forebody-alone and forebody-in-presence-of-afterbody results are used interchangeably to describe the force and moment characteristics of the $\ell/d = 3.5$ forebody. The distinction between the two configurations is indicated in the configuration description at the top of each plot. (AD indicates the presence of the afterbody, detached from the forebody).

Hysteresis— Aerodynamic forces that are related to boundary-layer separation may exhibit a hysteresis effect; that is, the variation of the forces with increasing flow angle might be different than with decreasing angle. The possible effect of hysteresis was investigated by making many of the test runs with both increasing and decreasing flow angle. The results in figure 4 for several Reynolds numbers at $M = 0.25$ show that the side force is generally repeatable with increasing and decreasing angle of attack, indicating little or no hysteresis effect.

Repeatability— Repeated test runs were made with the basic pointed configuration and, as figure 5 shows for $M = 0.25$, the side force was generally repeatable from test to test.

Reynolds number— The effect of Reynolds number was not measured in previous investigations; however, previous use of boundary-layer transition trips have tended to reduce the side force (ref. 5). Consequently, it was felt that increasing Reynolds number might have a similar effect. To investigate this effect, the forebody was tested at $M = 0.25$ over a wide range of Reynolds numbers from 0.3×10^6 to 3.8×10^6 (based on base diameter); the results are presented in figures 6 and 7.

At the lowest Reynolds numbers, a large side force develops, starting at $\alpha \approx 33°$ and extending to $\alpha \approx 80°$. The angle of attack at which the side force first becomes significant (generally within about $\pm 2.5°$) is called the "angle of onset" herein. The direction of the side force has been shown by previous studies to be arbitrary, depending on small geometric asymmetries in each model, especially in the machining of the nose tip (refs. 2 and 10). The magnitude of the maximum side force at the lower Reynolds numbers is as large as 1.4 times the maximum normal force (see $|C_Y|/C_N$), so that the inclination angle, Ψ, of the resultant force is as large as $55°$. Increasing the Reynolds number above $R_d = 0.8 \times 10^6$ progressively reduces the magnitude of the side force, an effect similar to that of tests with boundary-layer trips. However, the maximum side force increases

6

again as the Reynolds number increases above $R_d \approx 2 \times 10^6$, and the direction is opposite to that of the low Reynolds number side force. This means that inclination angle, Ψ, of the resultant force changes from left to right with increasing Reynolds number. This effect is not entirely understood, except that the boundary layer on the windward side of the forebody is tending towards more turbulent flow. A question was raised that the change with Reynolds number could be an effect of the flow in the tunnel; however, the 12-foot wind tunnel used is known to have a very low free stream turbulence and the known effect of increasing noise level with increasing Reynolds number should only increase the effective Reynolds number of the test. Also, the effect of possible small changes in free stream flow angle (such as that due to the sting support fairing) should be negligible according to the tests with sideslip (fig. 10). Note that the effect of increasing the Reynolds number on the angle of onset is small.

The normal-force coefficient has a maximum value of 2.9 at the lowest Reynolds number of 0.3×10^6 and decreases appreciably to about 2 at the remainder of the Reynolds numbers tested (0.8×10^6 to 3.8×10^6). Also, the maximum C_N occurs at angles of attack between 50° to 65°, above which it decreases appreciably, sometimes abruptly, so that the value of C_N at $\alpha = 88°$ is considerably lower than the maximum. Note also that there is an apparent increase in the normal-force curve slope in the angle-of-attack range where the side force increases ($\alpha > 33°$). This increase in C_N curve slope implies that the normal force and, hence, the resultant force, are increased by the flow asymmetry that causes the side force.

The center of pressure, CP_R, of the resultant normal force is located at about $x/\ell = 0.5$ for angles of attack less than 30°. This is in general agreement with the slender-body theory value of $0.46 \ \ell$ for this forebody. At higher angles of attack, CP_R moves slightly rearward until at $\alpha = 88°$ it is close to the centroid of planform area, $x/\ell = 0.624$.

A small rolling moment was recorded that occurred at high angles of attack when the side force was large. Since the asymmetric pressures that produce the side force do not produce a rolling moment for a circular body, the small recorded rolling moment was probably due to an asymmetry in the boundary-layer skin-friction forces. Evidently, a rolling moment due to asymmetric skin-friction forces should be anticipated on flight vehicles when large side forces exist. The data are not presented because the measured rolling moment was small (maximum $|C_l| < 0.02$) and relatively inaccurate from the particular strain-gauge balance used.

In order to investigate the accuracy of the force measurements at the lowest Reynolds numbers, tests were repeated with balance B, which had one-half the normal-force range of balance A used in the other tests. The results for $R_d = 0.3 \times 10^6$, 0.8×10^6, and 1.1×10^6 are presented in figure 7 and show that no significant differences occurred between the results from the two balances.

Roll— Previous investigations (refs. 5 and 10) have shown that when a body is tested in various positions of roll angle about the axis of symmetry that the side force can change direction for a range of roll angles. For example, reference 10 shows that the direction changed every 90° in roll angle for a forebody identical to that of the present model. A considerable amount of experimental data show that the direction of the side force is influenced by very small geometric asymmetries that exist in most models, especially near the nose. In the present results the effect of roll angle (fig. 8) is to change the direction of the side force from left to right in the range of roll angles near $\phi_B = 270°$.

More startling results (fig. 9) were obtained when the removable nose tip (length of 0.192) was rolled to several fixed positions, resulting in an effect that was similar to that of rolling the complete body. Apparently, the asymmetry in the vortex flow is very sensitive to the body geometry near the nose. Note that the angle of onset does not change more than about 5° with roll position.

These roll tests indicate that body models should be tested in several positions of roll, if possible, when determining the asymmetric characteristics at high angles of attack. In addition, the orientation of model parts and of surface discontinuities, such as junctions and set screws, should be noted. Some insight into the possible effect of the junction of the removable nose section may be obtained from the results of tests that were made with a ring of roughness elements located at the junction (fig. 14). Because the side force was greatly reduced, it was believed that the effect of a large discontinuity at the junction would act as a boundary layer trip and would likewise reduce the side force. Since the side force is large without the ring of trips it is believed that the junction effect is negligible.

Sideslip— Figure 10 shows the effect of sideslip angle for $\alpha = 40°$, $55°$, and $70°$ at $R_d = 0.8 \times 10^6$. At sideslip angles between 5° and 15° the side force changes sign (direction). The angle of sideslip range where the change occurs is generally repeatable. The data show nearly identical results for both increasing and decreasing angles of sideslip. The data also show that the direction of sideslip is not sensitive to small variations in stream angles such as those produced by the model support system fairing on the floor of the wind tunnel.

Note that the effect of sideslip on a body is identical to testing at zero sideslip at a slightly higher angle of attack and at a roll angle of both the body and the balance. The change in direction of side force from left to right between $\beta = 5°$ to $15°$ would correspond to roll angles between about 6° and 18°. On the other hand, the side force data at roll angles of 0° and 90° (figs. 8 and 9) are in the same direction, indicating that the side force changed direction twice in the roll range between 0° and 90°, the 0°-90° range was not tested. An identical model used in reference 10 experienced a change in direction of side force every 90°, or four times in 360°. These results indicate that testing in 90° increments could be insufficient to adequately describe the effect of roll.

Boundary-layer trips— Boundary-layer transition trips have been shown in previous investigations (refs. 2 and 5) to reduce the asymmetric force, the amount depending on the location of the trips. At high angles of attack, longitudinal boundary-layer transition strips were partially effective. Surprisingly, a ring of roughness elements around the body behind the nose was also effective, as was the application of roughness elements over a large part of the nose surface area (ref. 2).

Results of the present investigation with boundary-layer transition strips and surface roughness are presented in figures 11-15 for $M = 0.25$. Longitudinal strips at $\Theta = \pm 15°$ (T2 in fig. 11) and $\Theta = \pm 30°$ (T4 in fig. 12) reduce the magnitude of the side force significantly (by 50 percent or more). When the length of the transition strips at $\Theta = \pm 30°$ is reduced to 1/3 of the body length (T6 in fig. 12), the maximum side force is even smaller than with the full-length strip, an indication that the vortex asymmetry is sensitive to the nature of the boundary layer near the apex. Results of tests with transition strips at $\Theta = 0°$ and $\Theta = \pm 60°$ (data not shown) showed little or no reduction in side force.

The side force is also reduced by a ring of roughness elements around the forebody (fig. 13) when the elements are located at $x/\ell = 0.09$, 0.14, 0.19, and 0.286. However, a ring at $x/\ell = 0.05$ and at 0.286 is less effective in reducing the side force. Figure 14 shows that the ring of roughness elements at $x/\ell = 0.19$ is not as effective at higher Reynolds numbers. (Perhaps, the results for the longitudinal strips might also be affected by Reynolds number, but this was not tested.)

An interesting effect related to boundary-layer tripping was found when the forebody was sprayed with flat-black, spray-can paint in preparation for oil-flow studies. The surface of the coat of paint on the model was very rough and tests without oil showed a substantial reduction in the side force (fig. 15). Polishing the flat paint did not change the results. Only when a gloss enamel paint was applied and highly polished did the maximum side force increase to nearly the value obtained with the smooth, bare model (fig. 15). This result is not surprising, however, since the effect of rough paint on the boundary layer must be similar to that produced by using roughness elements. Adding oil to the polished surface reduced the side force only slightly; however, it must not be assumed that oil will not induce large changes. In oil flow tests, the forces should be measured to determine if changes occur.

These results with boundary-layer trips show that the side force is sensitive to the nature of the boundary layer (i.e., whether it is laminar, transitional, or turbulent), especially near the forebody apex.

Nose bluntness— Based on the results presented in references 5 and 10, it was expected, but not certain, that the side force would be maximum for pointed noses and would decrease with increasing nose bluntness. To investigate this effect, three nose radii were tested (figs. 16-18). Even the smallest nose radius of 4 percent of the base radius (NB1) (fig. 16) greatly reduces the side force. The next larger radius of 8 percent (NB2) has the lowest side force at $R_d = 0.8 \times 10^6$, although at the higher Reynolds numbers (fig. 17) the side force is larger. Increasing the nose radius further to 16.7 percent increases the maximum side force. The variation of the side force with sideslip (fig. 18) is almost linear; no abrupt changes occur as for the pointed-nose results (fig. 10). The flow mechanism associated with nose bluntness is not understood at his time, but it must be related to the effect of the shape of the nose section on the local flow, perhaps in spreading the initial vortices farther apart. Evidently, some caution should be exercised in the use of nose bluntness to reduce side forces, because it is possible that there is an optimum nose radius for a particular configuration.

Strakes— Previous studies have shown that strakes placed on each side of the body near the nose can reduce the asymmetric force (ref. 10). To investigate the effect of strakes, a slot was made in a duplicate, pointed nose section. Three removable, flat, sharp-edged plates were made to insert in the slot; the plates had exposed widths on each side of 0.32, 0.64, and 1.27 cm. Even the narrowest strake (NST1 in figs. 19 and 20) essentially eliminated the side force at all except the lowest Reynolds number of 0.3×10^6, where the side force is greatly reduced. As expected, a side force occurs with sideslip angle (fig. 21), which is identical to rolling the forebody. Note that the side force and yawing moment variations with sideslip angle are directionally stable at $\alpha = 40°$.

Figure 22 shows that when the roll angle of the removable nose with the narrowest strake is varied, the effect produces mixed variations in the side force. Note that at angles of attack of up to about 50° the side force and yawing moment increases with roll angles up to 30°. In this angle of attack range a rotatable nose with strakes might, perhaps, be used to provide high angle-of-attack yawing moment control.

9

Nose booms– Many aircraft use nose booms that extend ahead of the fuselage to mount pitot-static pressure systems and systems that measure the flow angle. Consequently, tests were conducted with short rods (0.319-cm in diameter) of two different lengths (2.54 and 5.08 cm) inserted in the blunt noses and one of one length (2.54 cm) inserted in the sharp nose of the $\ell/d = 3.5$ tangent ogive forebody. No significant effect was obtained with nose booms mounted in the blunt noses. On the other hand, a nose boom mounted in the pointed nose greatly reduced the large side force (fig. 23). The side force varies somewhat with Reynolds number and it is noted that the data are not repeated very well at $R_d = 0.8 \times 10^6$. Although the angle of onset appears to vary with Reynolds number the lowest angle of onset is about 35°, similar to the results without the nose boom.

Canopy– The simulated canopy had no effect on the asymmetric forces at $M = 0.25$ at zero sideslip (data not shown).

Mach number– It was expected from the results of reference 5 that the side force would decrease with increasing Mach number. To investigate this effect, tests were made at several Mach numbers from 0.1 to 0.7 at $R_d = 0.8 \times 10^6$. The results in figure 24 show that the magnitude of the side force decreases with increasing Mach number. At $M = 0.7$, the maximum absolute value of C_Y is less than 0.5. Note that the angle of onset does not vary much with Mach number.

Forebody With Afterbody

Effect of Reynolds number– Figure 25 shows the results at several Reynolds numbers for the forebody attached to the $\ell/d = 3.5$ afterbody. The magnitude of the side force is generally as large or larger than for the forebody alone and it changes direction with increasing angle of attack, indicating that additional vortices might be forming and shedding due to the increased length of the afterbody. At $R_d = 0.8 \times 10^6$, the side force is noticeably smaller than at any of the other Reynolds numbers, whether higher and lower. The reason for this is not known, although it is possible that some intermediate transitional flow condition exists at Reynolds numbers near this value. The angle of onset of side force is between 25° and 30°, about 5° to 10° lower than for the forebody alone.

Similar to the forebody results, the normal-force-curve slope increases noticeably when the side force increases, as does the resultant force (compare the curves for C_N, $|C_Y|/C_N$ and $C_R - C_N$). The maximum normal force occurs near an angle of attack of 55° and is noticeably greater than the magnitudes at $\alpha = 88°$. The resultant center of pressure ranges between 70 and 120 percent of the forebody length as angle of attack increases from 10° to 88°.

Effect of Mach number– Figure 26 shows the effect of Mach number from 0.1 to 0.7 at $R_d = 0.8 \times 10^6$. Note that at $M = 0.25$ the side force is smallest for this Reynolds number (fig. 25); this is an unexplained anomaly, because at other Reynolds numbers tested the magnitude of the absolute value of the maximum measured side force coefficient, $|C_Y|$, is about 3.4 at $M = 0.25$. At $M = 0.7$ maximum $|C_Y|$, is reduced to about 2. The angle of onset is essentially constant with Mach number. A large increase in normal force occurs, as expected, with increasing Mach number. Note the discontinuities in the C_N curves at $M = 0.6$ and 0.7 at $\alpha \approx 40°$ and 45°, coinciding with the rapid decrease in the side force.

10

CONCLUSIONS

Based on data obtained from this wind-tunnel investigation to determine the effect of fore-body shape on the asymmetric force and moment generated on an $\ell/d = 3.5$, tangent ogive at high angles of attack and at zero sideslip, the following conclusions are made. Data were obtained over a wide range of angles of attack, angles of sideslip, Reynolds numbers and Mach numbers up to 0.7.

1. At low speeds the pointed forebody develops a side force at angles of attack above about $33°$. The side force increases to a maximum at an angle of attack of about $55°$ and decreases to zero at an angle of about $80°$.

2. The variation of side force is generally repeatable with increasing and decreasing angle of attack and also from test to test.

3. The maximum side force is as large as 1.5 times the maximum normal force.

4. The side force is sensitive to the nature of the boundary layer as indicated by large changes with boundary layer trips.

5. The normal-force curve slope is increased in the angle-of-attack range where the side force occurs and the maximum normal force occurs at angles of attack near $60°$, rather than at $90°$.

6. The maximum side force varies considerably with Reynolds number and decreases with increasing Mach number to near zero at $M = 0.7$.

7. The direction and magnitude of the side force is sensitive to the body geometry near the nose: rotating the nose tip changes the direction of the side force; nose boom and boundary-layer trips near the apex significantly reduce the side force; and nose strakes and small bluntness tend to eliminate the side force.

8. The angle of attack of onset of side force is not strongly influenced by Reynolds number or Mach number.

9. The short $\ell/d = 3.5$ afterbody lowers the angle of onset of side force by about $5°$.

Ames Research Center
    National Aeronautics and Space Administration
        Moffett Field, California 94035, July 9, 1976.

REFERENCES

1. Allen, H. J.; and Perkins, E. W.: A Study of the Effects of Viscosity on Flow Over Slender Inclined Bodies of Revolution. NACA TR 1048, 1951.

2. Letko, W.: A Low-Speed Experimental Study of the Directional Characteristics of a Sharp-Nosed Fuselage Through a Large Angle-of-Attack Range at Zero Angle of Sideslip. NACA TN 2911, 1953.

3. Chambers, J. R.; Anglin, E. L.; and Bowman, J. S., Jr.: Effects of a Pointed Nose on Spin Characteristics of a Fighter Airplane Model Including Correlation with Theoretical Calculations. NASA TN D-5921, 1970.

4. Thomson, K. D.; and Morrison, D. F.: The Spacing, Position, and Strength of Vortices in the Wake of Slender Cylindrical Bodies at Large Incidences. J. of Fluid Mech., vol. 50, part 4. 1971, pp. 751-783.

5. Pick, G. S.: Investigation of Side Forces on Ogive-Cylinder Bodies at High Angles of Attack in the $M = 0.5$ to 1.1 Range. AIAA Paper 71-570, 1971.

6. Clark, W. H.; and Peoples, J. R.: Occurrence and Inhibition of Large Yawing Moments During High Incidence Flight of Slender Missile Configurations. AIAA Paper 72-968, 1972.

7. Jorgensen, Leland H.; and Nelson, Edgar R.: Experimental Aerodynamic Characteristics for a Cylindrical Body of Revolution With Various Noses at Angles of Attack from $0°$ to $58°$ and Mach Numbers from 0.6 to 2.0. NASA TM X-3128, 1974.

8. Jorgensen, Leland H.; and Nelson, Edgar R.: Experimental Aerodynamic Characteristics for a Cylindrical Body of Revolution With Side Strakes and Various Noses at Angles of Attack from $0°$ to $58°$ and Mach Numbers From 0.6 to 2.0. NASA TM X-3130, 1975.

9. Jorgensen, Leland H.; and Nelson, Edgar R.: Experimental Aerodynamic Characteristics for Bodies of Elliptic Cross Section at Angles of Attack From $0°$ to $58°$ and Mach Numbers From 0.6 to 2.0. NASA TM X-3129, 1975.

10. Coe, P. L., Jr.; Chambers, J. R.; and Letko, W.: Asymmetric Lateral-Directional Characteristics of Pointed Bodies of Revolution at High Angles of Attack. NASA TN D-7095, 1973.

11. Keener, Earl R.; and Chapman, Gary T.: Onset of Aerodynamic Side Forces at Zero Sideslip on Symmetric Forebodies at High Angles of Attack. AIAA Paper 74-770, 1974.

12. Keener, Earl R.; and Taleghani, Jamshid: Wind Tunnel Investigation of the Aerodynamic Characteristics of Five Forebody Models at High Angles of Attack at Mach Numbers From 0.25 to 2. NASA TM X-73,076, 1975.

13. Keener, E. R.; Chapman, G. T.; and Kruse, R. L.: Effects of Mach Number and Afterbody Length on Onset of Asymmetric Forces on Bodies at Zero Sideslip and High Angles of Attack. AIAA Paper 76-66, 1976.

REMOVABLE NOSES

NOSE
BOOMS

STRAKES

SHARP
&
BLUNT

CANOPY

TAN. OGIVE
$l/d = 3.5$

AFTERBODY
$l/d = 3.5$
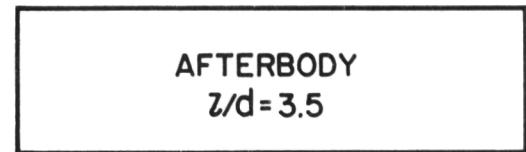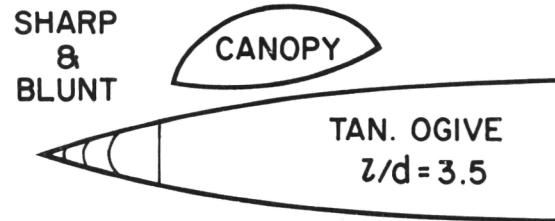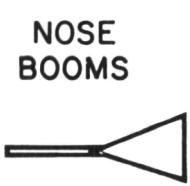
Figure 1.— Sketch of models.
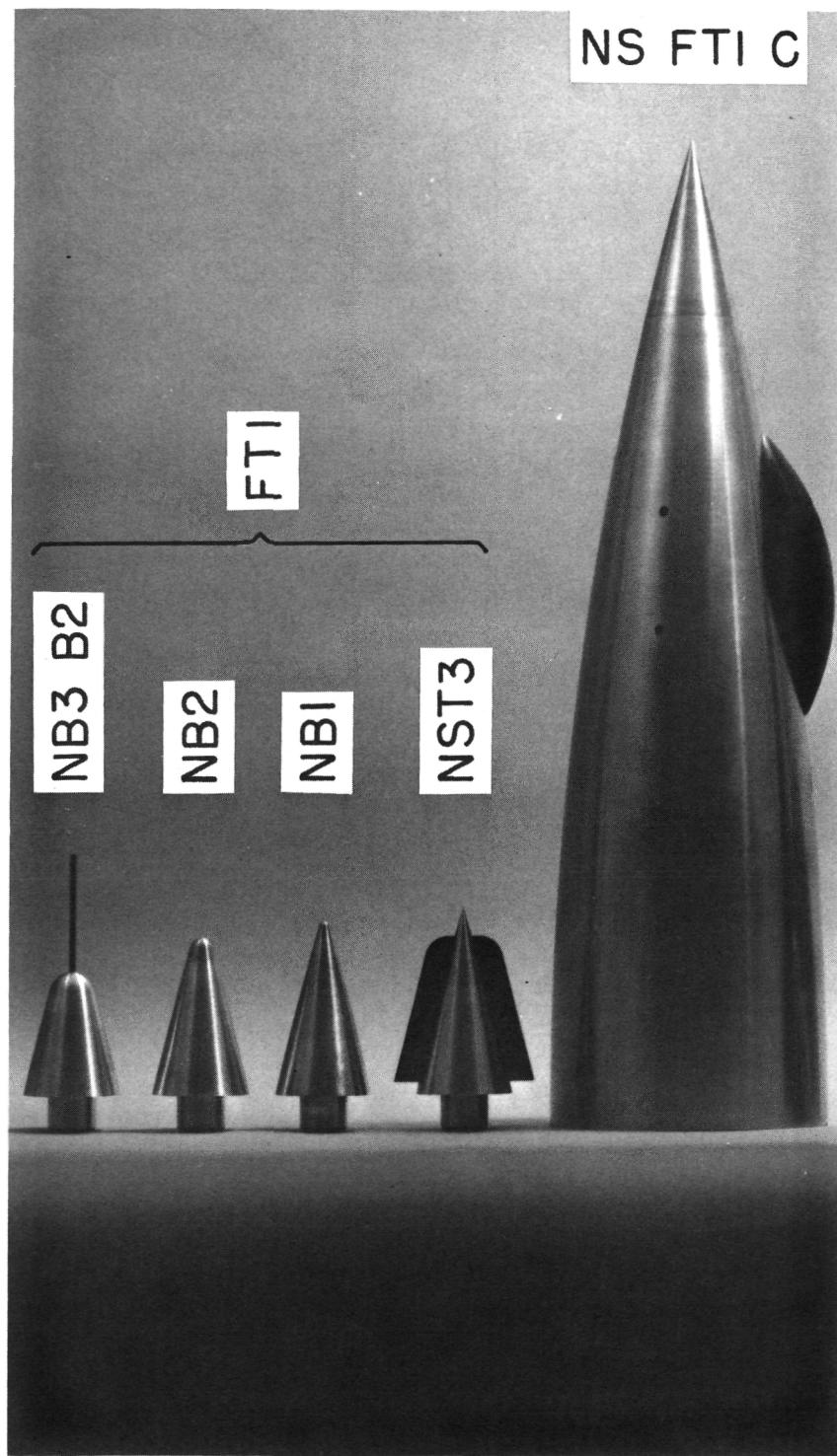
(a) $\ell/d = 3.5$ tangent ogive with removable noses and simulated canopy.

Figure 2.— Photographs of models and tunnel installation.
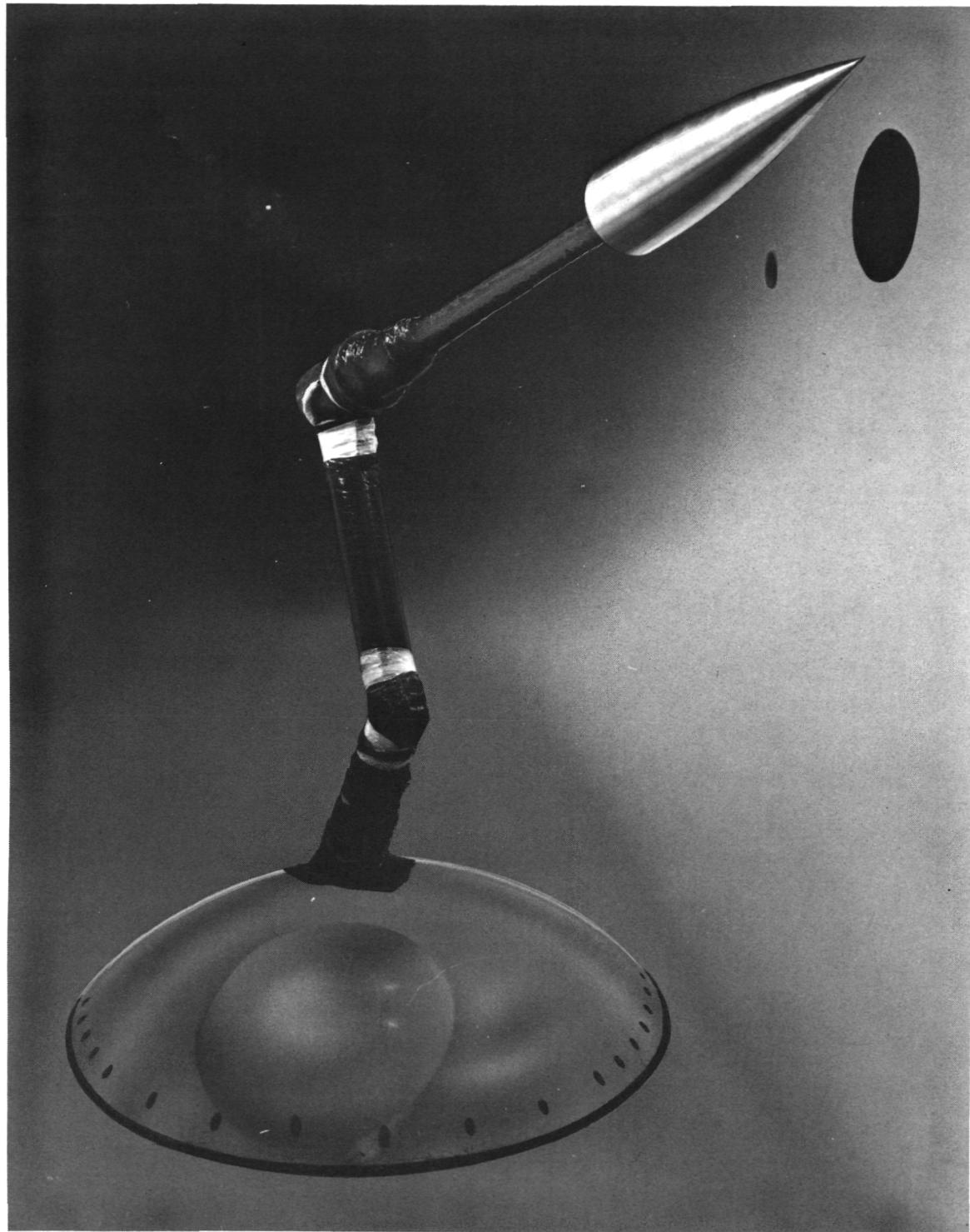
(b) Installation of $\ell/d = 3.5$ tangent ogive on floor-support system, $\alpha = 0°$ to $45°$.

Figure 2.– Continued.

(c) Installation of $\ell/d = 3.5$ tangent ogive on floor-support system, $\alpha = 36°$ to $88°$.

Figure 2.— Continued.
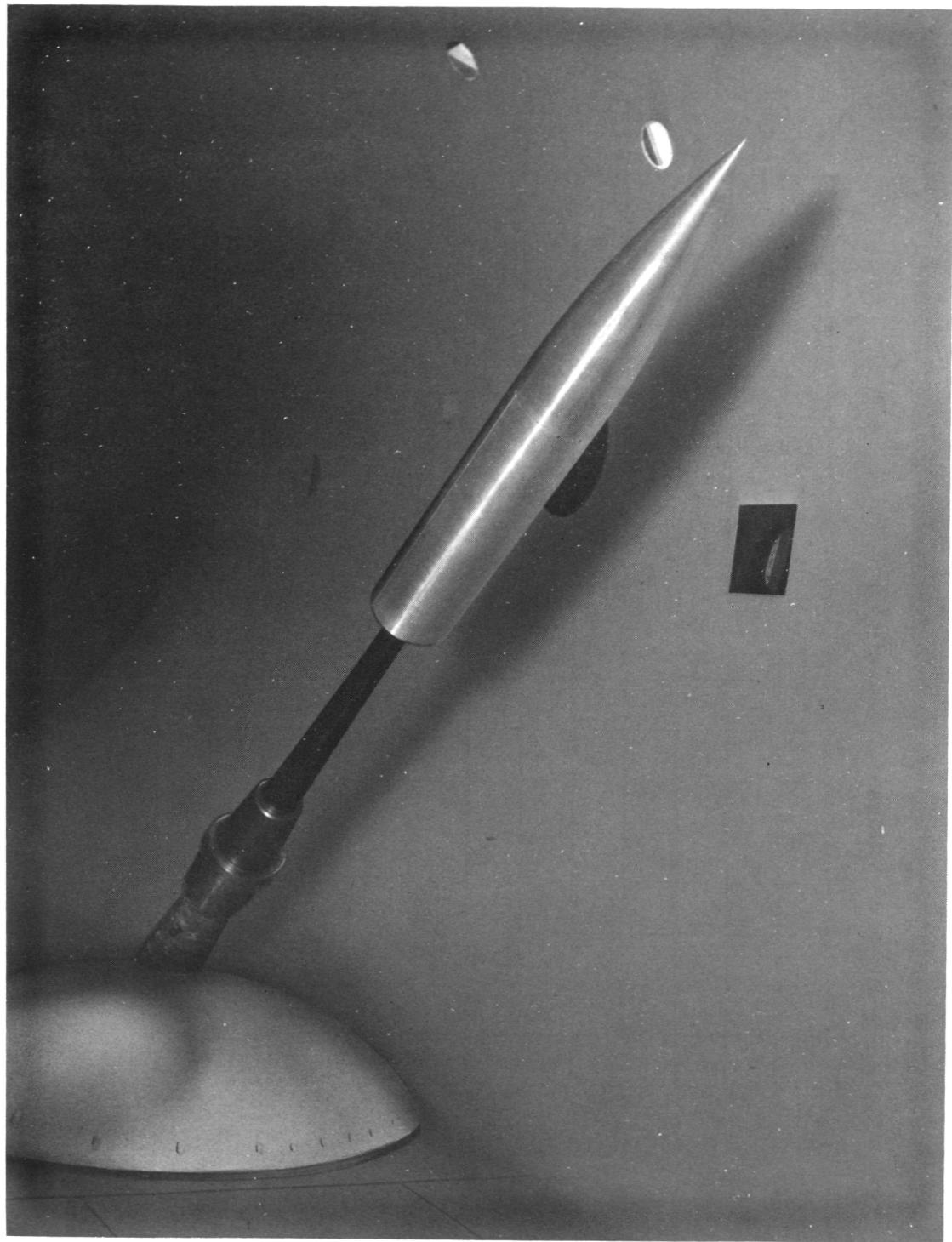
(d) $\ell/d = 3.5$ tangent ogive with $\ell/d = 3.5$ afterbody.

Figure 2.— Concluded.
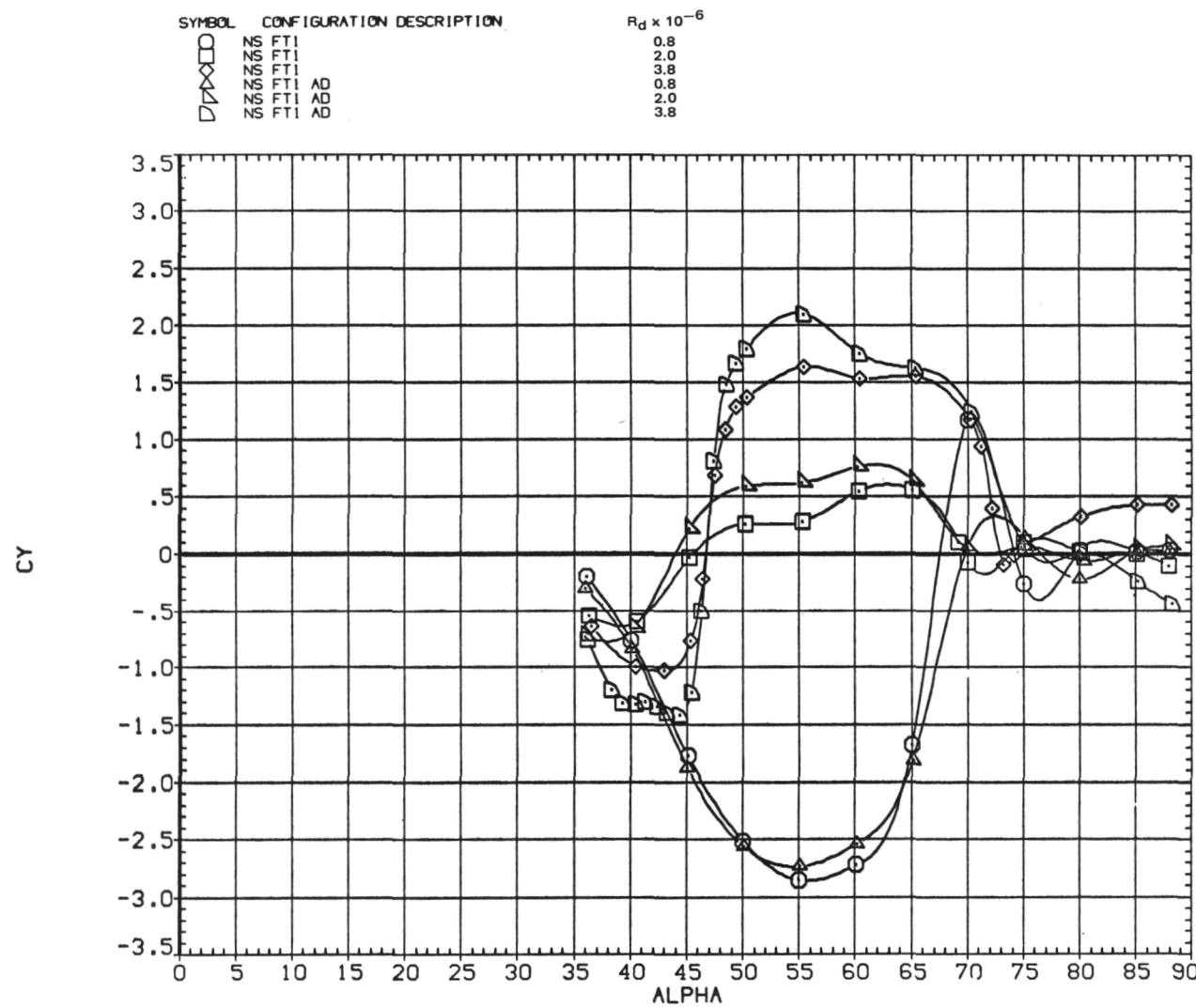
(a) C_Y versus α.

Figure 3.— Comparison of forebody alone to forebody in presence of afterbody; $M = 0.25$.

SYMBOL	CONFIGURATION DESCRIPTION	$R_d \times 10^{-6}$
○	NS FT1	0.8
□	NS FT1	2.0
◇	NS FT1	3.8
△	NS FT1 AD	0.8
▽	NS FT1 AD	2.0
◁	NS FT1 AD	3.8

(b) C_N versus α.

Figure 3.– Continued.

SYMBOL	CONFIGURATION DESCRIPTION	$R_d \times 10^{-6}$
◯	NS FT1	0.8
◻	NS FT1	2.0
◇	NS FT1	3.8
⬡	NS FT1 AD	0.8
△	NS FT1 AD	2.0
▽	NS FT1 AD	3.8

(c) $C_{p,b}$ and C_{AF} versus α.

Figure 3.— Concluded.

SYMBOL   CONFIGURATION DESCRIPTION $R_d \times 10^{-6}$

○   NS FT1 AD   0.8
□   NS FT1 AD   DECR ALPHA   0.8
◇   NS FT1 AD   2.0
△   NS FT1 AD   DECR ALPHA   2.0
◁   NS FT1 AD   3.8
◻   NS FT1 AD   DECR ALPHA   3.8
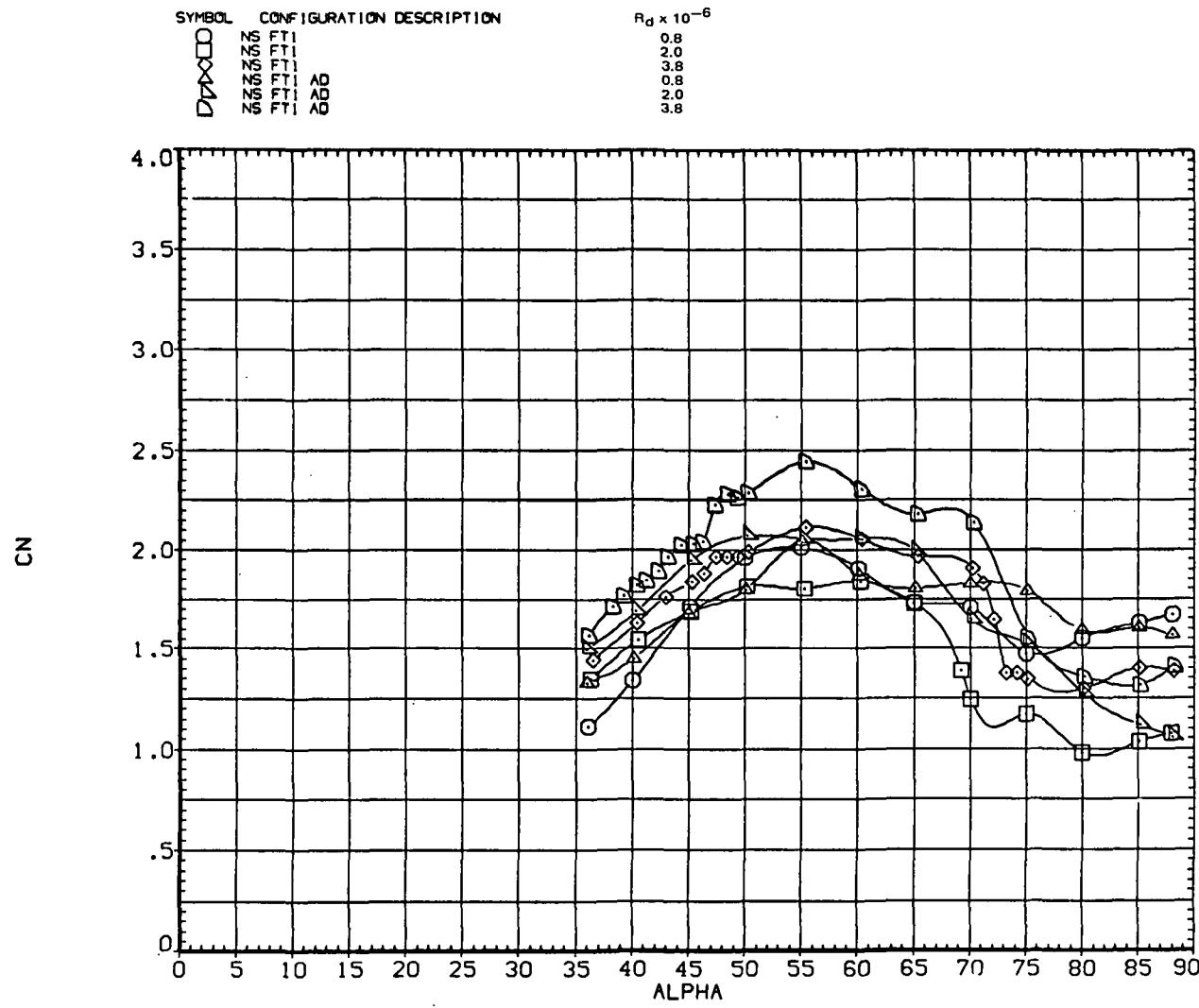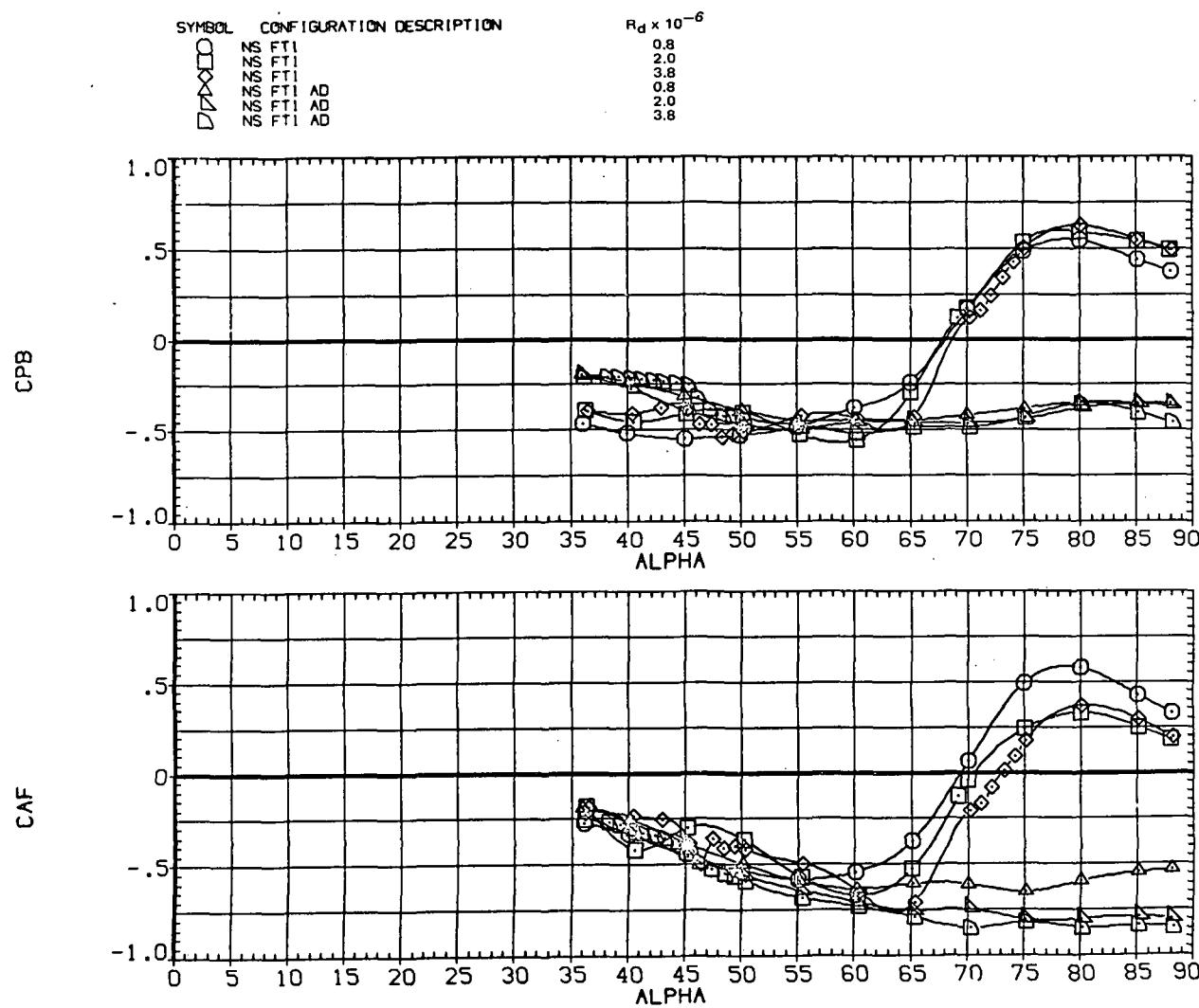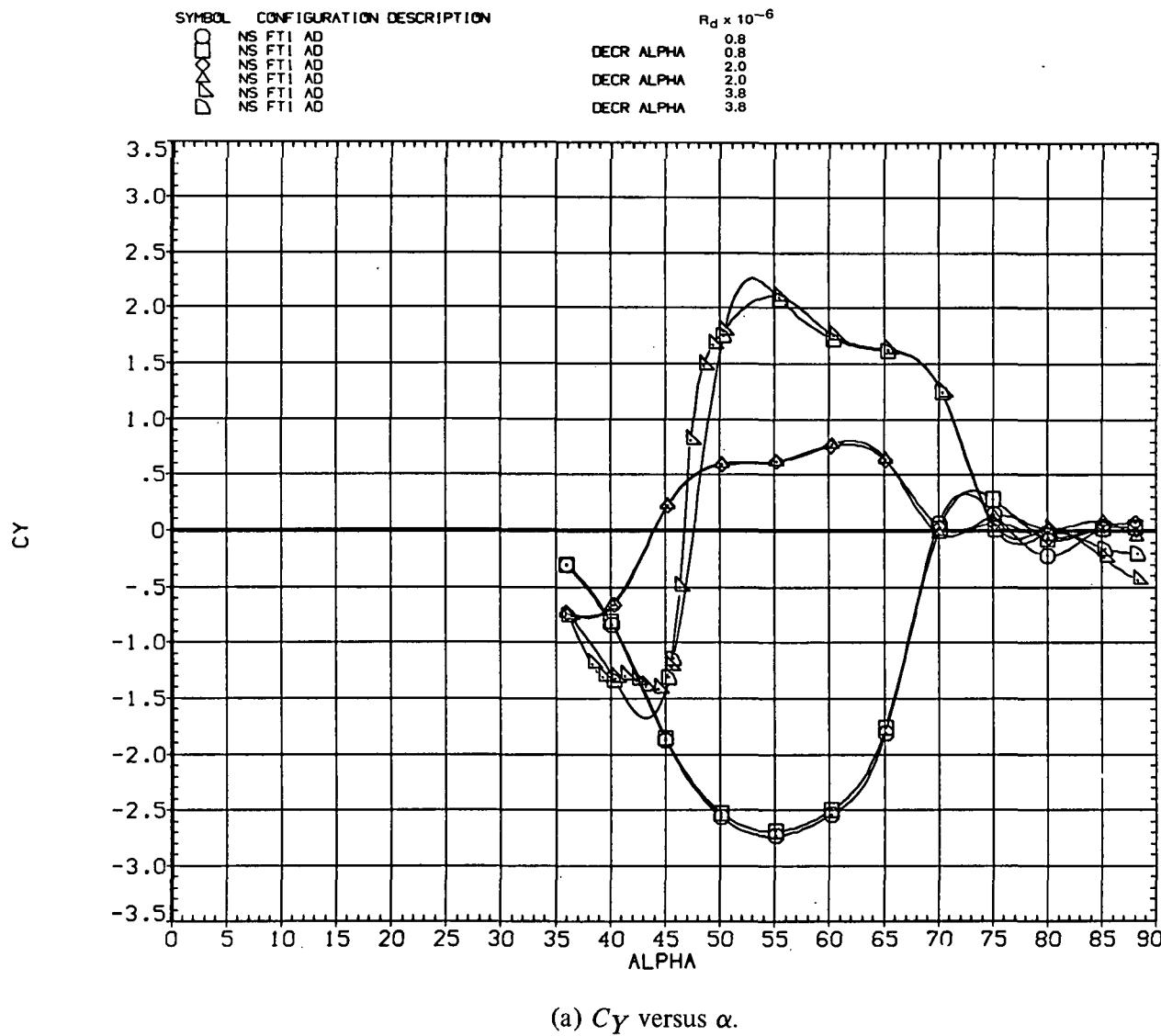
(a) C_Y versus α.

Figure 4.– Effect of hysteresis; $M = 0.25$.

SYMBOL	CONFIGURATION DESCRIPTION		$R_d \times 10^{-6}$
	NS FT1 AD		0.8
	NS FT1 AD	DECR ALPHA	0.8
	NS FT1 AD		2.0
	NS FT1 AD	DECR ALPHA	2.0
	NS FT1 AD		3.8
	NS FT1 AD	DECR ALPHA	3.8

(b) C_N versus α.

Figure 4.– Continued.

SYMBOL   CONFIGURATION DESCRIPTION   R_d x 10^{-6}

⌀   NS FT1 AD   0.8
◻   NS FT1 AD   DECR ALPHA   0.8
⬡⊠   NS FT1 AD   2.0
◇   NS FT1 AD   DECR ALPHA   2.0
▷△   NS FT1 AD   3.8
⬠   NS FT1 AD   DECR ALPHA   3.8

(c) C_n and C_m versus α.

Figure 4.— Concluded.

SYMBOL · CONFIGURATION DESCRIPTION
NS FT1 AD
NS FT1 AD
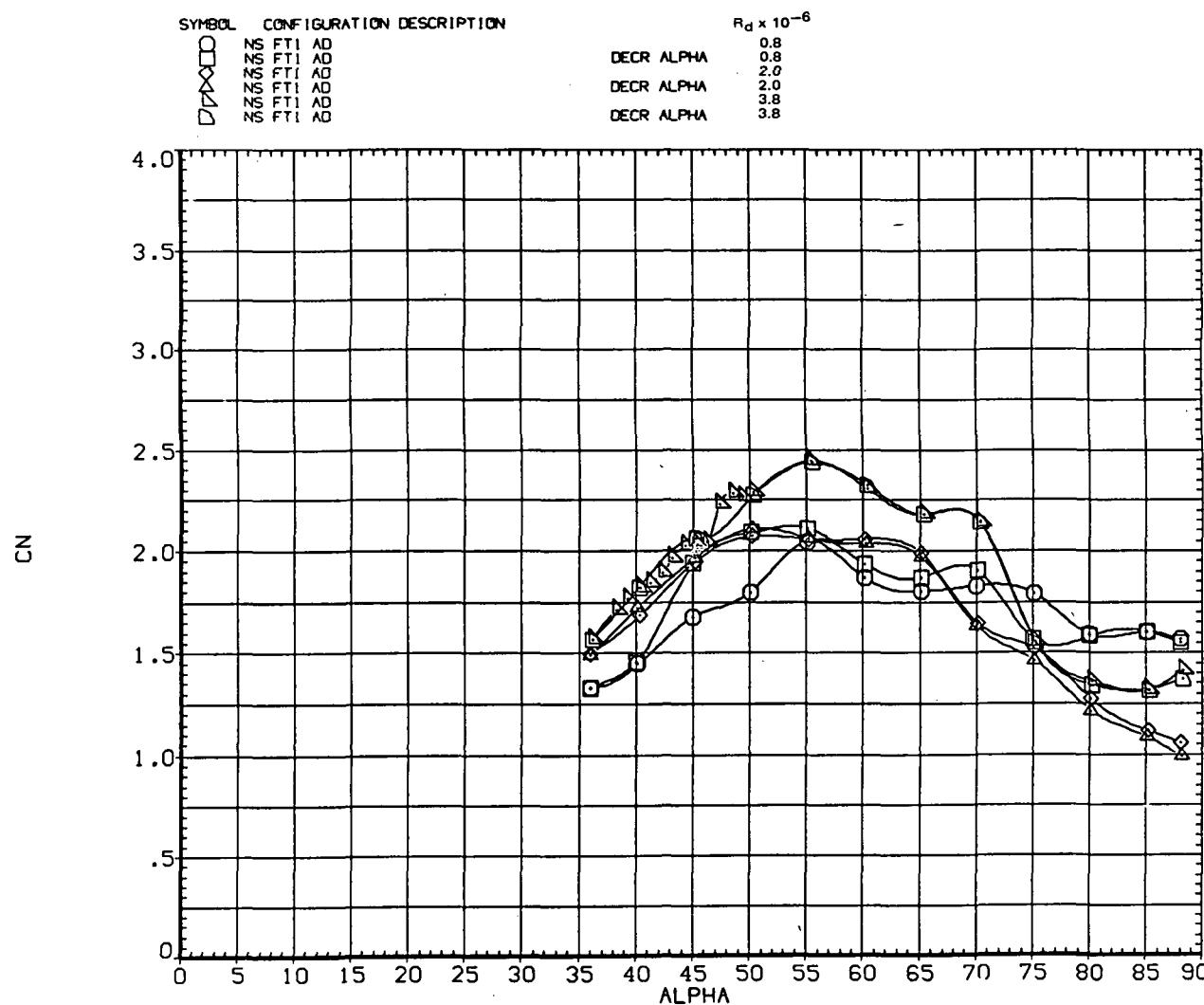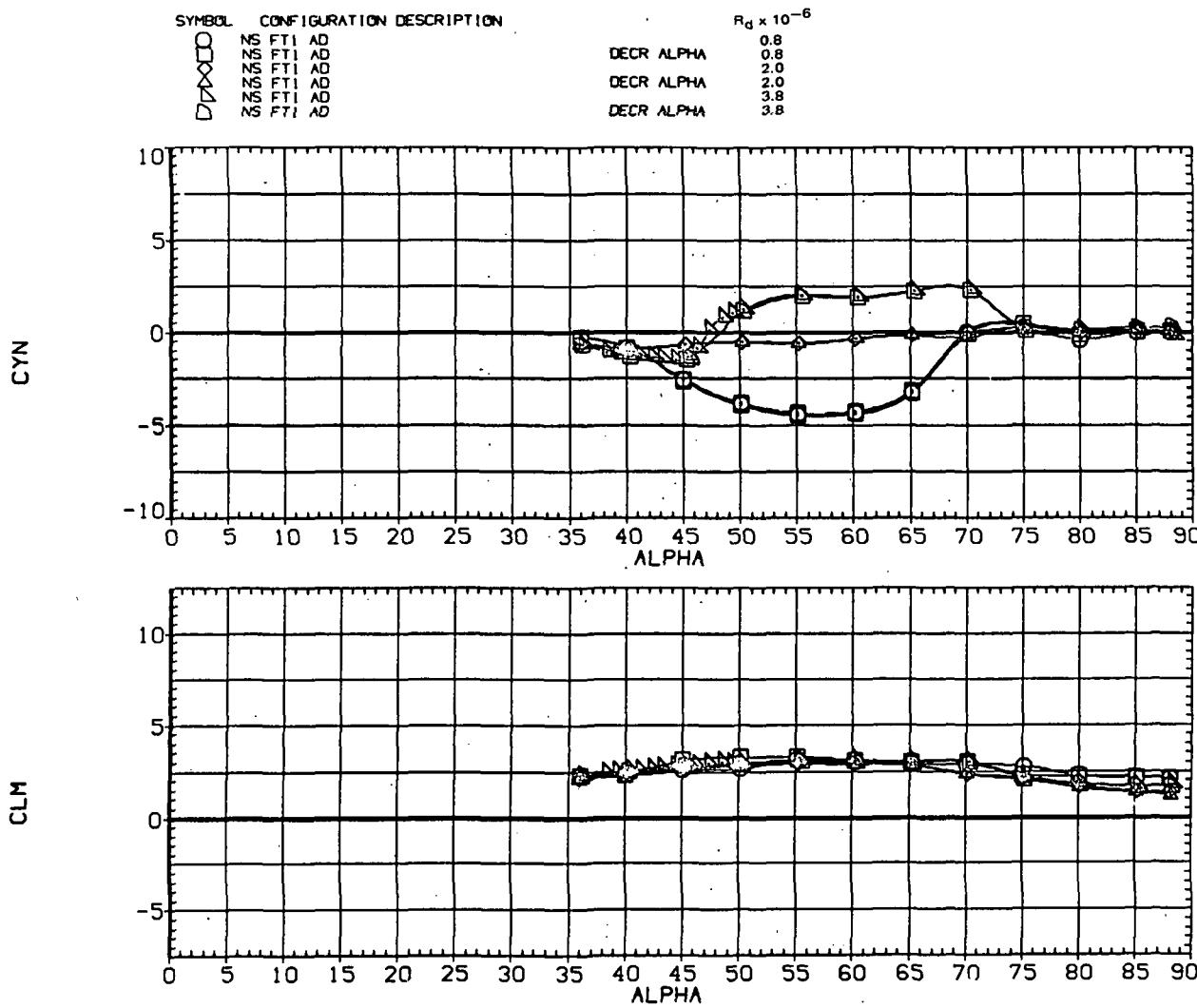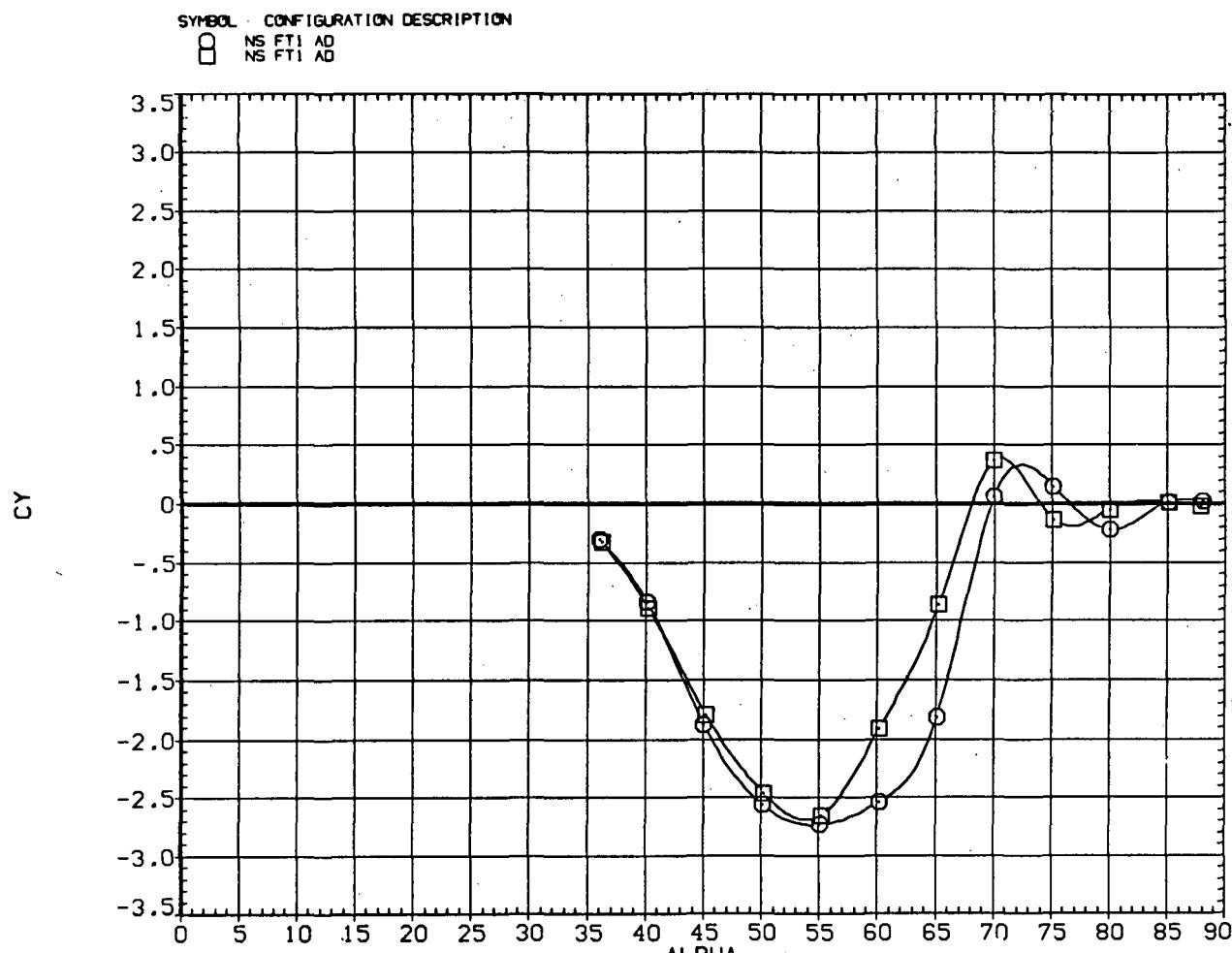
(a) C_Y versus α.

Figure 5.— Repeatability of data; $M = 0.25, R_d = 0.8 \times 10^6$.

(b) C_N versus α.

Figure 5.– Continued.

SYMBOL   CONFIGURATION DESCRIPTION
    NS FT1 AD
    NS FT1 AD
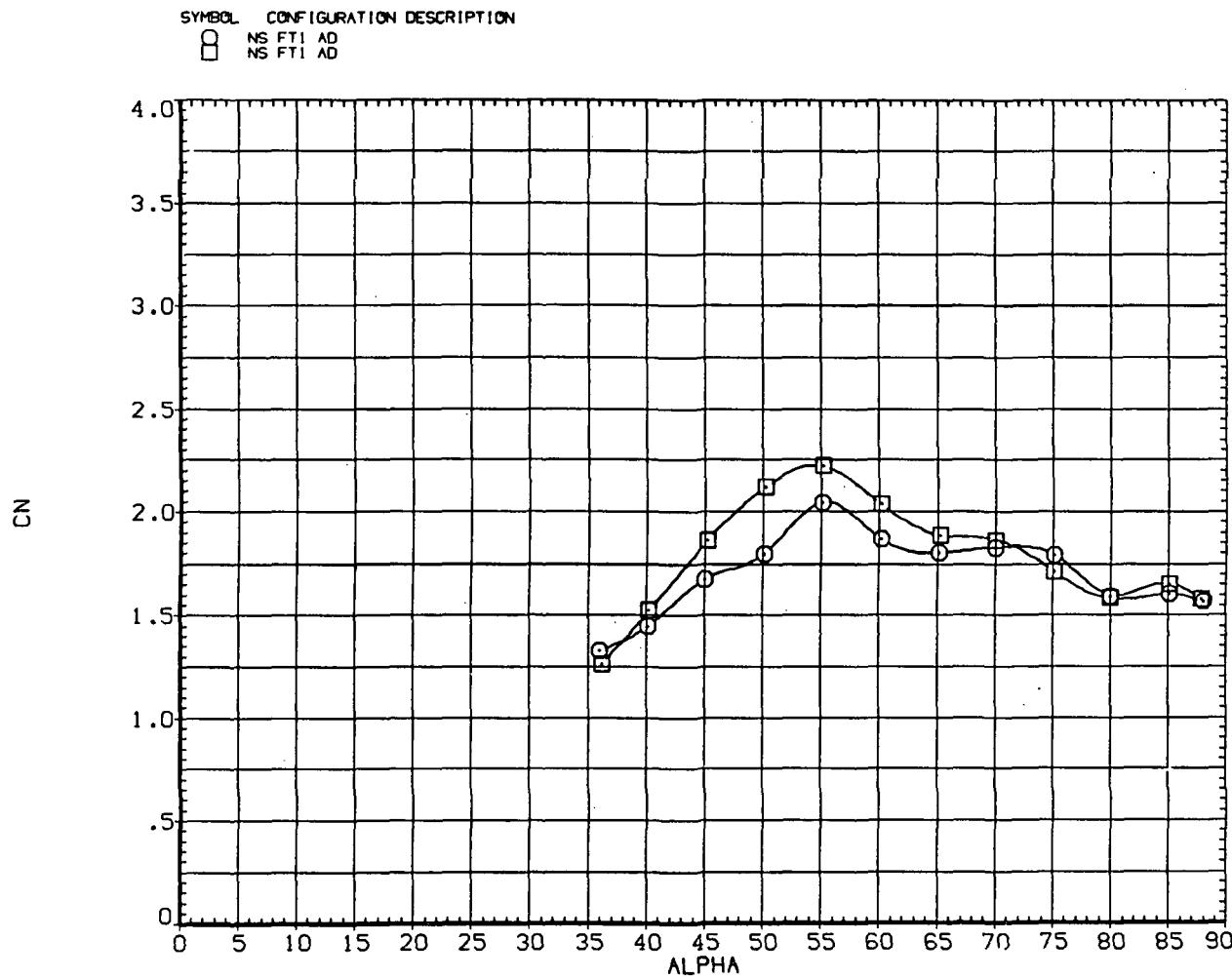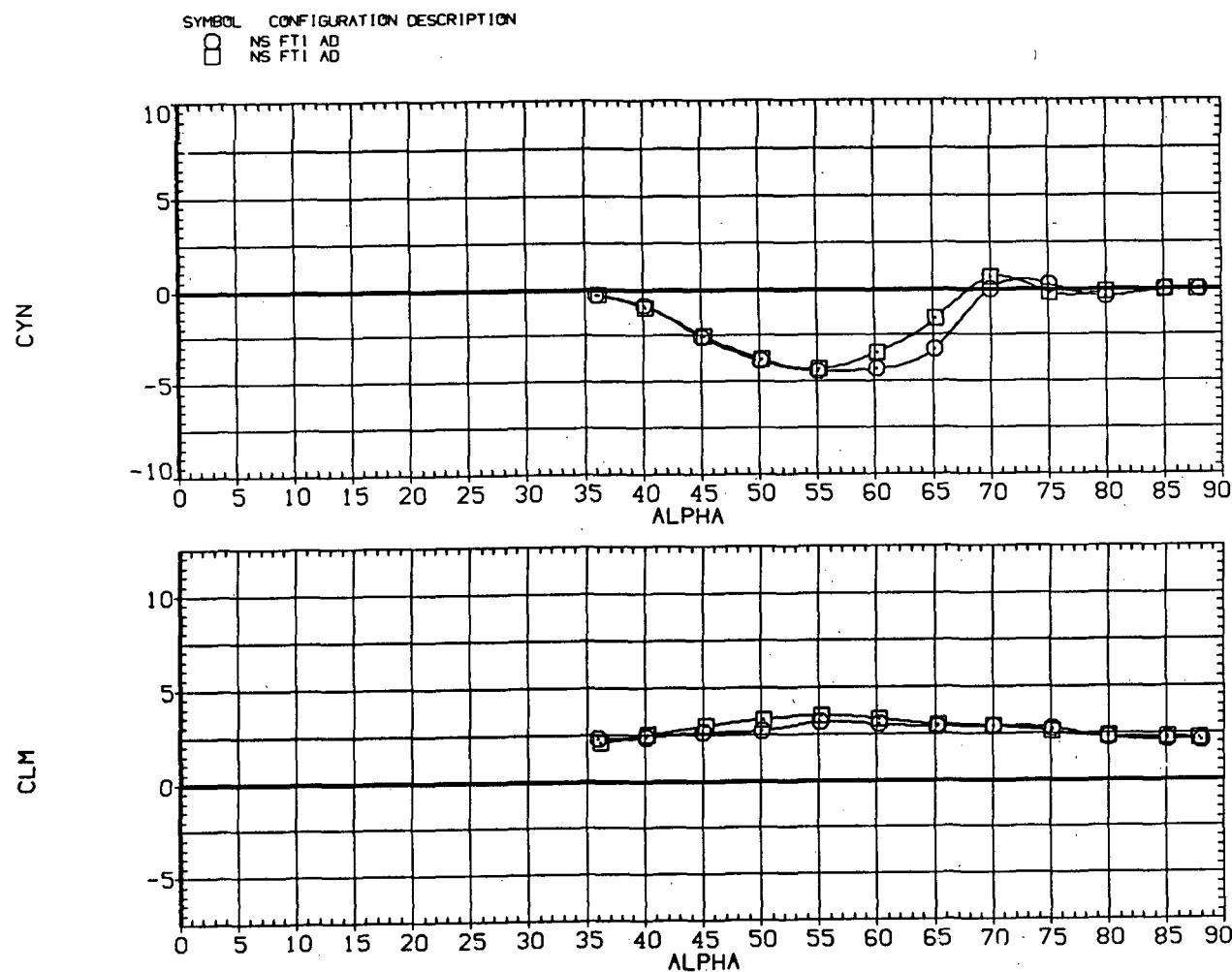
(c) C_n and C_m versus α.

Figure 5.— Concluded.
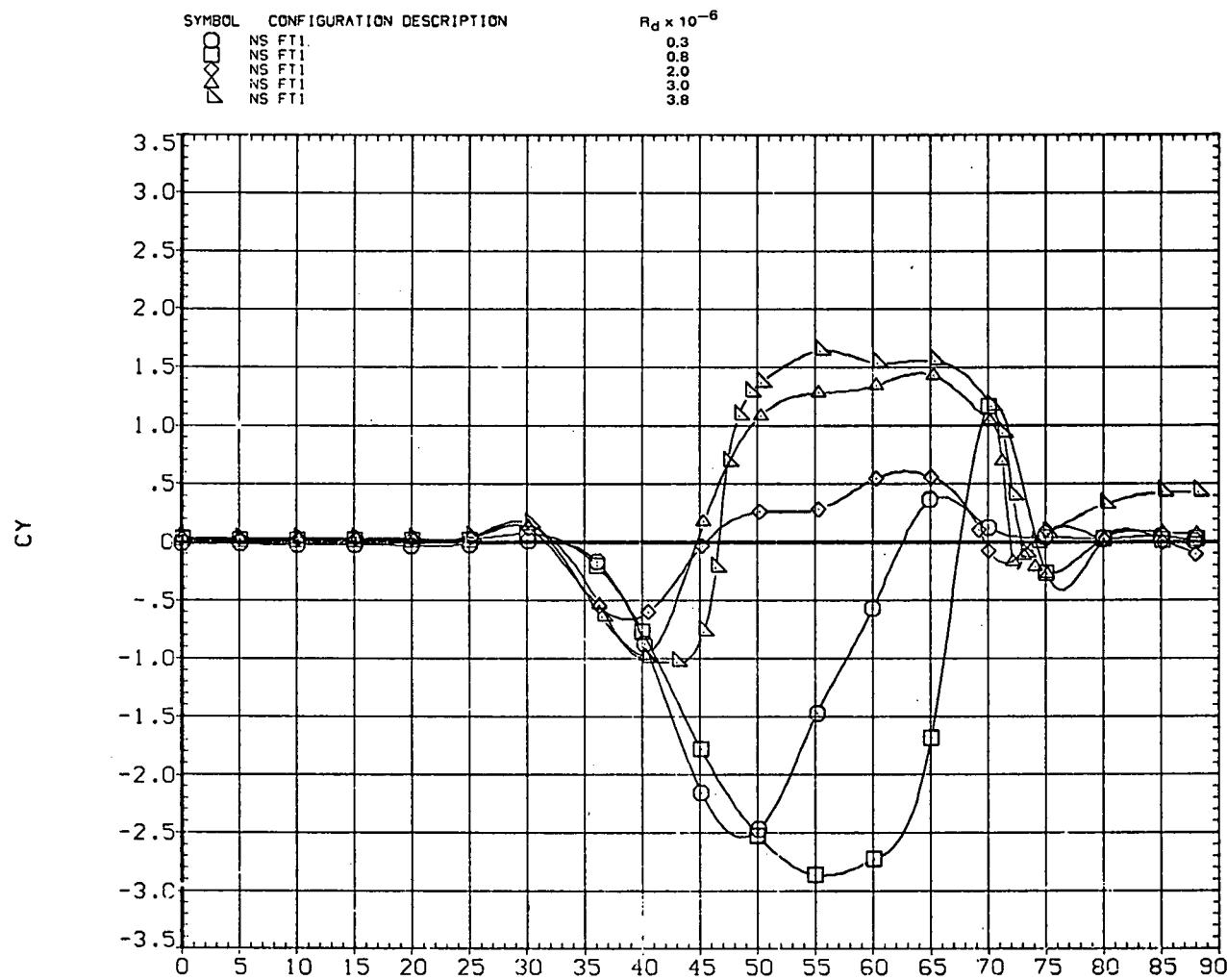
(a) C_Y versus α.

Figure 6.— Effect of Reynolds number; balance A, $M = 0.25$.
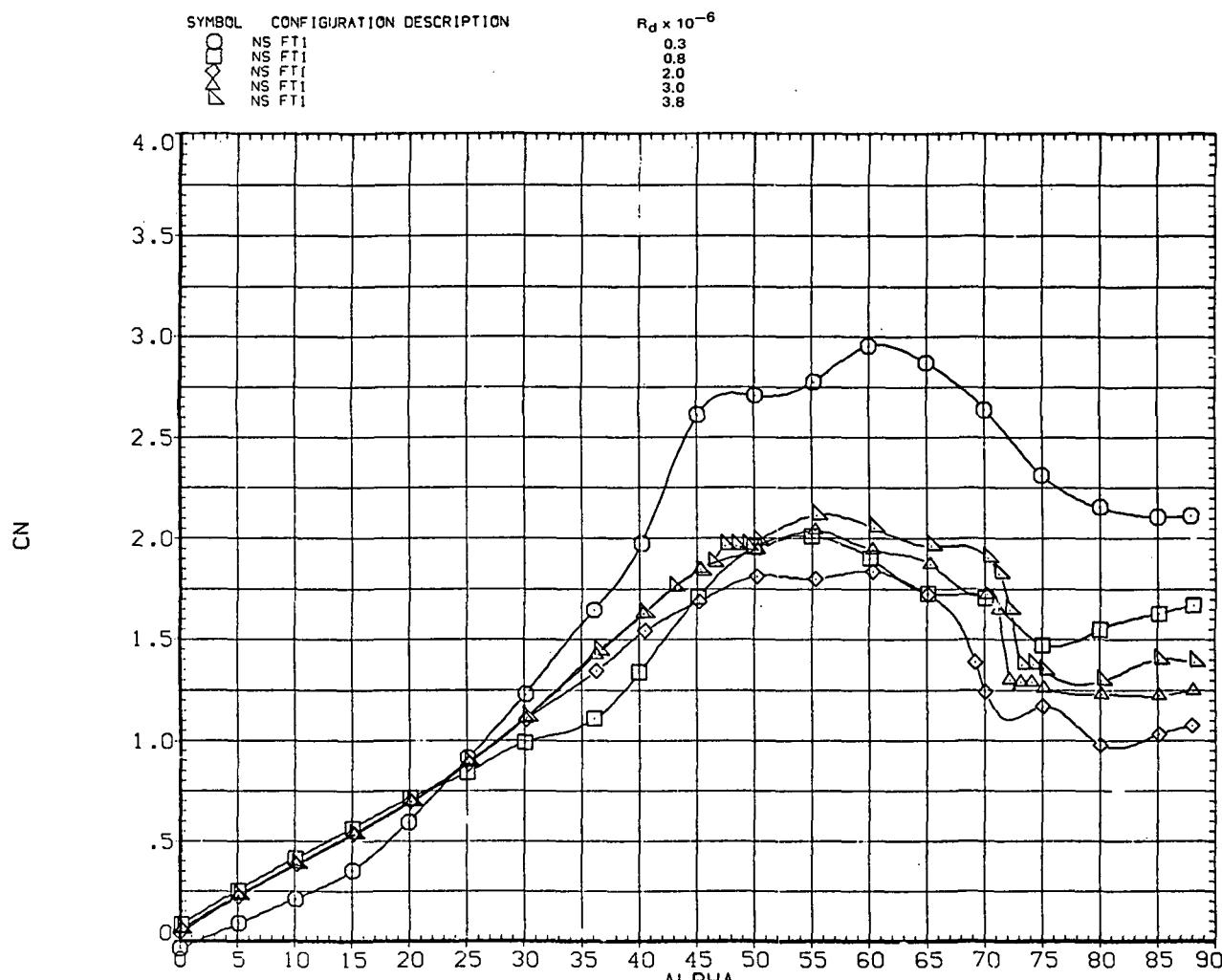
(b) C_N versus α.

Figure 6.– Continued.
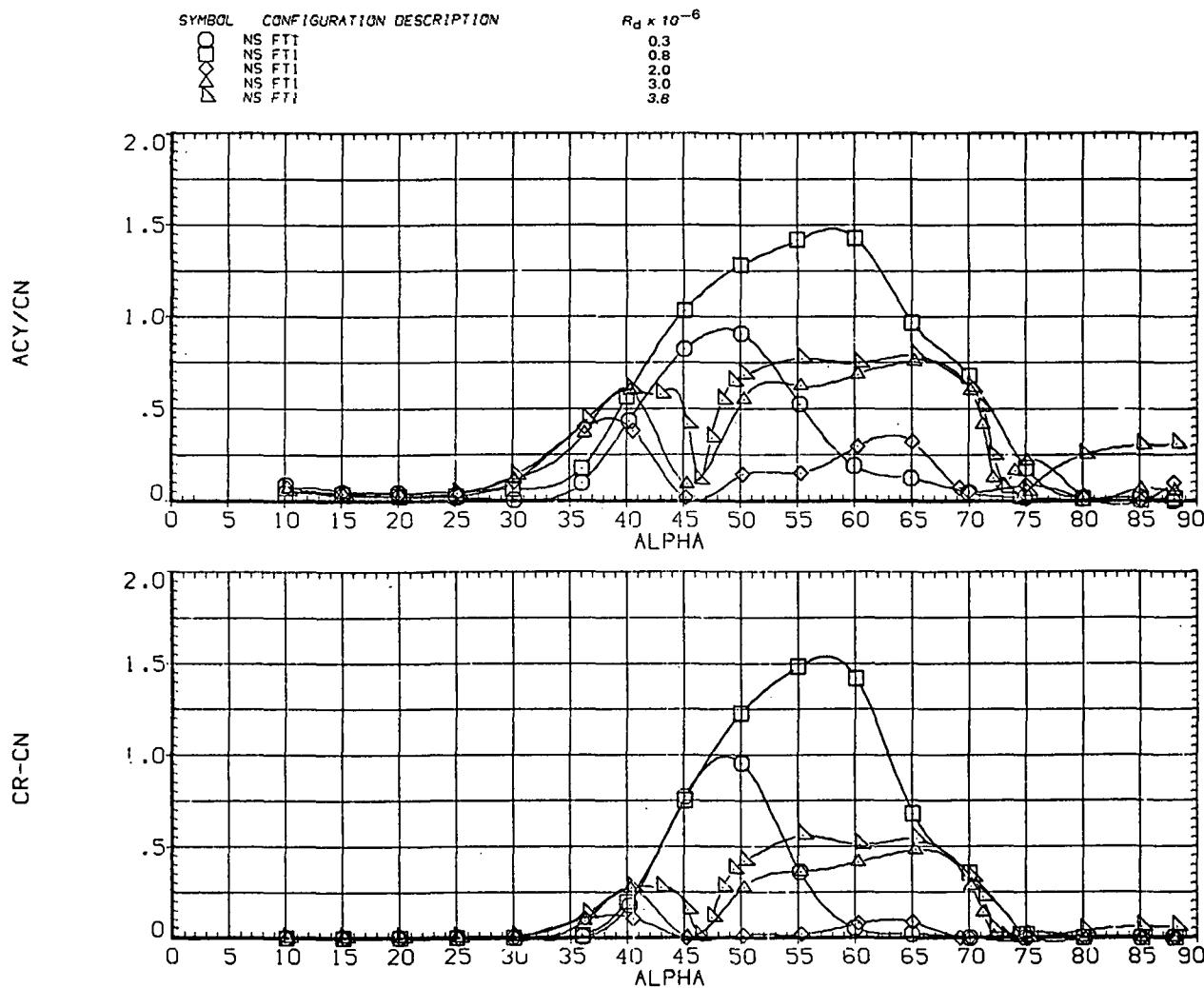
(c) $|C_Y|/C_N$ and $C_R - C_N$ versus α.
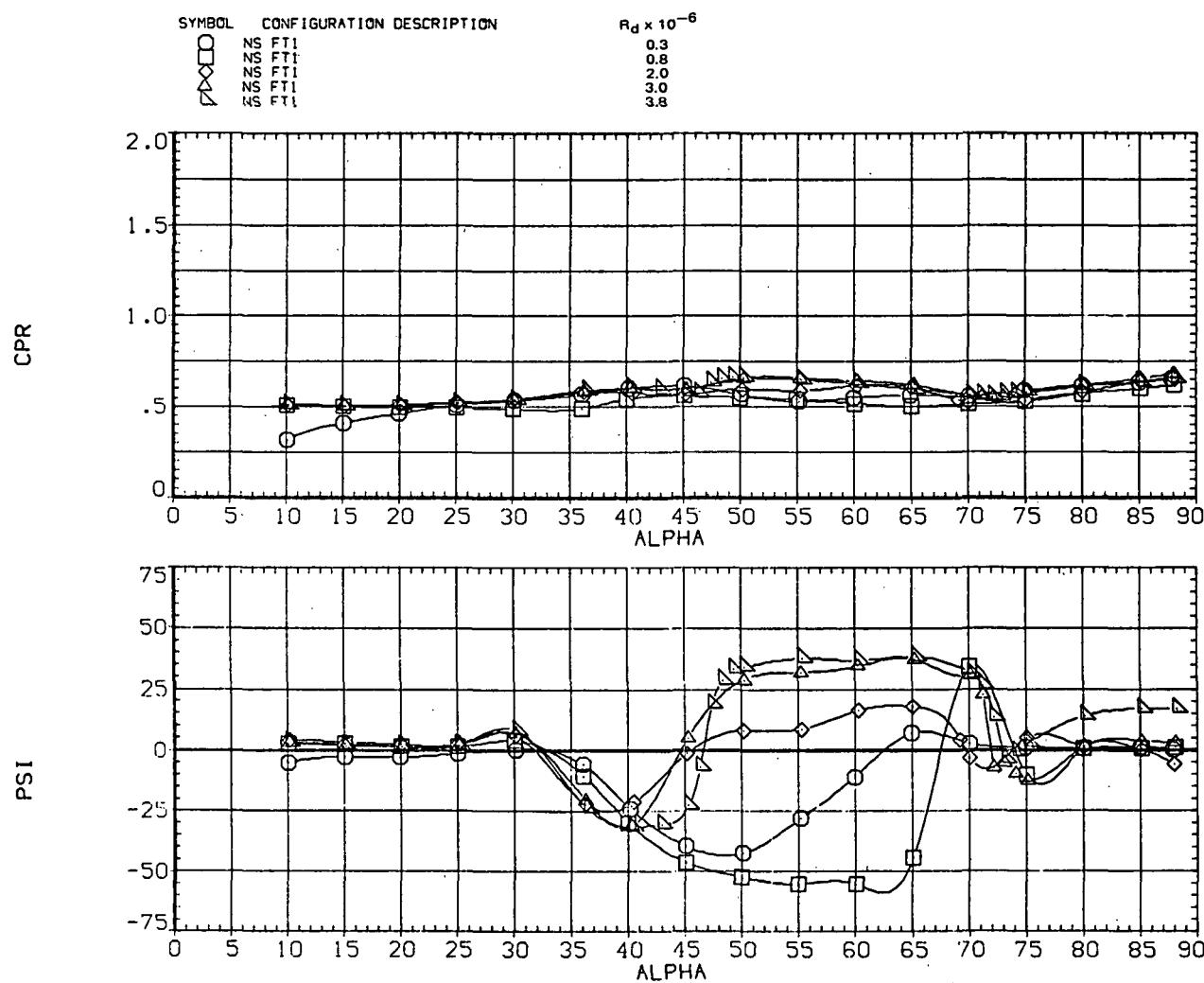
Figure 6.— Continued.

(d) CP_R and Ψ versus α.
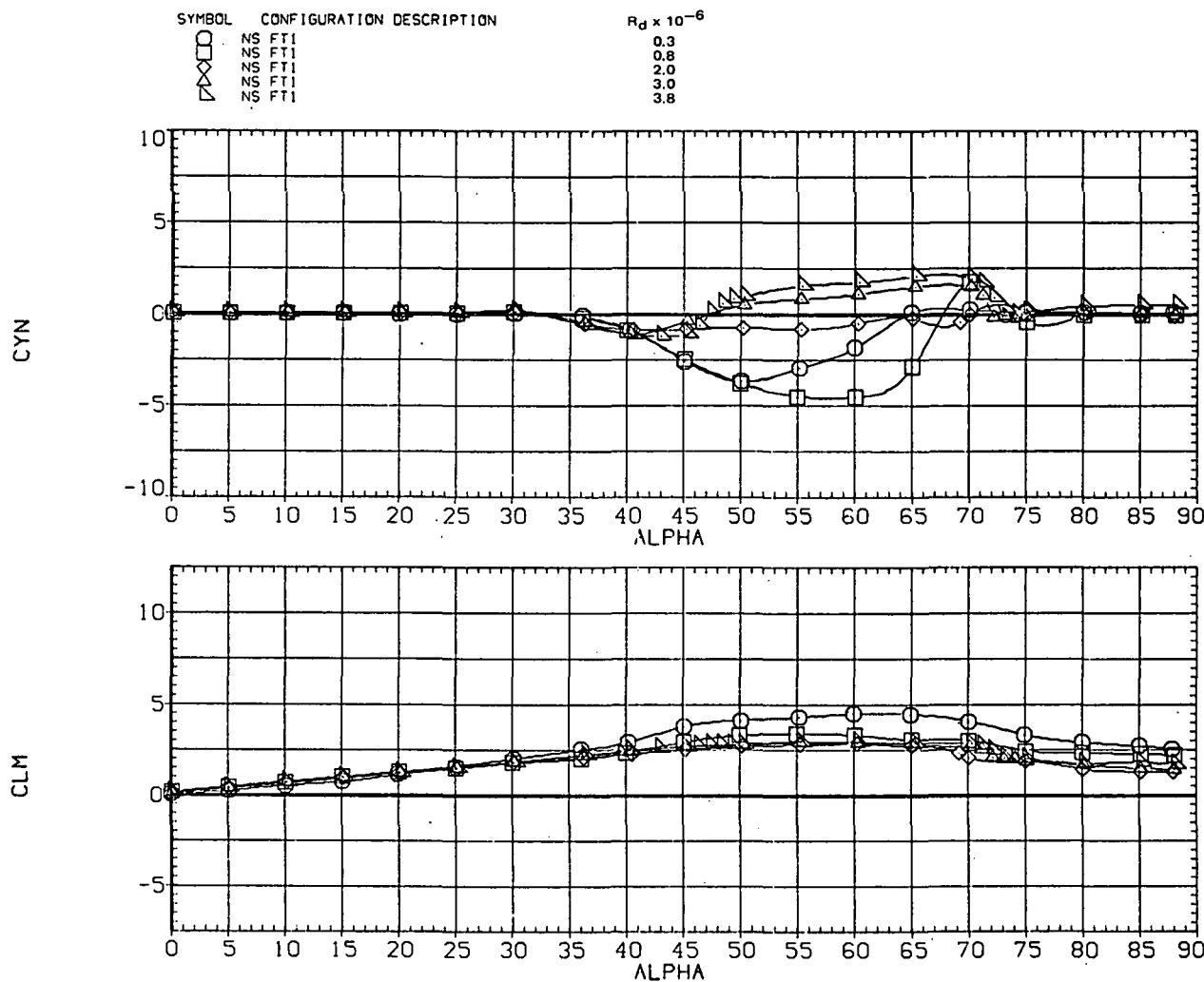
Figure 6.— Continued.

(e) C_n and C_m versus α.
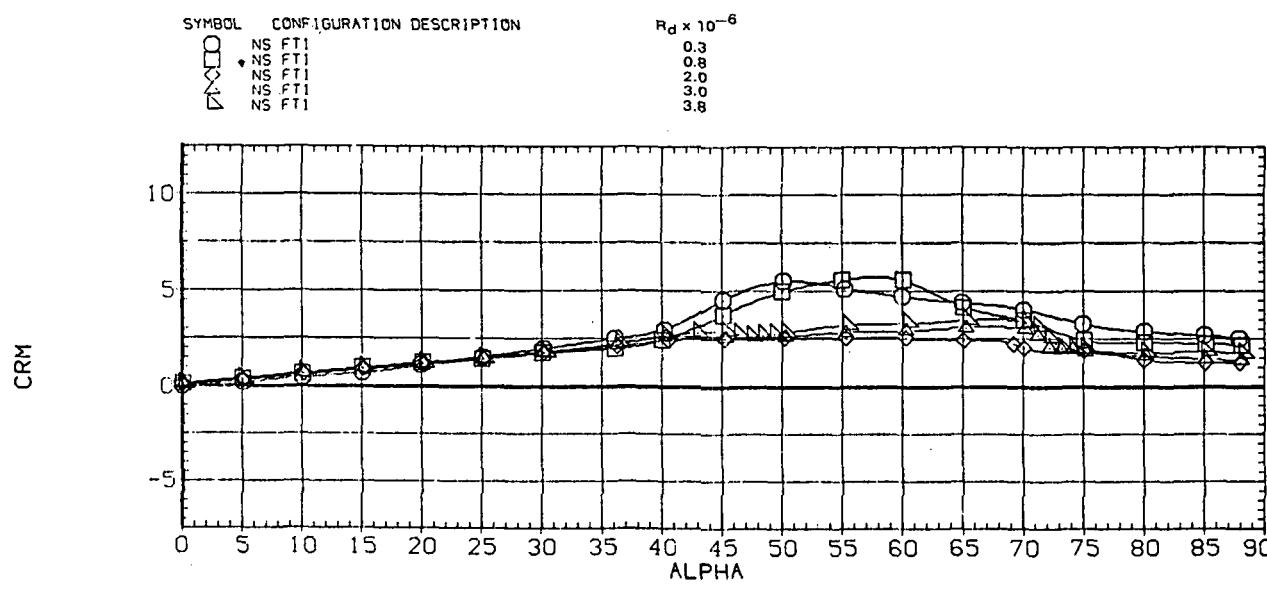
Figure 6.— Continued.

SYMBOL   CONFIGURATION DESCRIPTION $R_d \times 10^{-6}$

○	NS FT1	0.3
□	NS FT1	0.8
◇	NS FT1	2.0
△	NS FT1	3.0
△	NS FT1	3.8

(f) $C_{m,R}$ versus α.

Figure 6.— Continued.

SYMBOL	CONFIGURATION DESCRIPTION	$R_d \times 10^{-6}$
◯	NS FT1	0.3
▢	NS FT1	0.8
◇	NS FT1	2.0
△	NS FT1	3.0
◁	NS FT1	3.8

(g) $C_{p,b}$ and C_{AF} versus α.

Figure 6.— Concluded.

33

SYMBOL   CONFIGURATION DESCRIPTION $R_d \times 10^{-6}$

    NS FTI   0.3
    NS FTI   0.8
    NS FTI   1.1
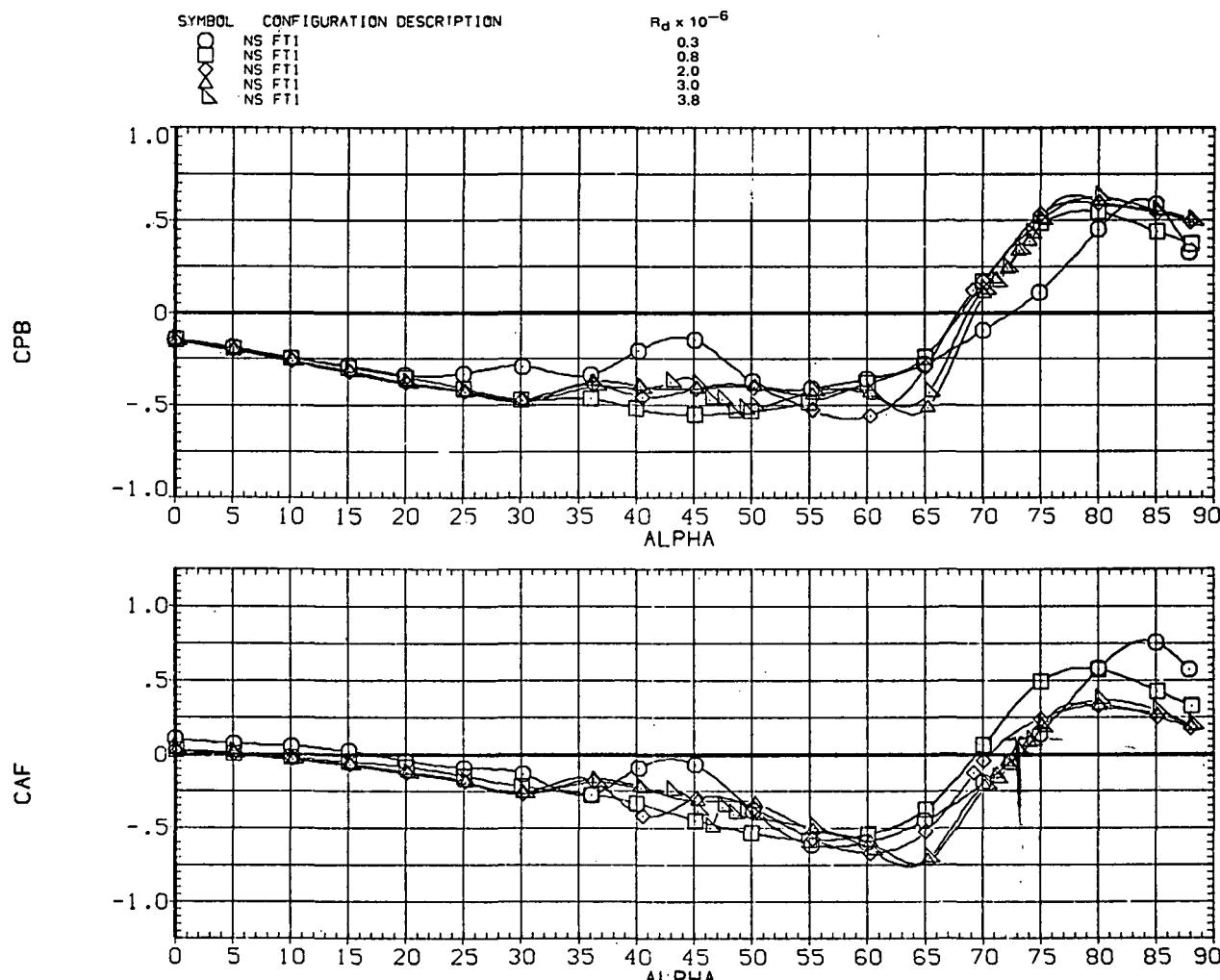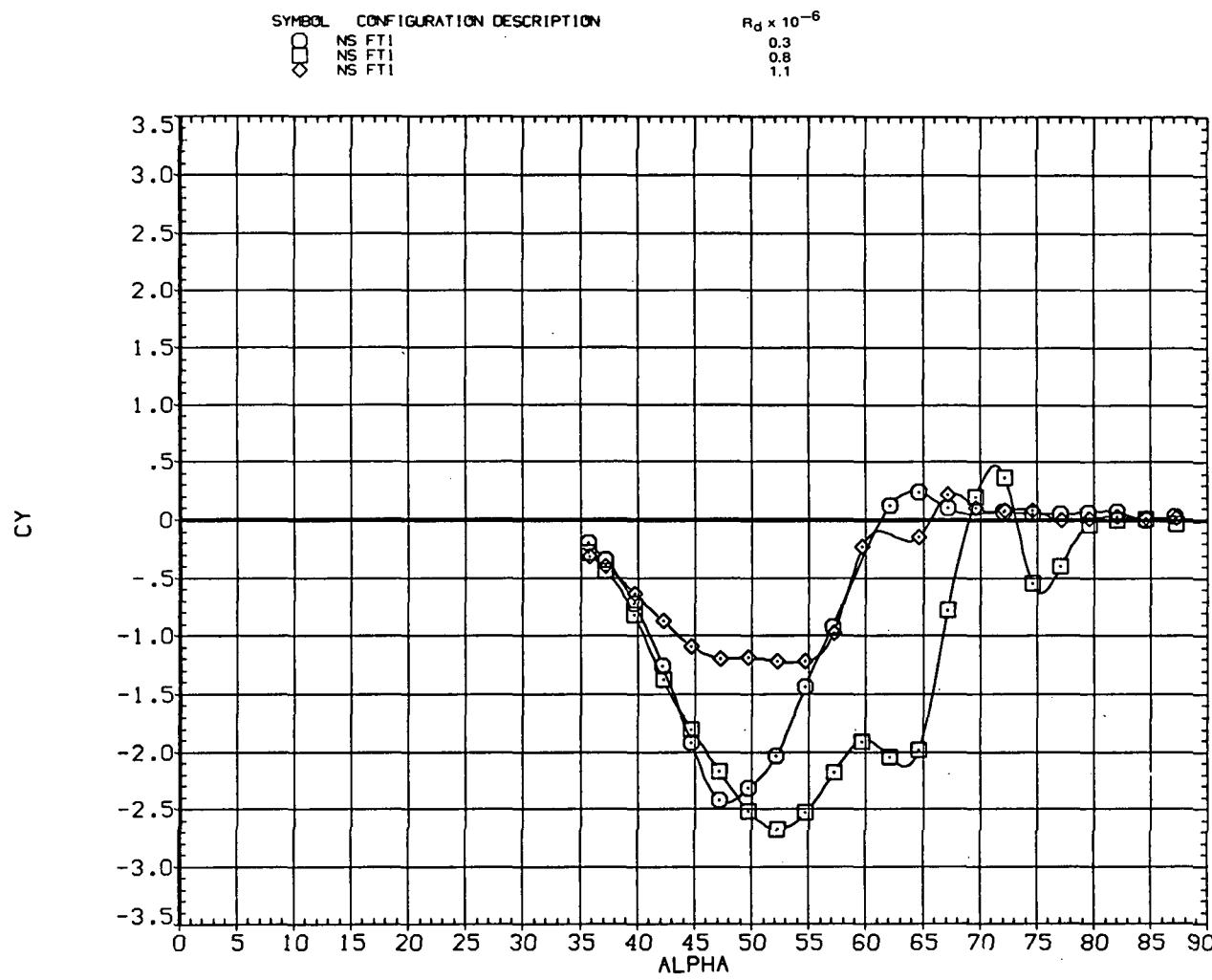
(a) C_Y versus α.

Figure 7.– Effect of Reynolds number; balance B, $M = 0.25$.
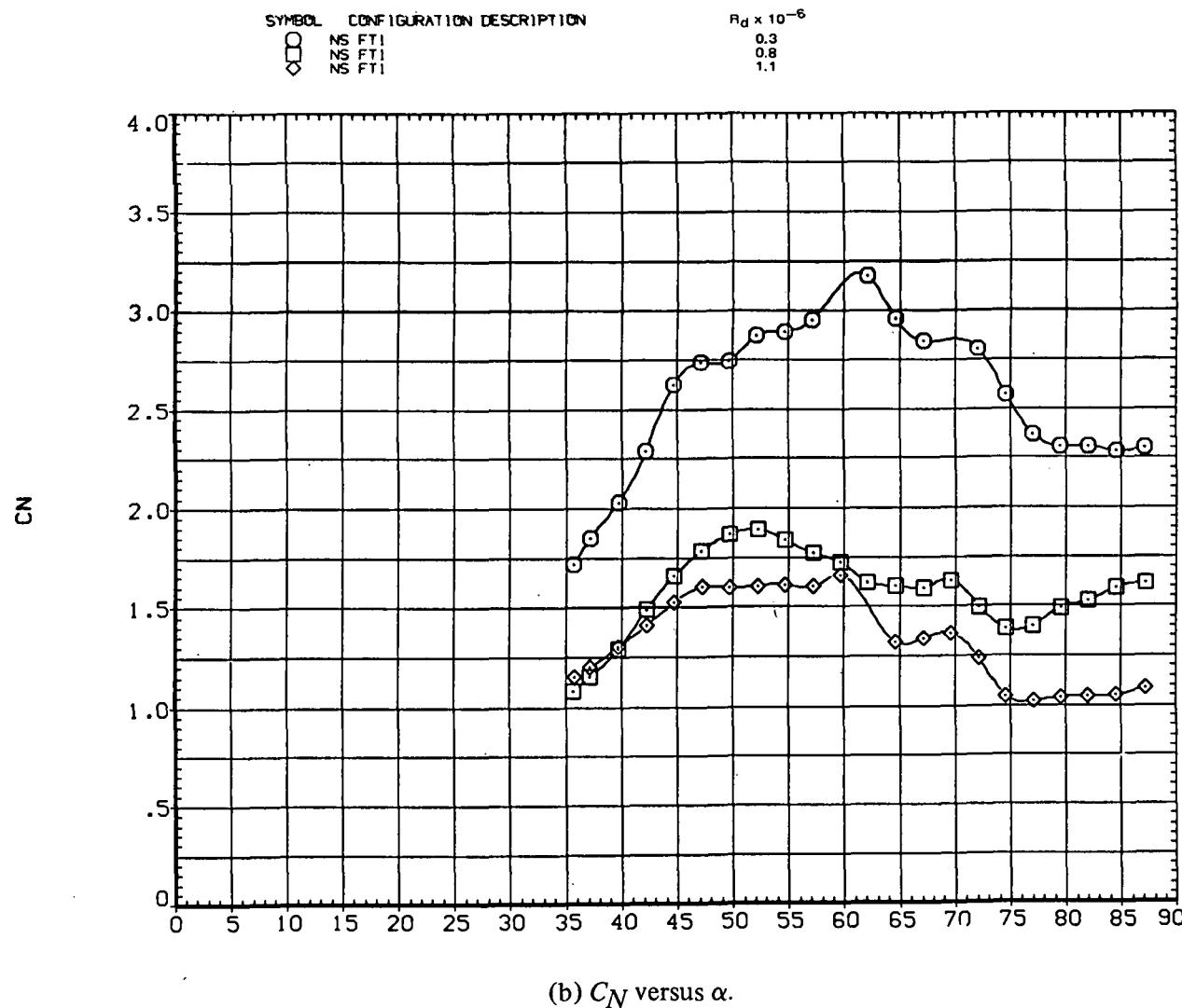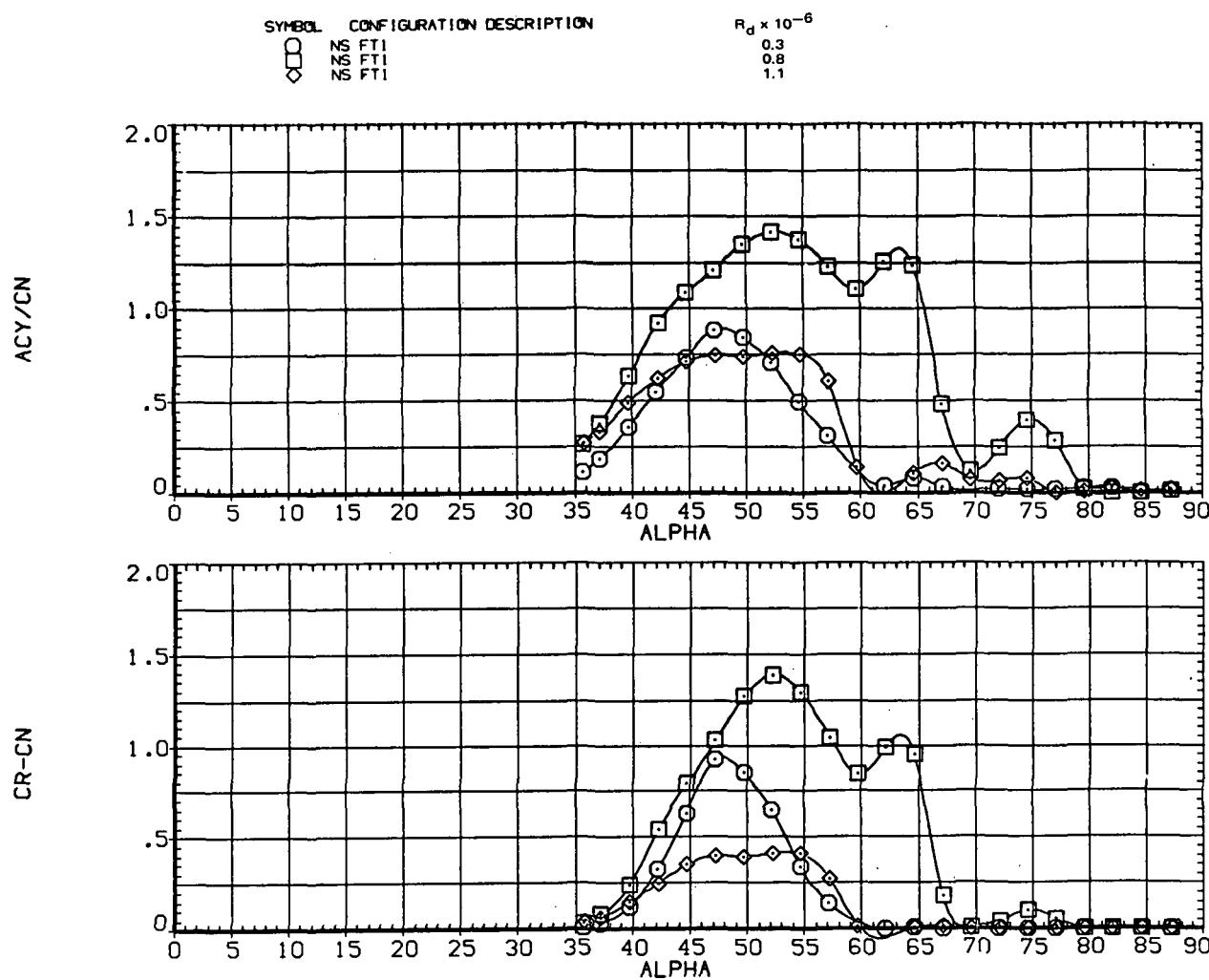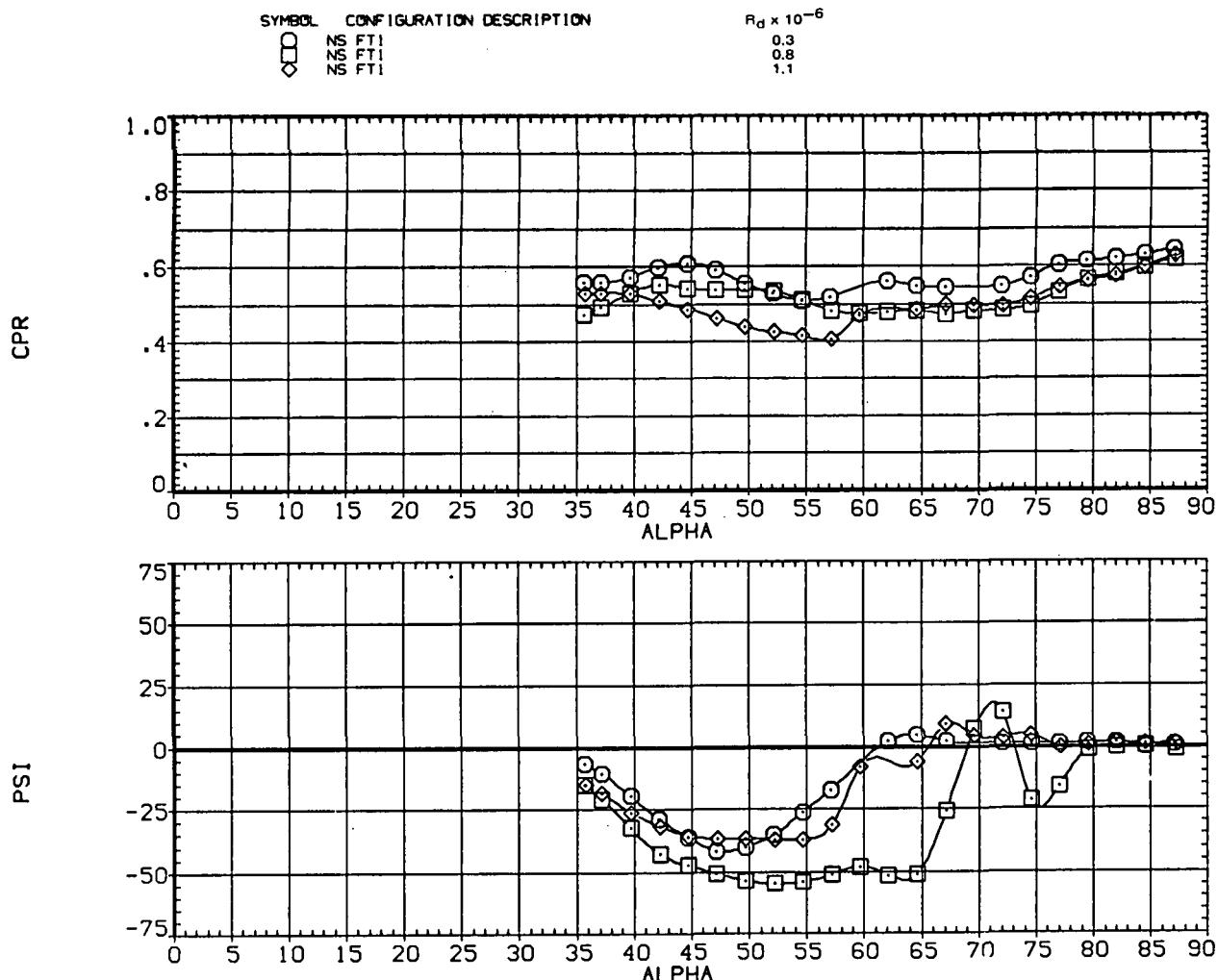
(b) C_N versus α.

Figure 7.— Continued.

SYMBOL	CONFIGURATION DESCRIPTION	$R_d \times 10^{-6}$
⊖	NS FT1	0.3
⊟	NS FT1	0.8
◇	NS FT1	1.1

(c) $|C_Y|/C_N$ and $C_R - C_N$ versus α.

Figure 7.— Continued.

SYMBOL   CONFIGURATION DESCRIPTION $R_d \times 10^{-6}$

	NS FT1	0.3
	NS FT1	0.8
◇	NS FT1	1.1

CPR

ALPHA

PSI

ALPHA

(d) CP_R and Ψ versus α.

Figure 7.– Continued.

(e) C_n versus α.

Figure 7.– Continued.

SYMBOL	CONFIGURATION DESCRIPTION	$R_d \times 10^{-6}$
○	NS FT1	0.3
□	NS FT1	0.8
◇	NS FT1	1.1
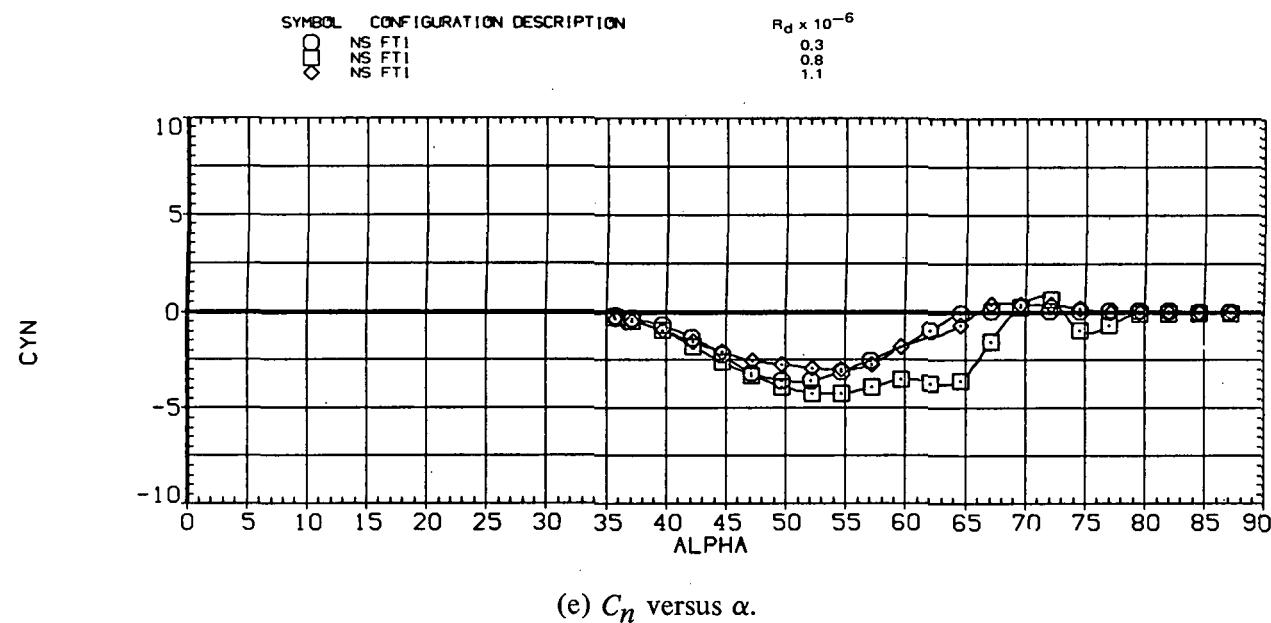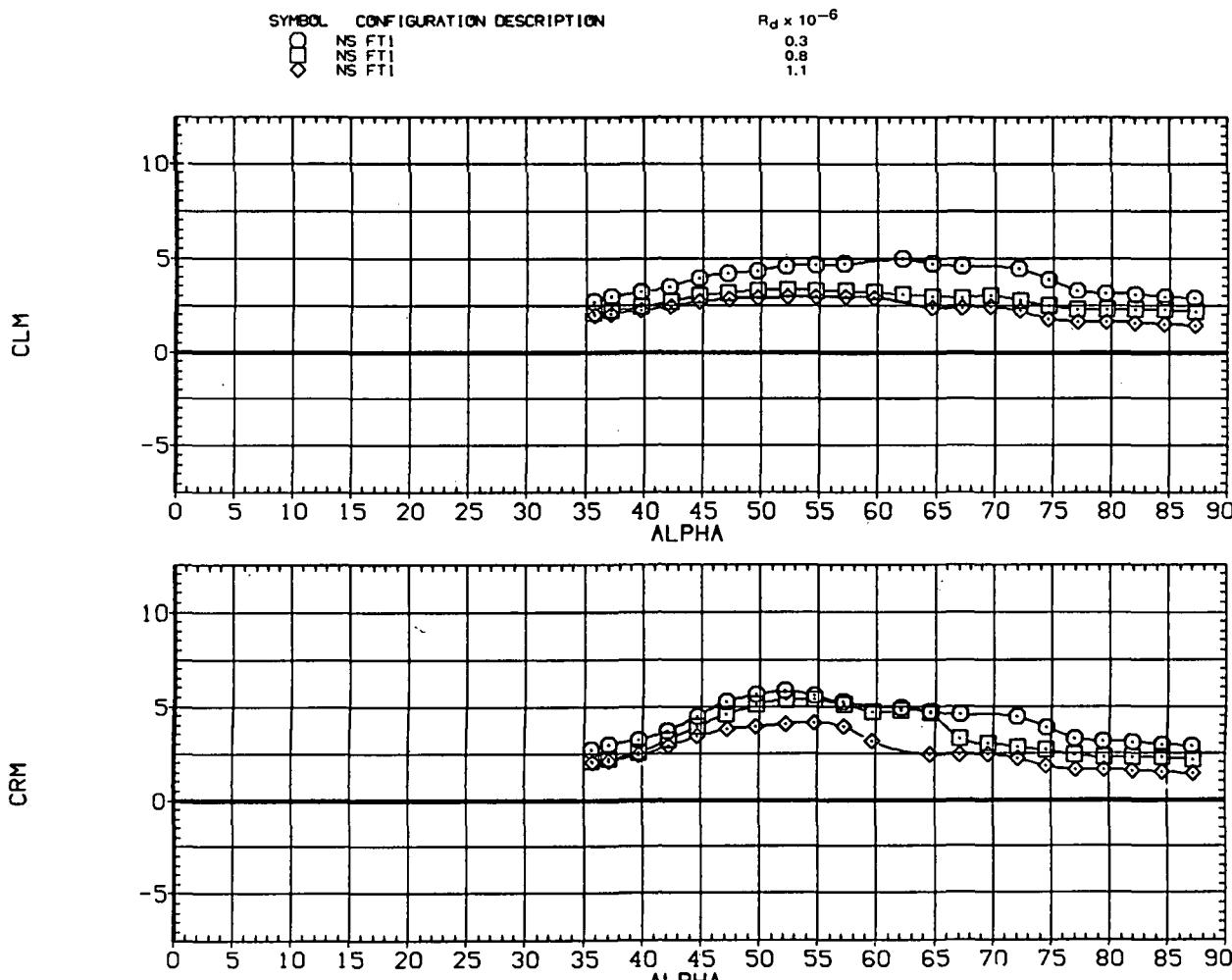
(f) C_m and $C_{m,R}$ versus α.

Figure 7.-- Continued.
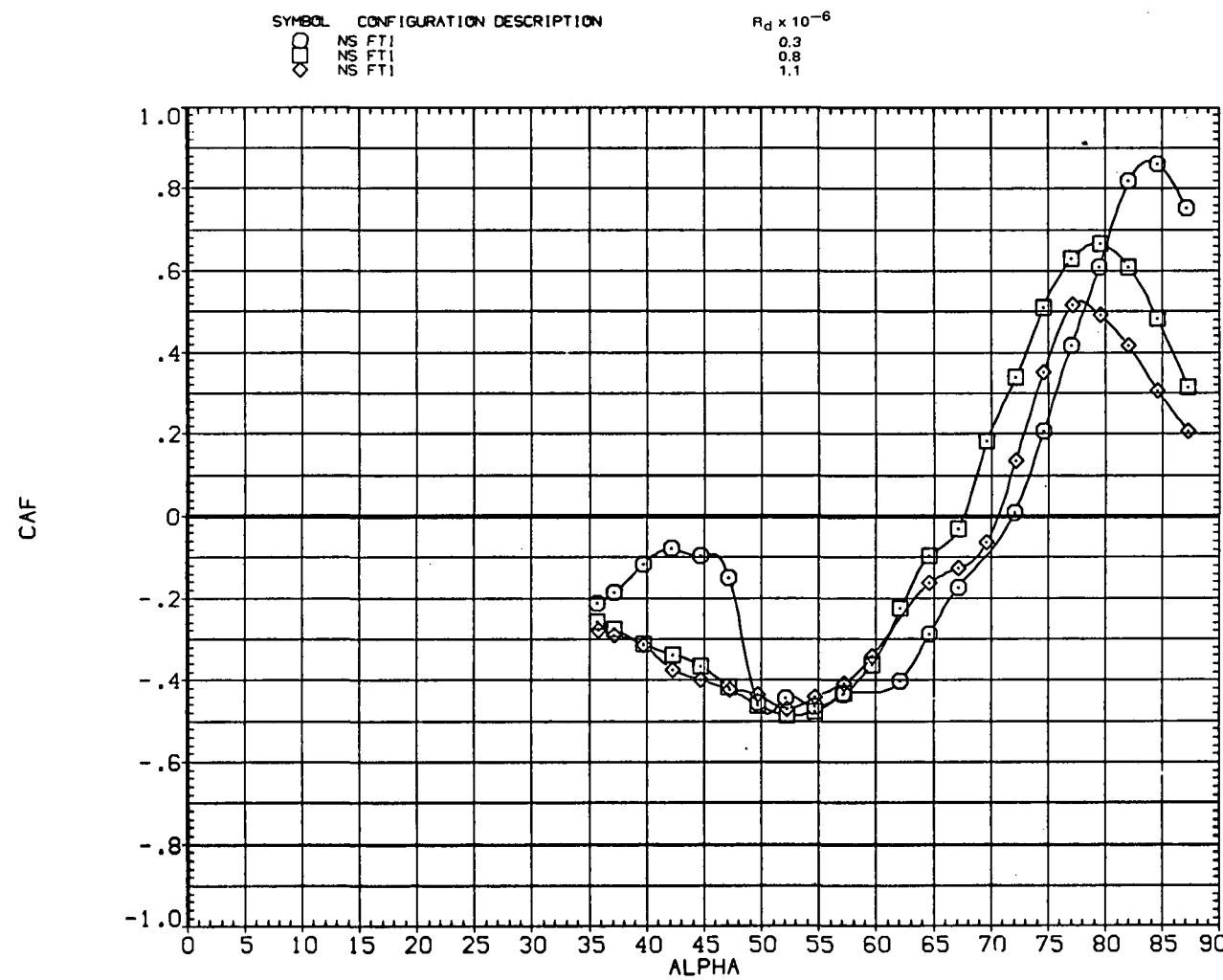
(g) C_{AF} versus α.

Figure 7.– Concluded.
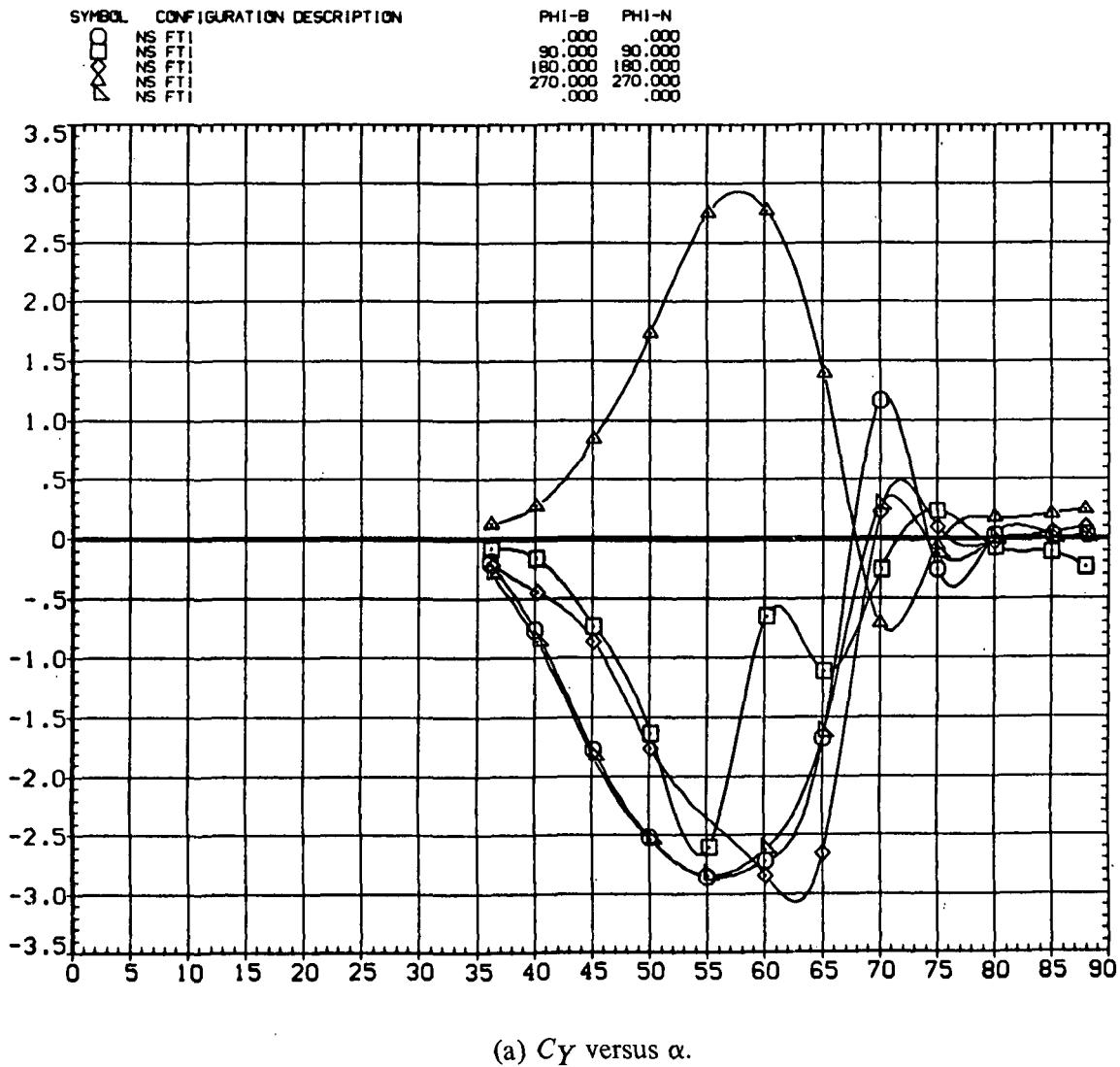
(a) C_Y versus α.

Figure 8.— Effect of roll angle of forebody; $M = 0.25$, $R_d = 0.8 \times 10^6$.
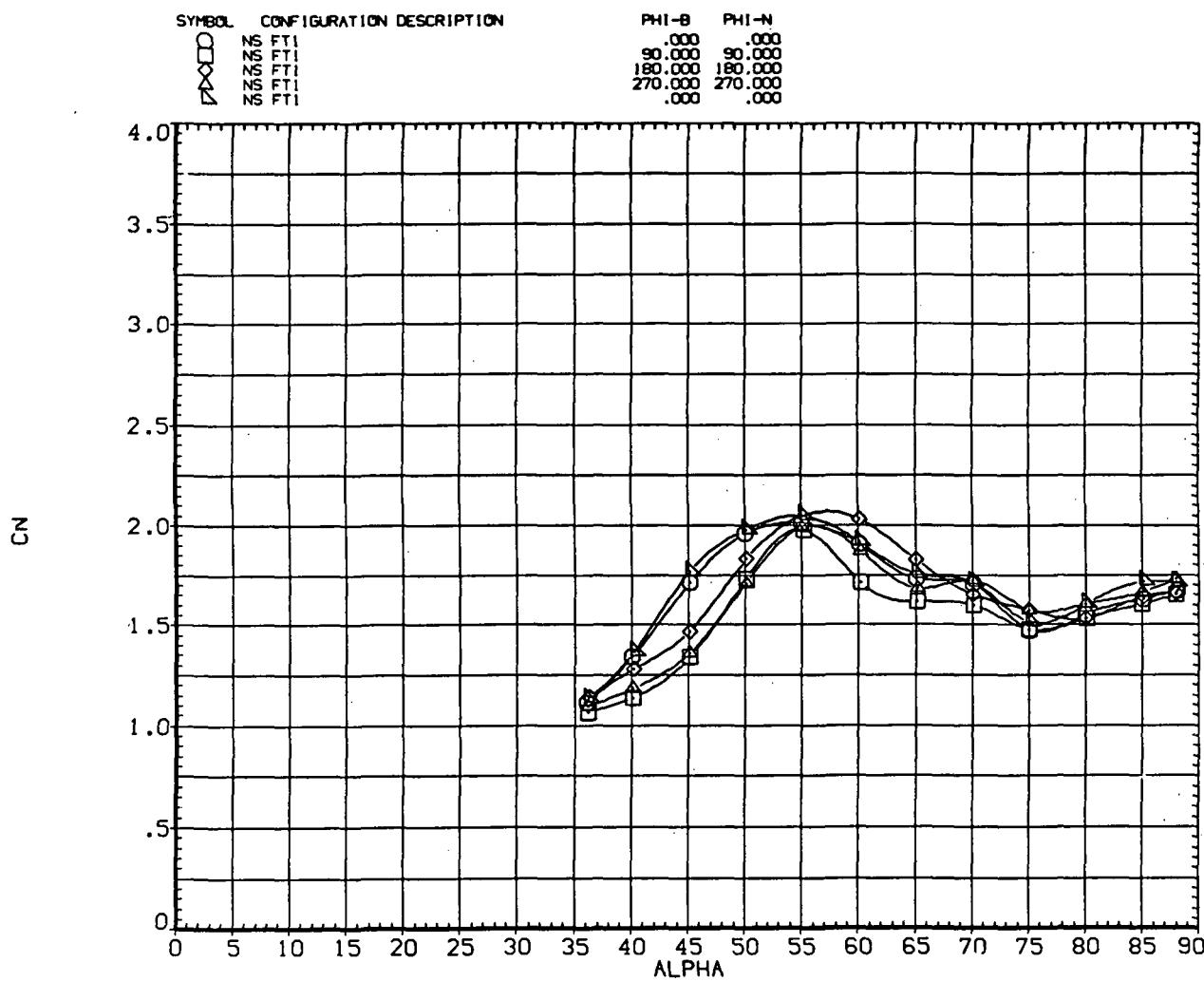
(b) C_N versus α.

Figure 8.– Continued.
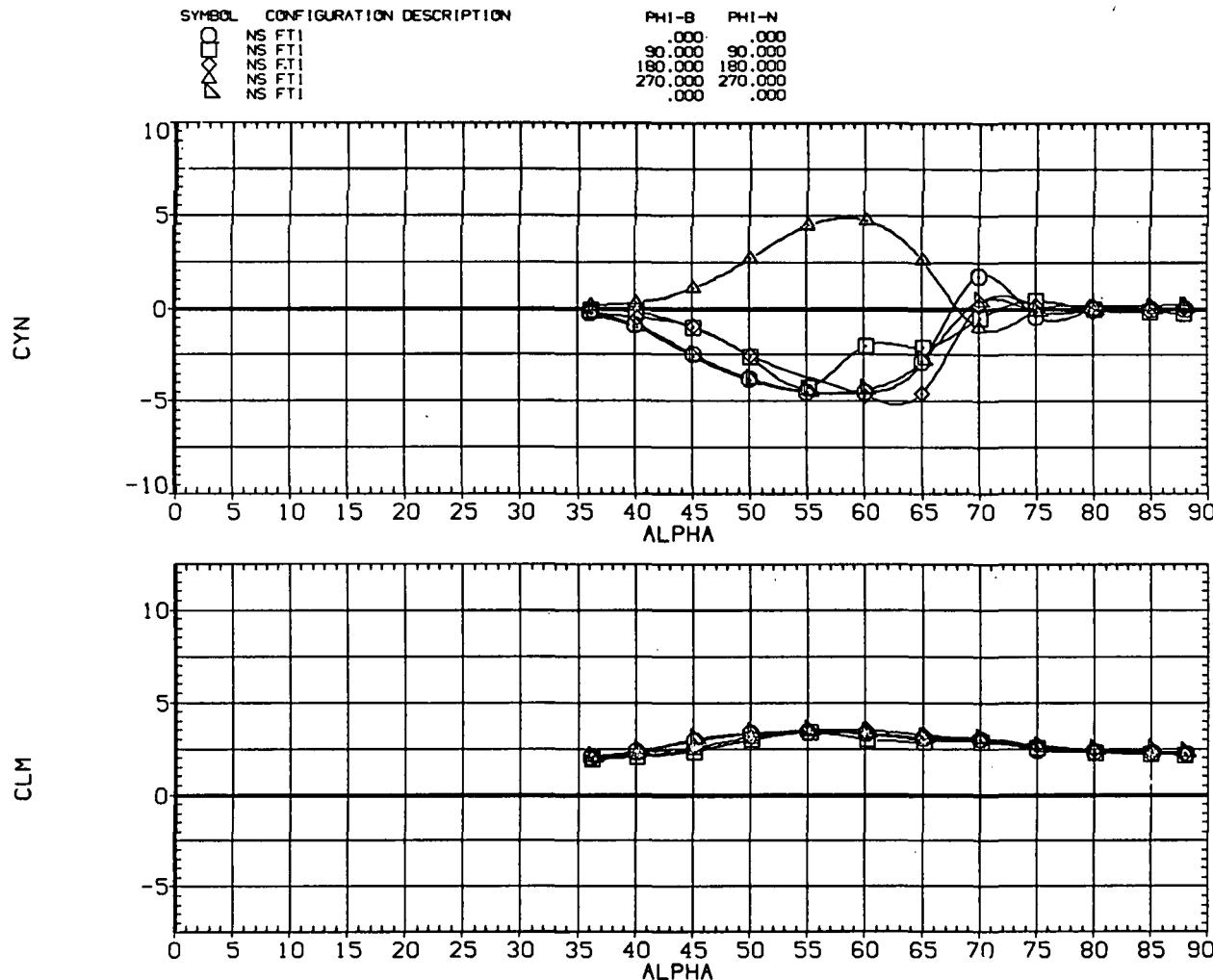
(c) C_n and C_m versus α.

Figure 8.– Concluded.
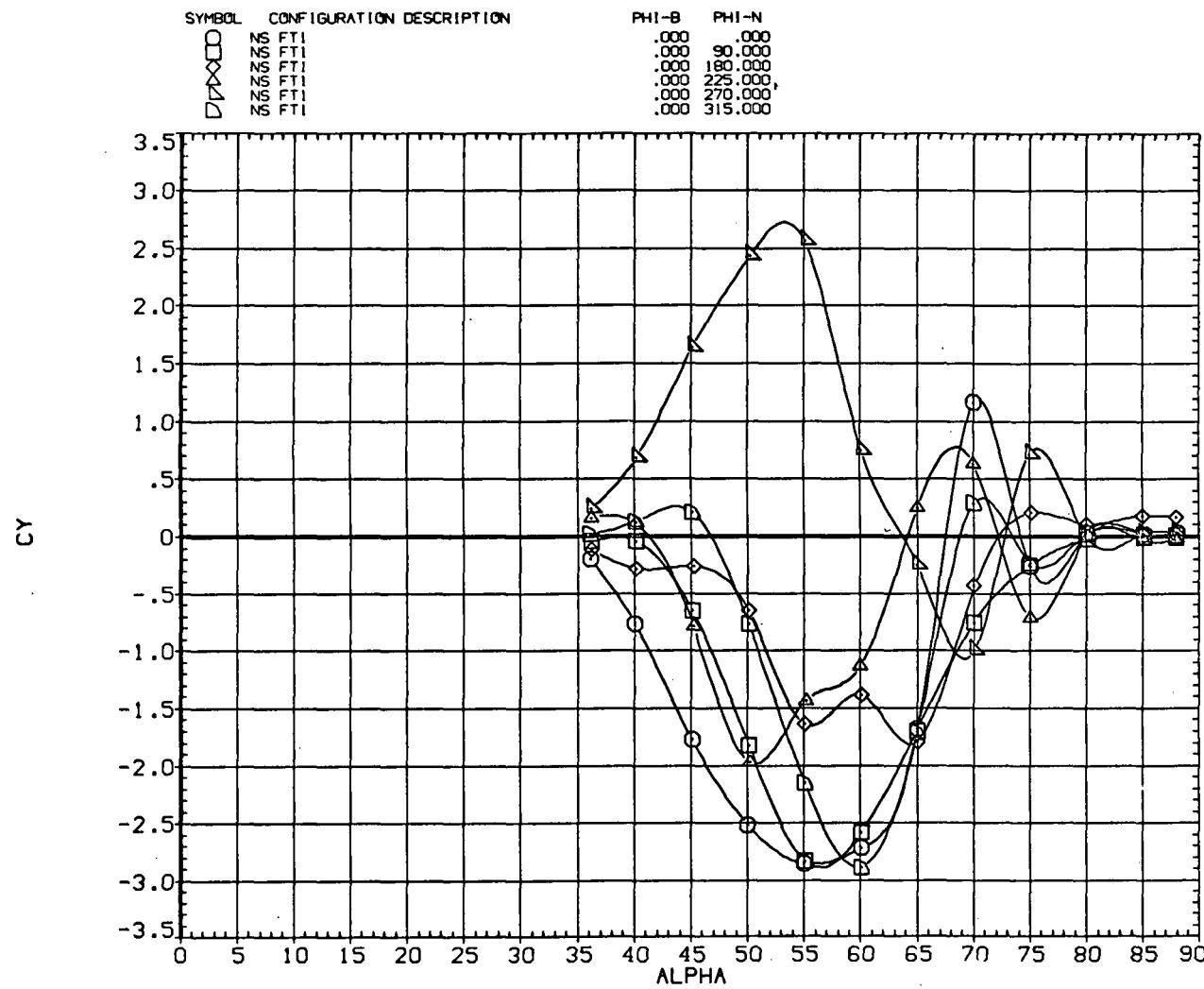
(a) C_Y versus α.

Figure 9.— Effect of roll angle of nose tip section; $M = 0.25$, $R_d = 0.8 \times 10^6$.

SYMBOL   CONFIGURATION DESCRIPTION   PHI-B   PHI-N
            NS FTI   .000   .000
            NS FTI   .000   90.000
            NS FTI   .000   180.000
            NS FTI   .000   225.000
            NS FTI   .000   270.000
            NS FTI   .000   315.000

CN

4.0

3.5

3.0

2.5

2.0

1.5

1.0

.5

0

0   5   10   15   20   25   30   35   40   45   50   55   60   65   70   75   80   85   90
ALPHA

(b) C_N versus α.

Figure 9.– Continued.

SYMBOL   CONFIGURATION DESCRIPTION   PHI-B   PHI-N
         NS FT1   .000   .000
         NS FT1   .000   90.000
         NS FT1   .000   180.000
         NS FT1   .000   225.000
         NS FT1   .000   270.000
         NS FT1   .000   315.000
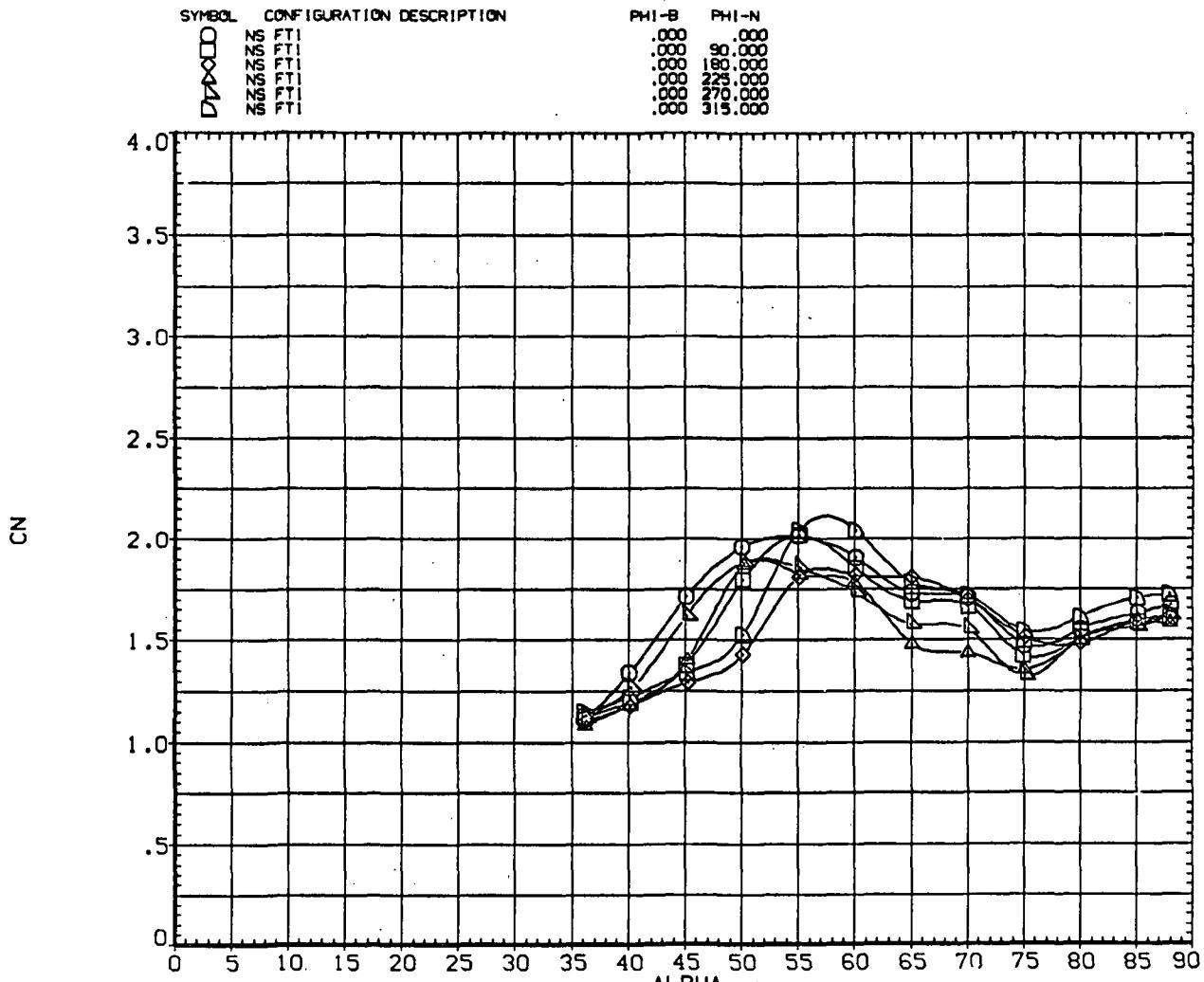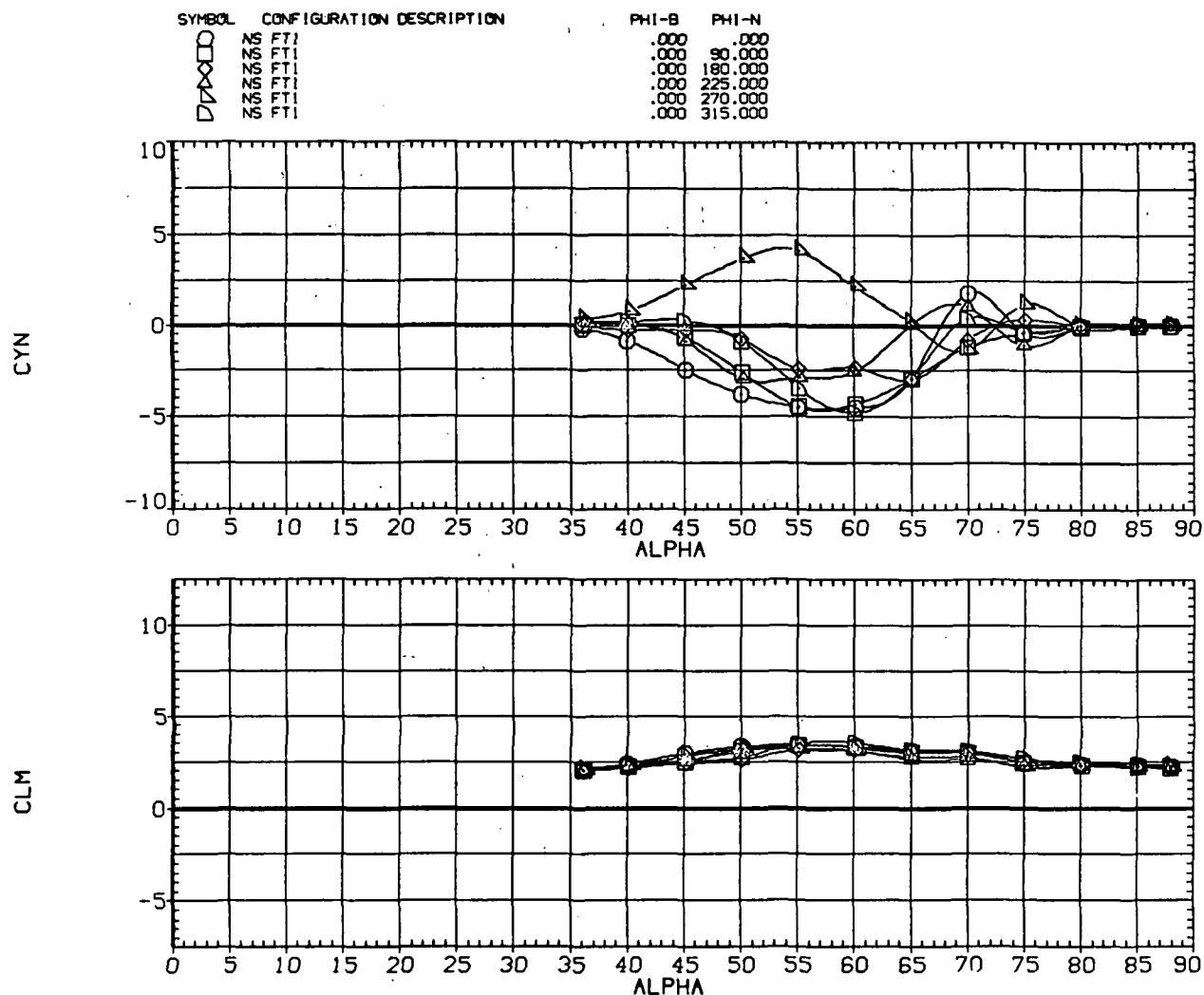
(c) C_n and C_m versus α.

Figure 9.— Concluded.
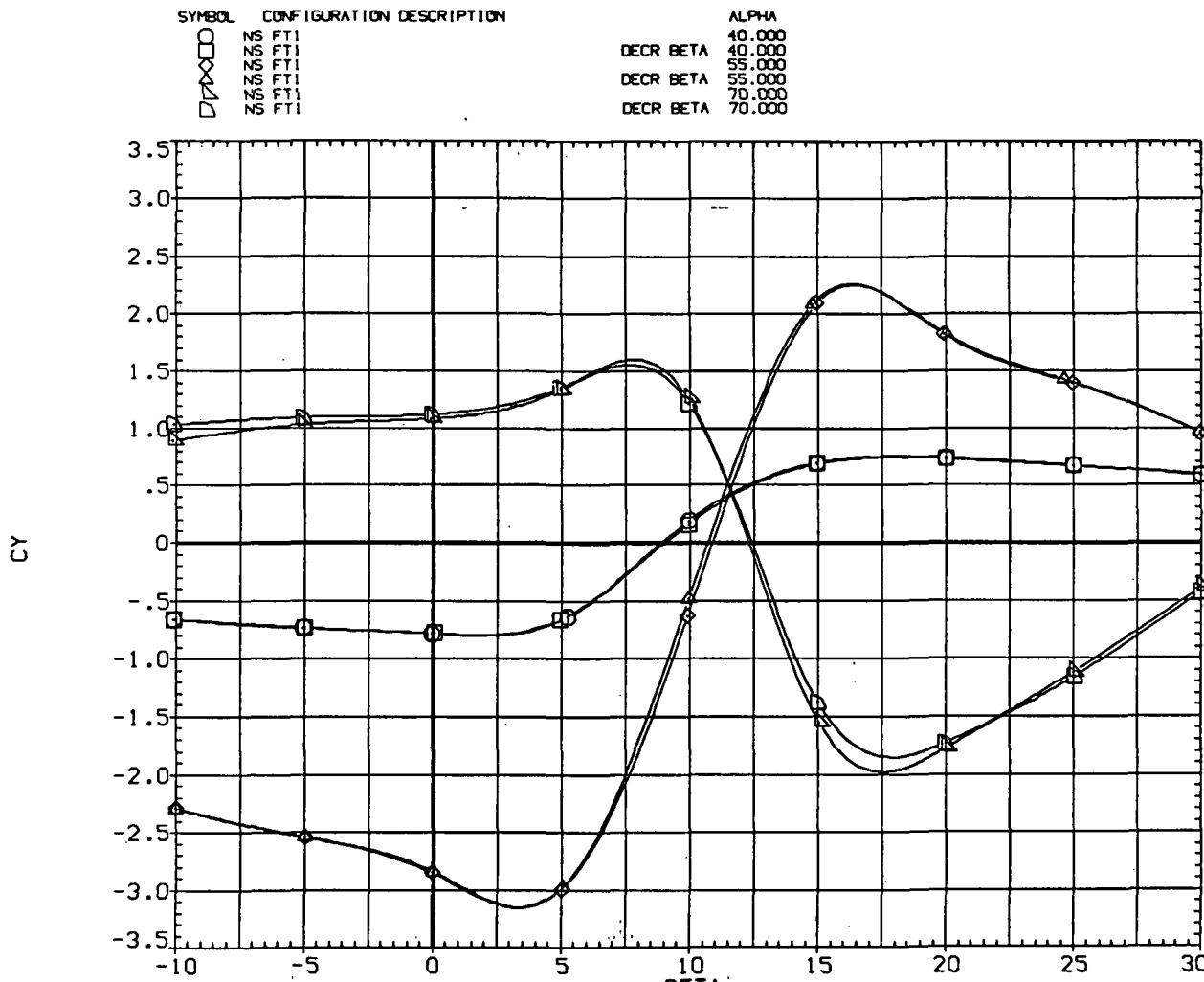
(a) C_Y versus α.

Figure 10.— Effect of angle of sideslip; $M = 0.25, R_d = 0.8 \times 10^6$.

SYMBOL   CONFIGURATION DESCRIPTION   ALPHA

SYMBOL	CONFIGURATION DESCRIPTION	ALPHA
○	NS FT1	40.000
⊟	NS FT1 DECR BETA	40.000
⊠	NS FT1	55.000
△	NS FT1 DECR BETA	55.000
△	NS FT1	70.000
▽	NS FT1 DECR BETA	70.000
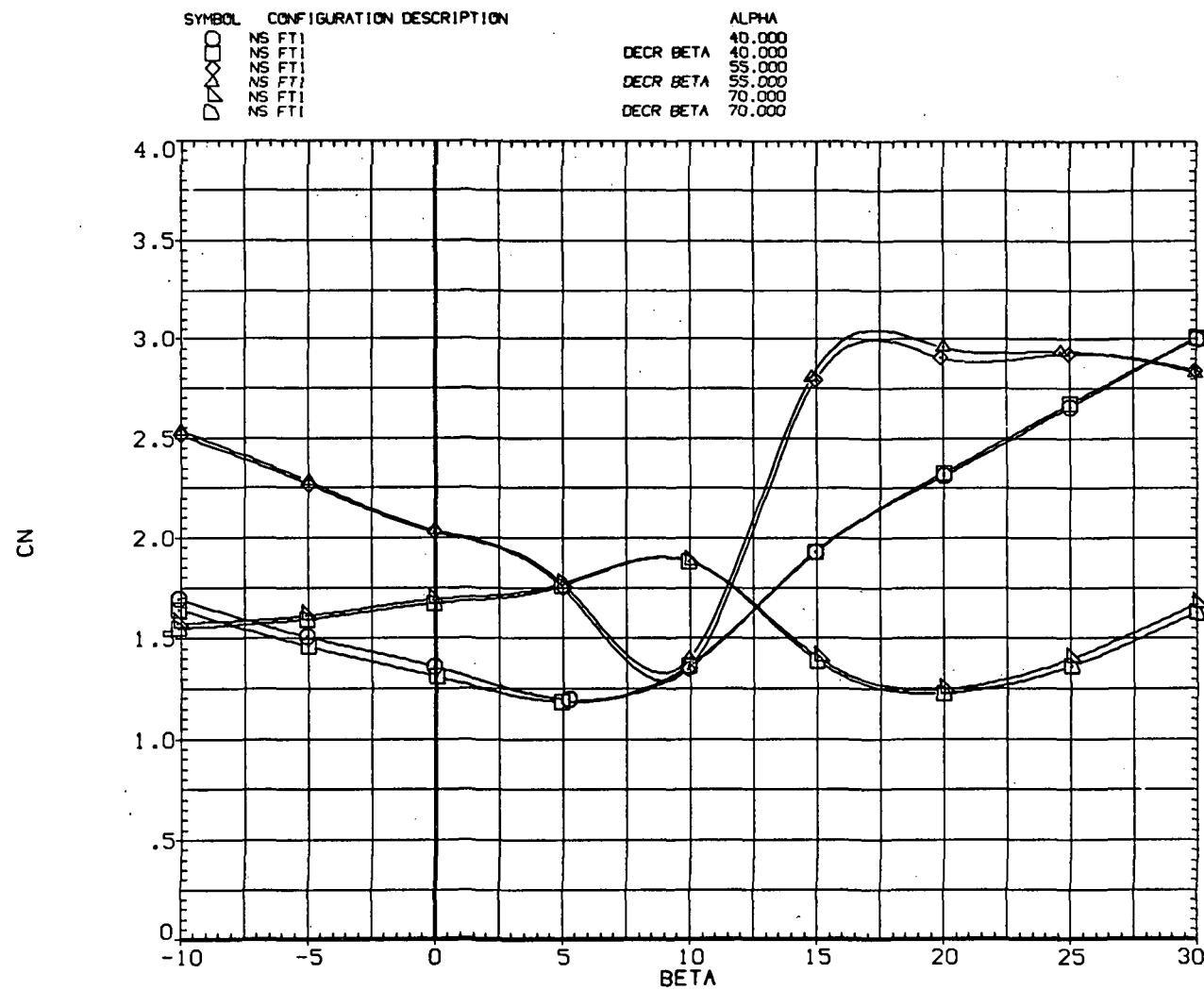
(b) C_N versus α.

Figure 10.– Continued.
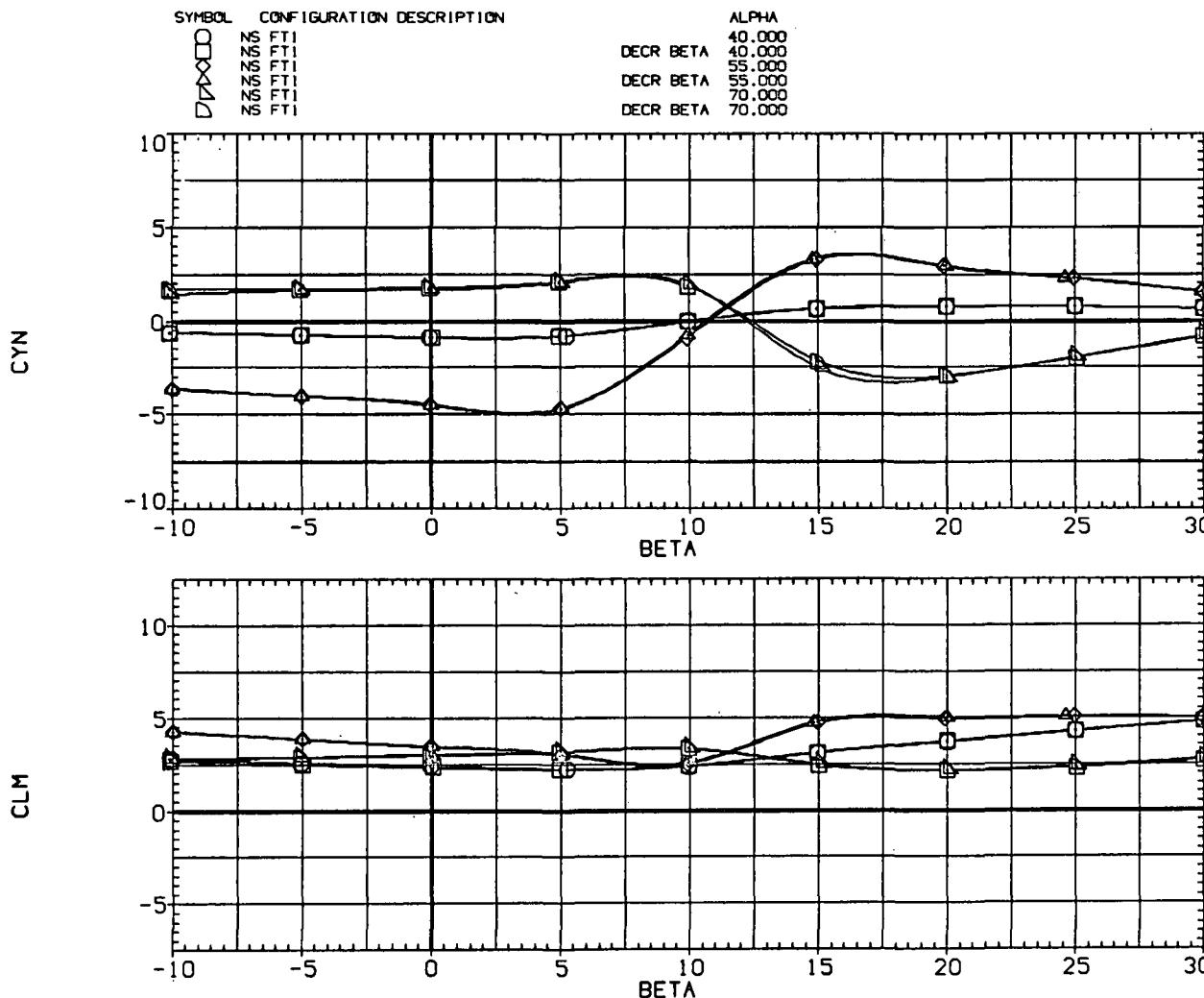
(c) C_n and C_m versus α.

Figure 10.— Concluded.
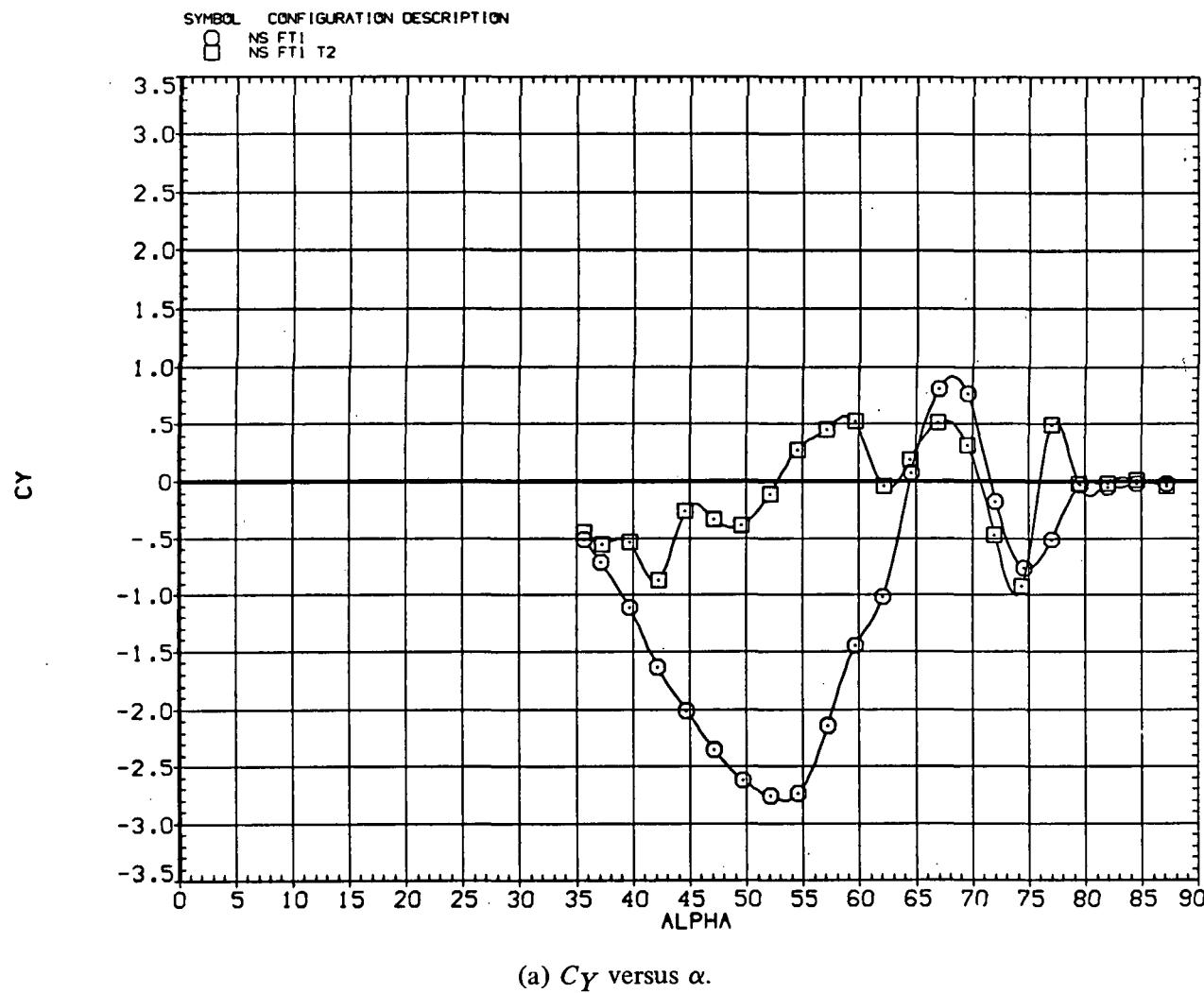
(a) C_Y versus α.

Figure 11.— Effect of boundary-layer transition strips; $M = 0.25$, $R_d = 0.8 \times 10^6$, $\Theta = \pm 15°$.

(b) C_N versus α.

Figure 11.— Continued.

SYMBOL   CONFIGURATION DESCRIPTION
    NS FT1
    NS FT1 T2
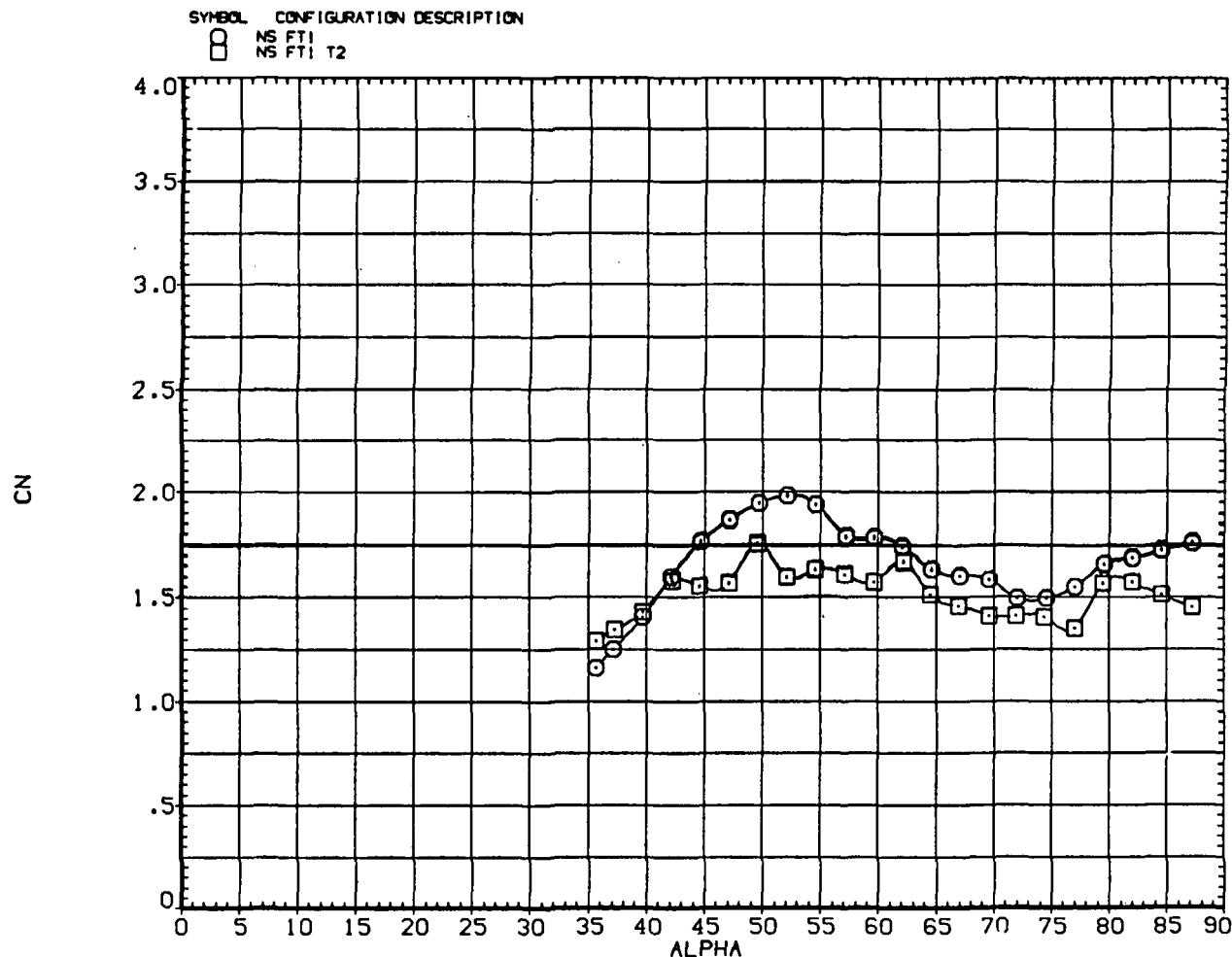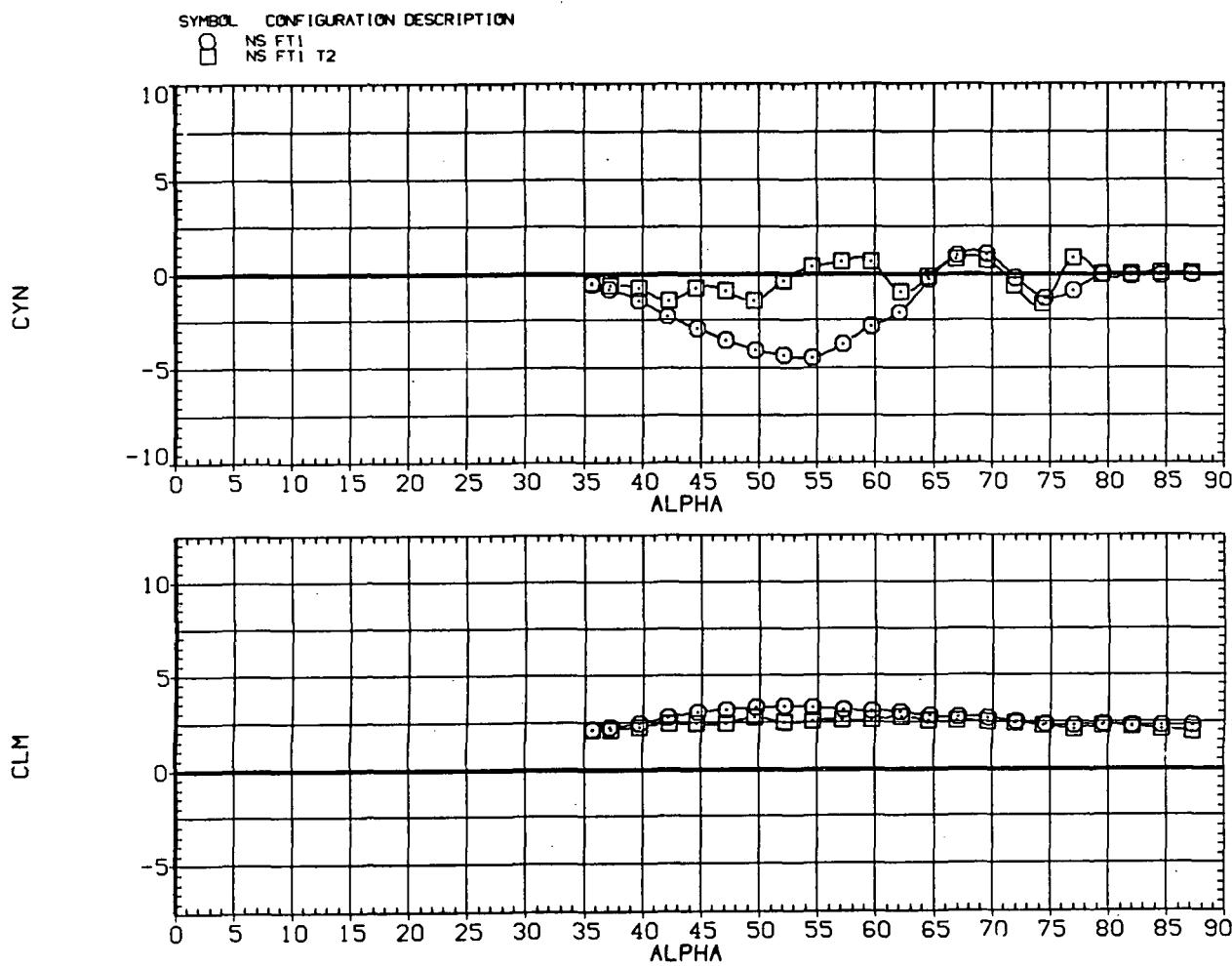
(c) C_n and C_m versus α.

Figure 11.— Concluded.
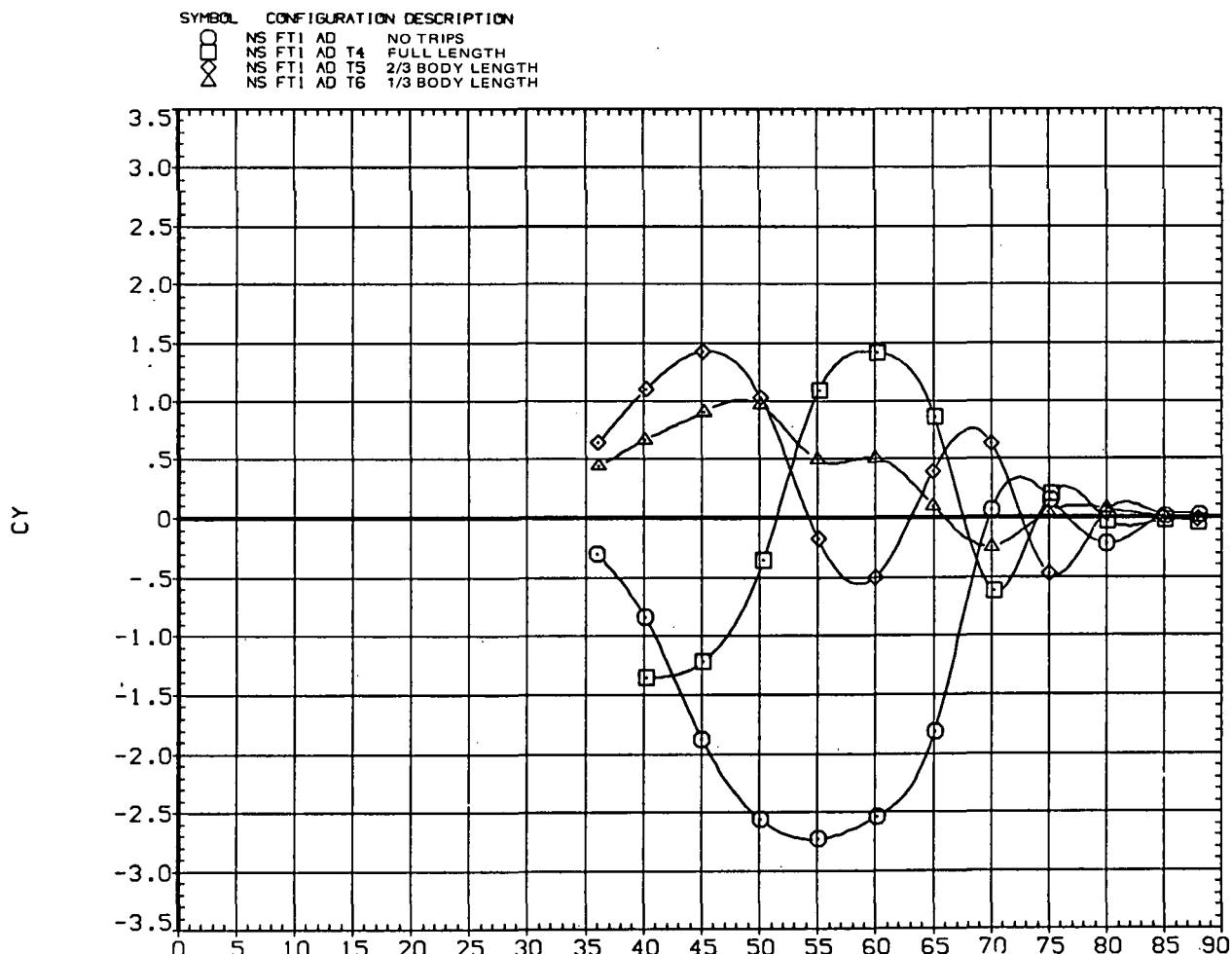
(a) C_Y versus α.

Figure 12.— Effect of length on boundary-layer transition strips; $M = 0.25$, $R_d = 0.8 \times 10^6$, $\Theta = \pm 30°$.

SYMBOL   CONFIGURATION DESCRIPTION

○	NS FT1 AD		NO TRIPS
□	NS FT1 AD	T4	FULL LENGTH
◇	NS FT1 AD	T5	2/3 BODY LENGTH
△	NS FT1 AD	T6	1/3 BODY LENGTH
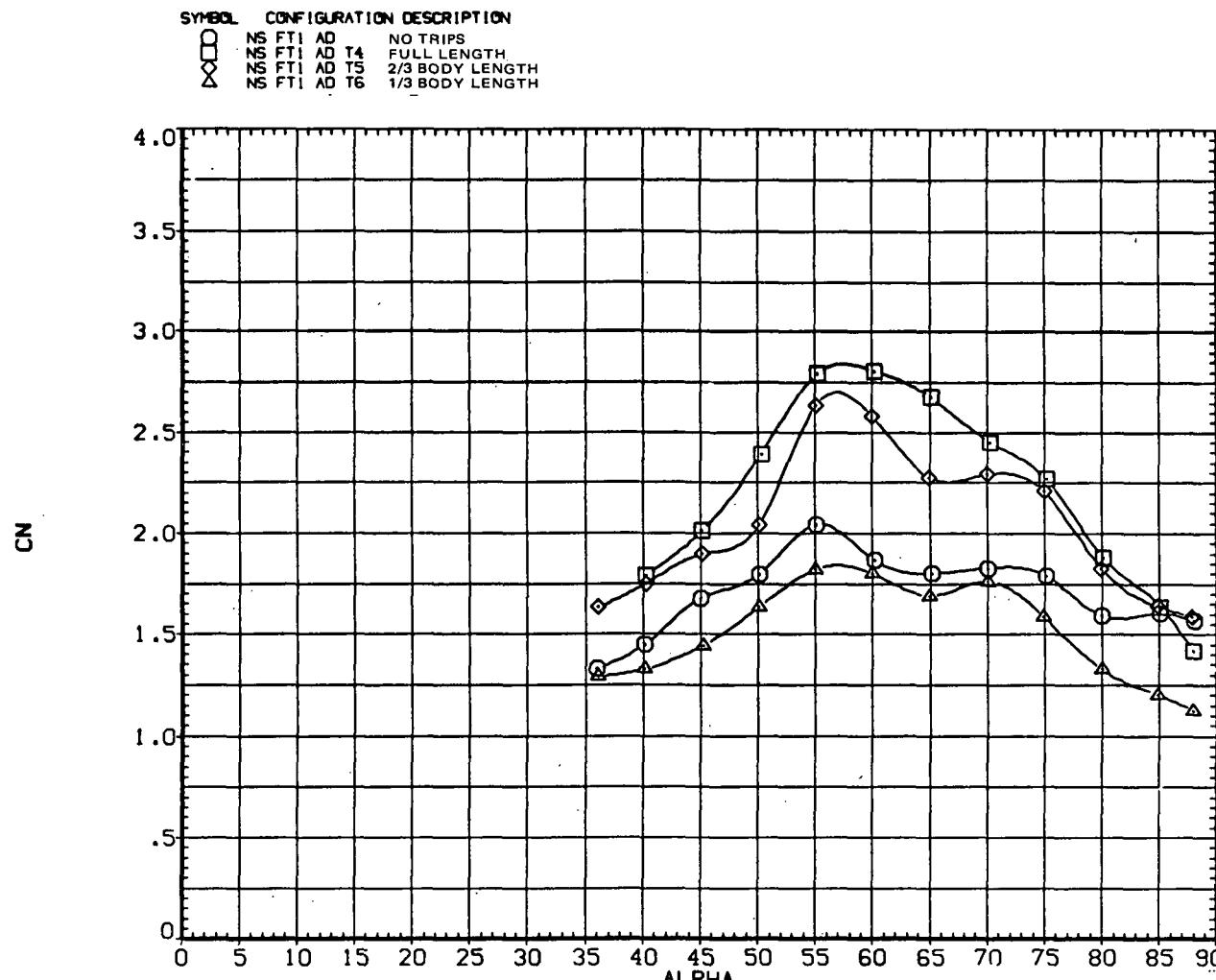
(b) C_N versus α.

Figure 12.– Continued.

(c) C_n and C_m versus α.

Figure 12.– Concluded.

SYMBOL   CONFIGURATION DESCRIPTION   x/ℓ
  ◯   NS FT1 T8   0.05
  ▢   NS FT1 T9   0.09
  ◇   NS FT1 T10   0.14
  △   NS FT1 T11   0.19
  ◁   NS FT1 T12   0.28
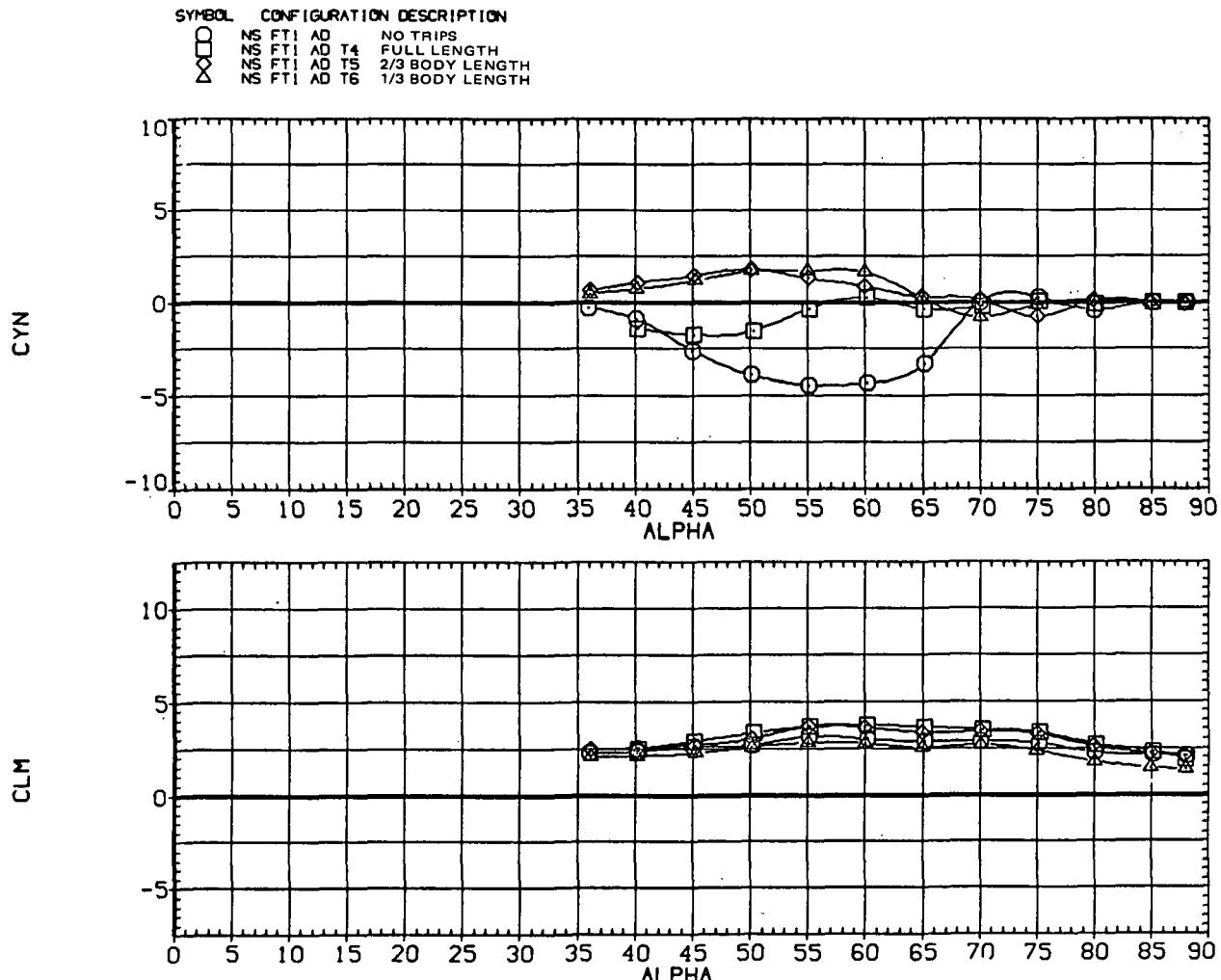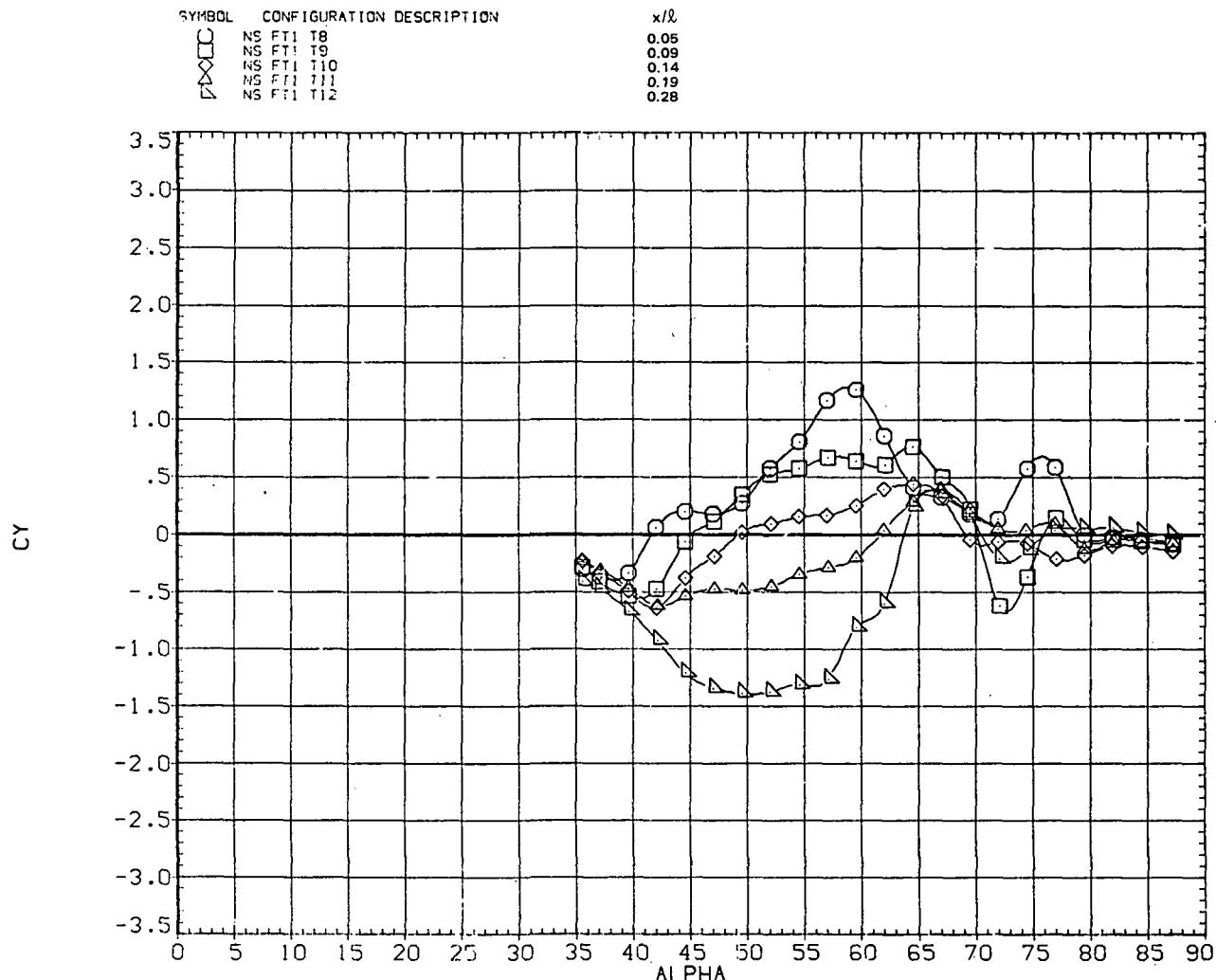
(a) C_Y versus α.

Figure 13.— Effect of a boundary-layer transition-strip ring around the forebody at various locations; $M = 0.25$, $R_d = 0.8 \times 10^6$.

(b) C_N versus α.

Figure 13.– Continued.

SYMBOL   CONFIGURATION DESCRIPTION   x/ℓ
  NS FT1 T8   0.05
  NS FT1 T9   0.09
  NS FT1 T10   0.14
  NS FT1 T11   0.19
  NS FT1 T12   0.28
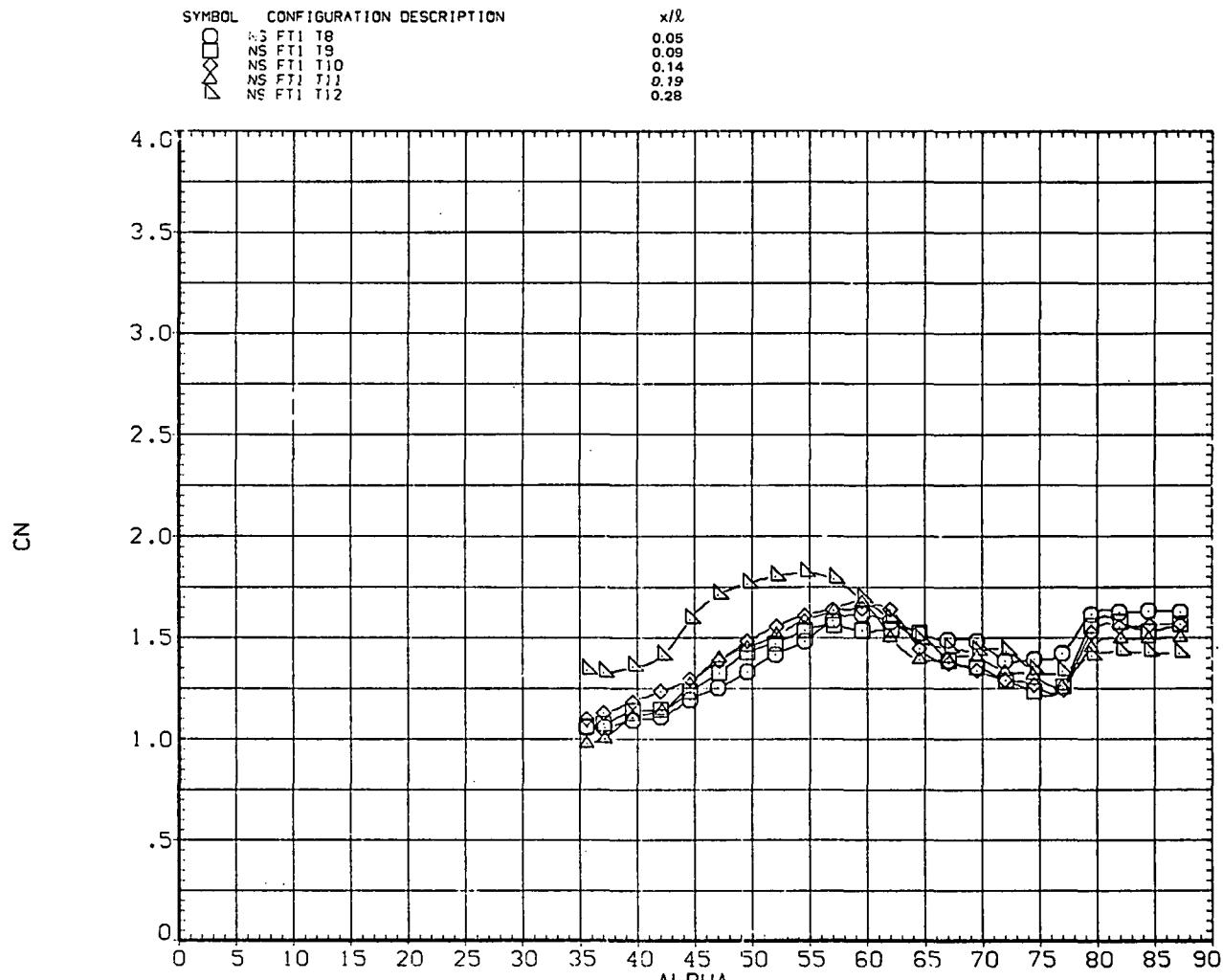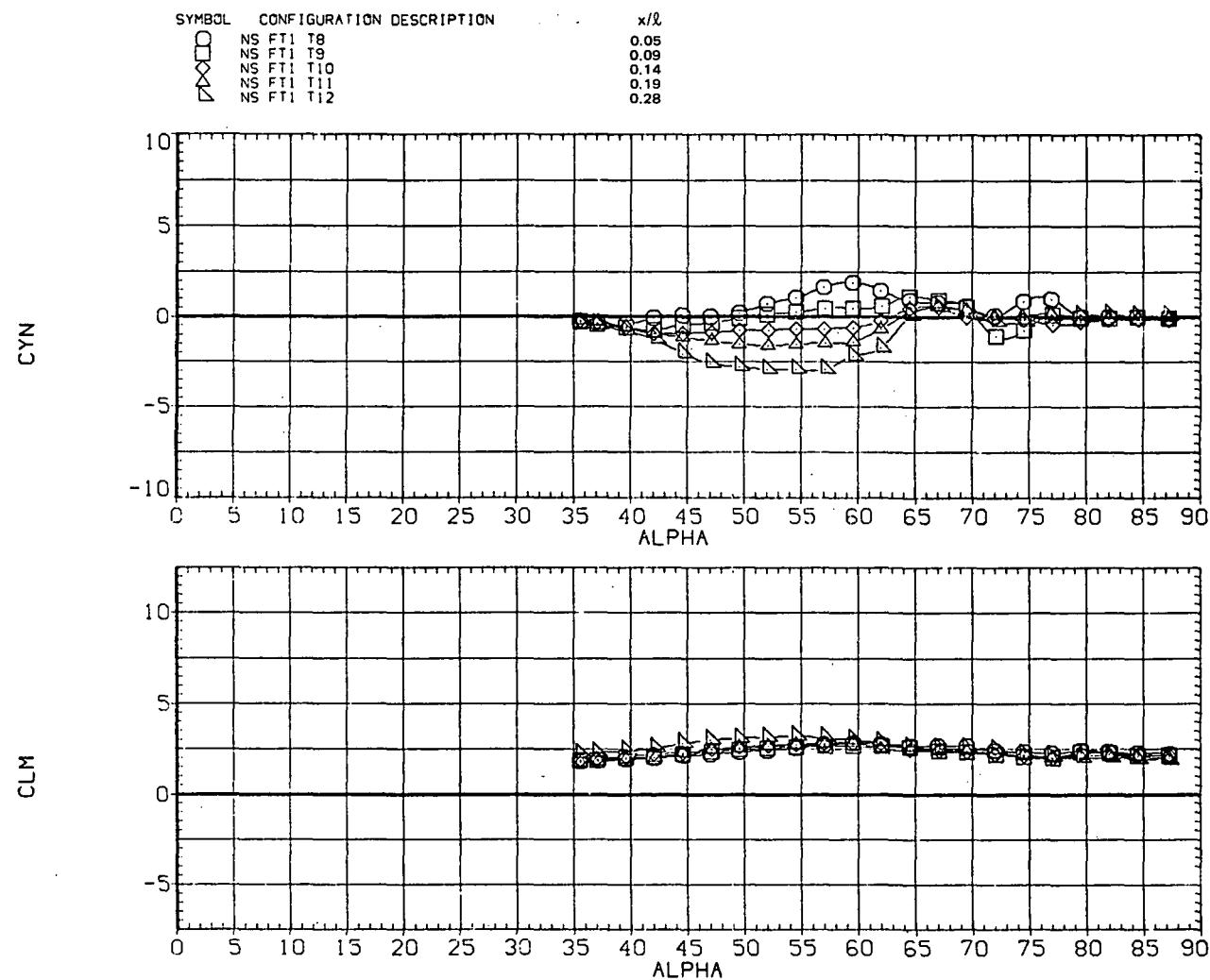
(c) C_n and C_m versus α.

Figure 13.— Concluded.

(a) C_Y versus α.
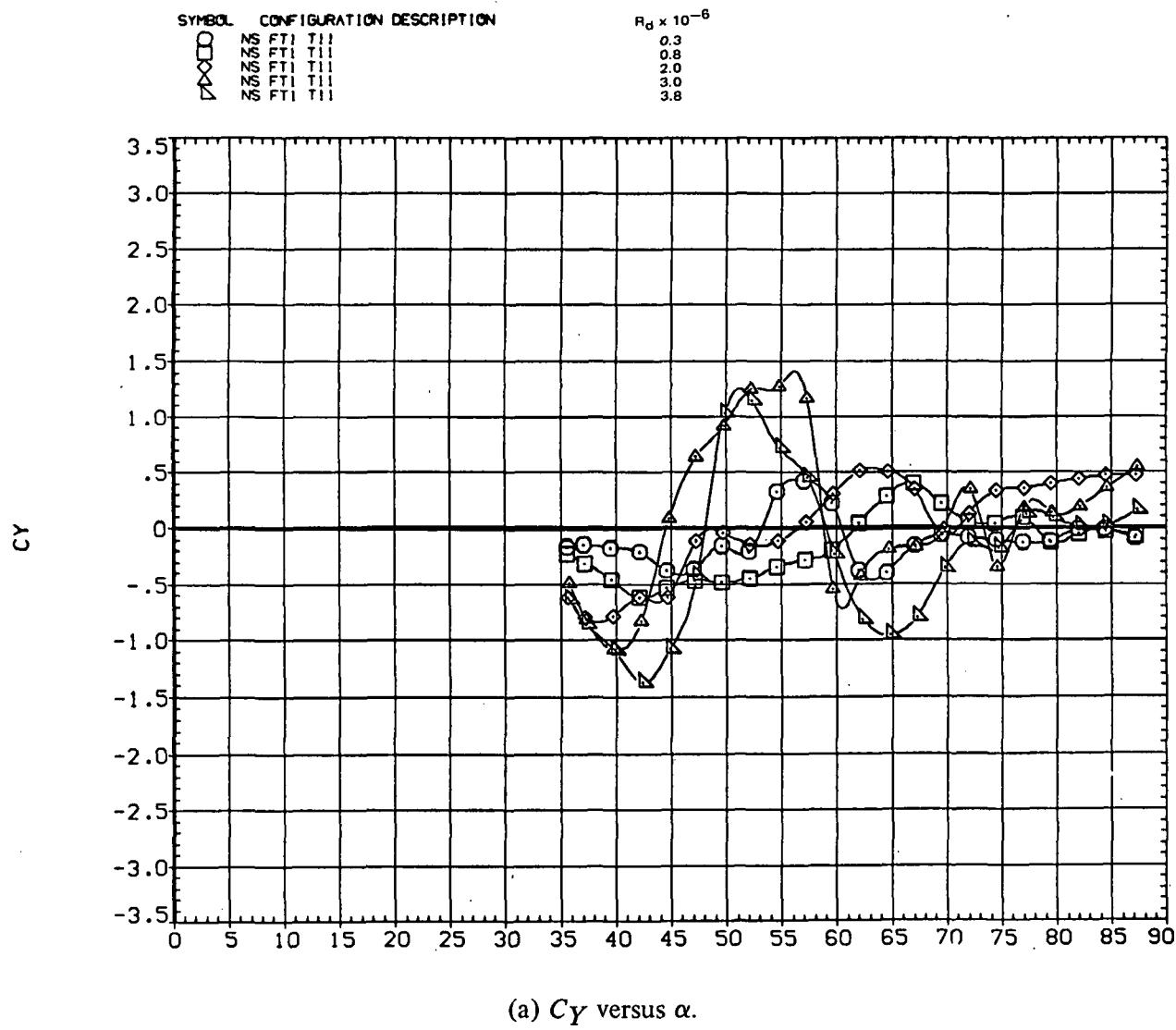
Figure 14.— Effect of Reynolds number with a boundary-layer transition-strip ring around the forebody at $x/\ell = 0.19$; $M = 0.25$, $R_d = 0.8 \times 10^6$.

SYMBOL	CONFIGURATION DESCRIPTION	$R_d \times 10^{-6}$
⊙	NS FT1 T11	0.3
⊟	NS FT1 T11	0.8
◇	NS FT1 T11	2.0
△	NS FT1 T11	3.0
△	NS FT1 T11	3.8
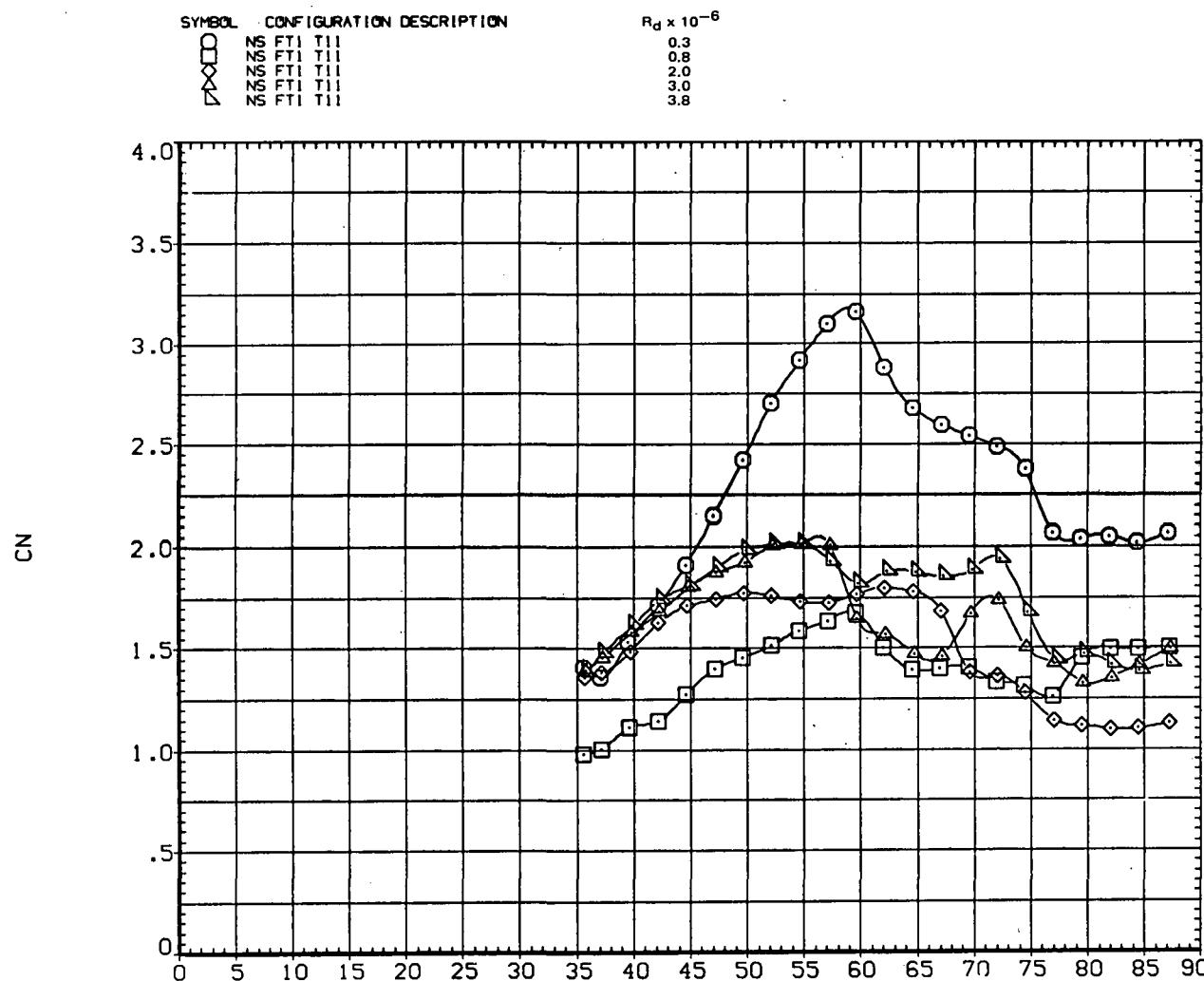
(b) C_N versus α.

Figure 14.– Continued.

(c) C_n and C_m versus α.

Figure 14.— Concluded.

SYMBOL   CONFIGURATION DESCRIPTION
          NS FT1 NO PAINT
          NS FT1 FLAT SPRAY-CAN PAINT
          NS FT1 POLISHED FLAT SPRAY-CAN PAINT
          NS FT1 POLISHED GLOSS SPRAY-CAN PAINT
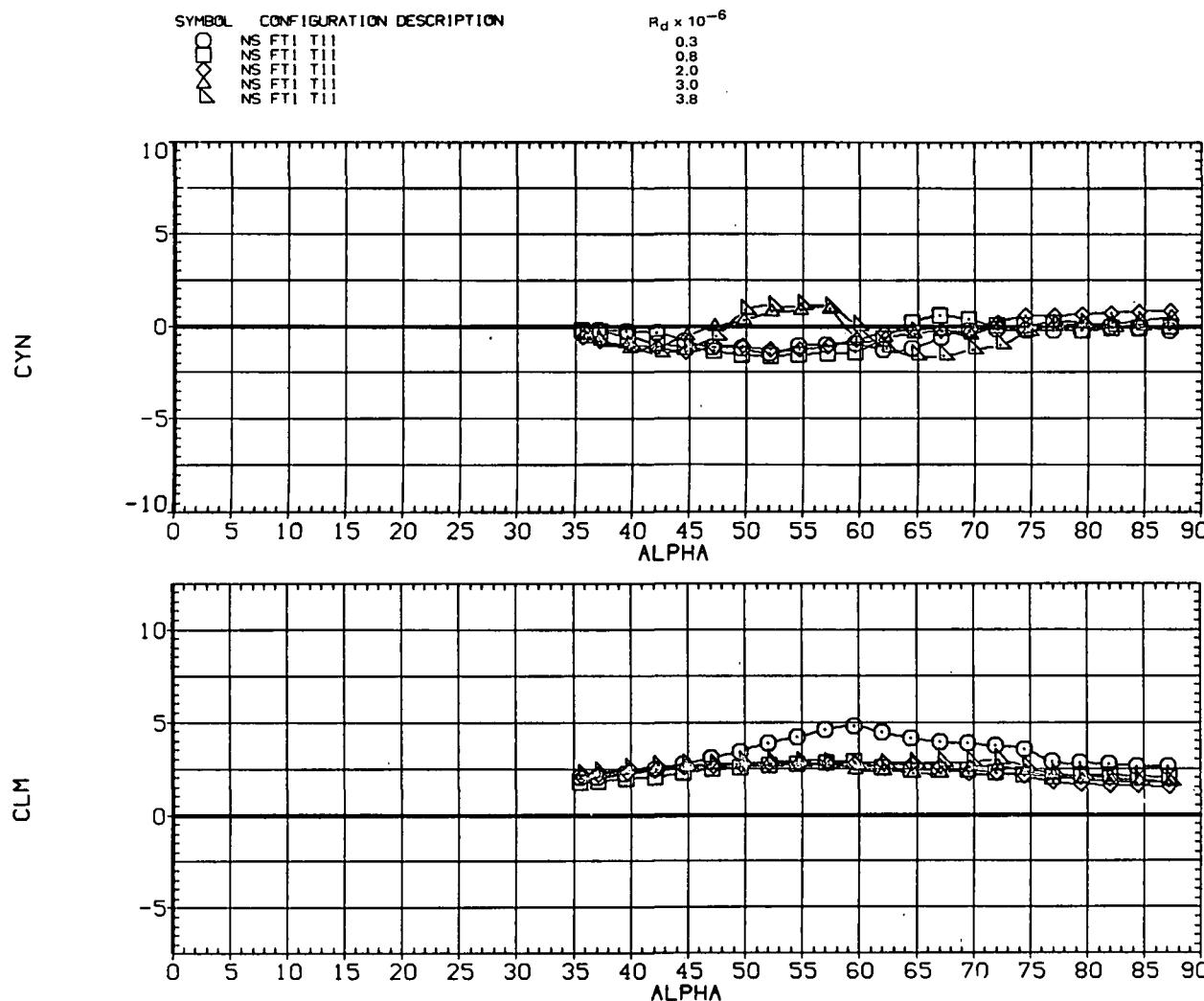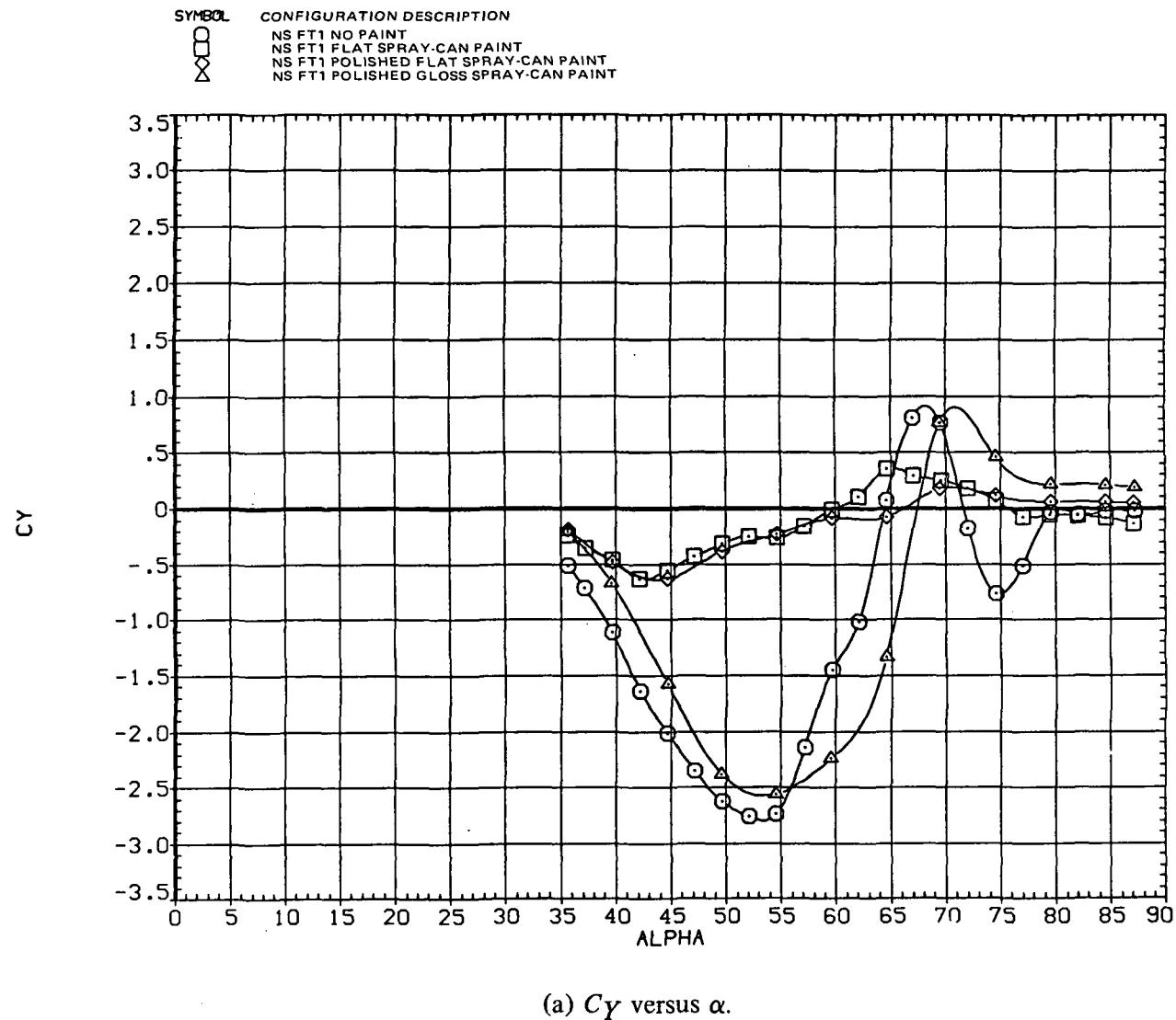
(a) C_Y versus α.

Figure 15.– Effect of surface roughness caused by flat-black point; $M = 0.25, R_d = 0.8 \times 10^6$

(b) C_N versus α.

Figure 15.– Continued.

SYMBOL   CONFIGURATION DESCRIPTION
NS FT1 NO PAINT
NS FT1 FLAT SPRAY CAN PAINT
NS FT1 POLISHED FLAT SPRAY-CAN PAINT
NS FT1 POLISHED GLOSS SPRAY-CAN PAINT
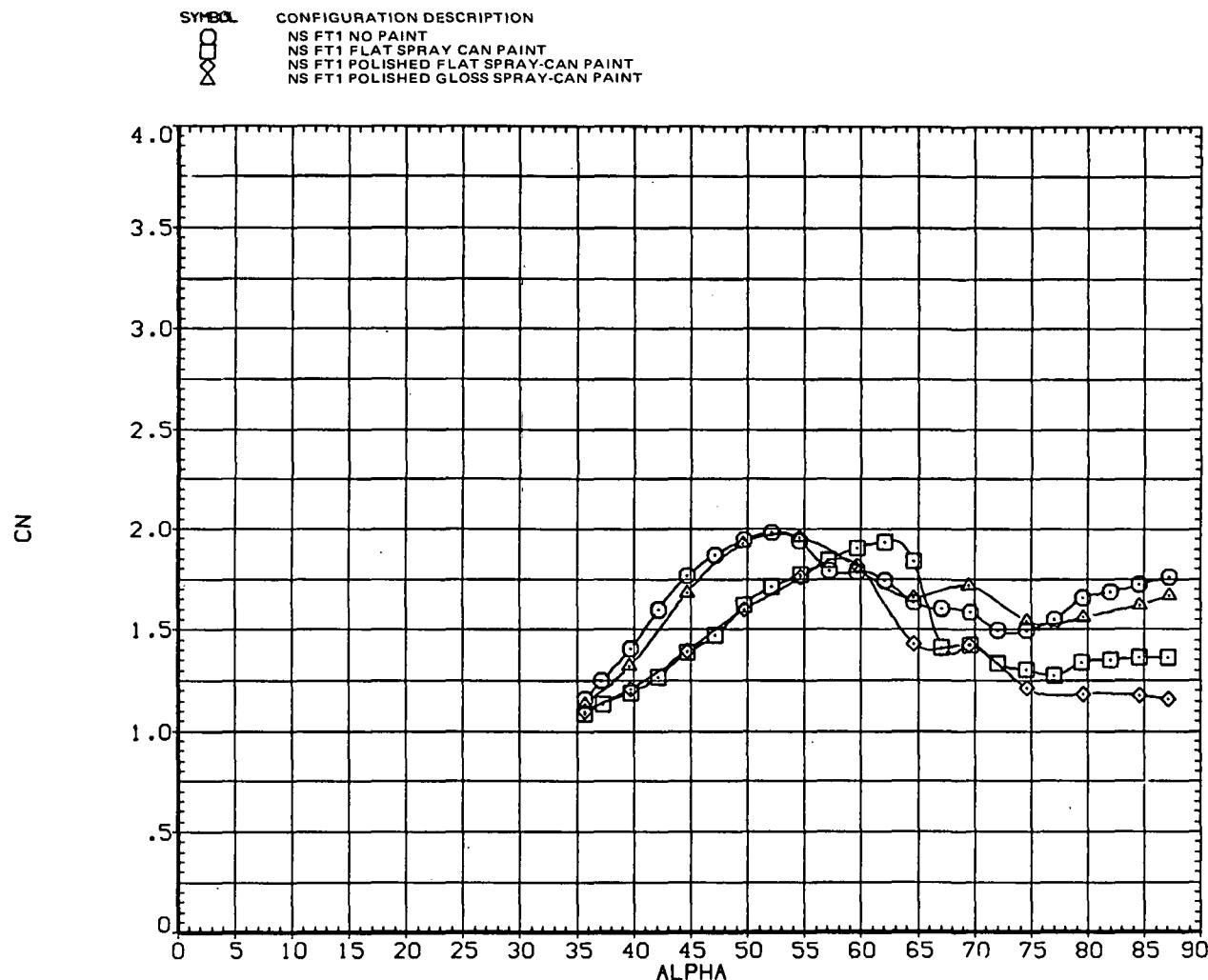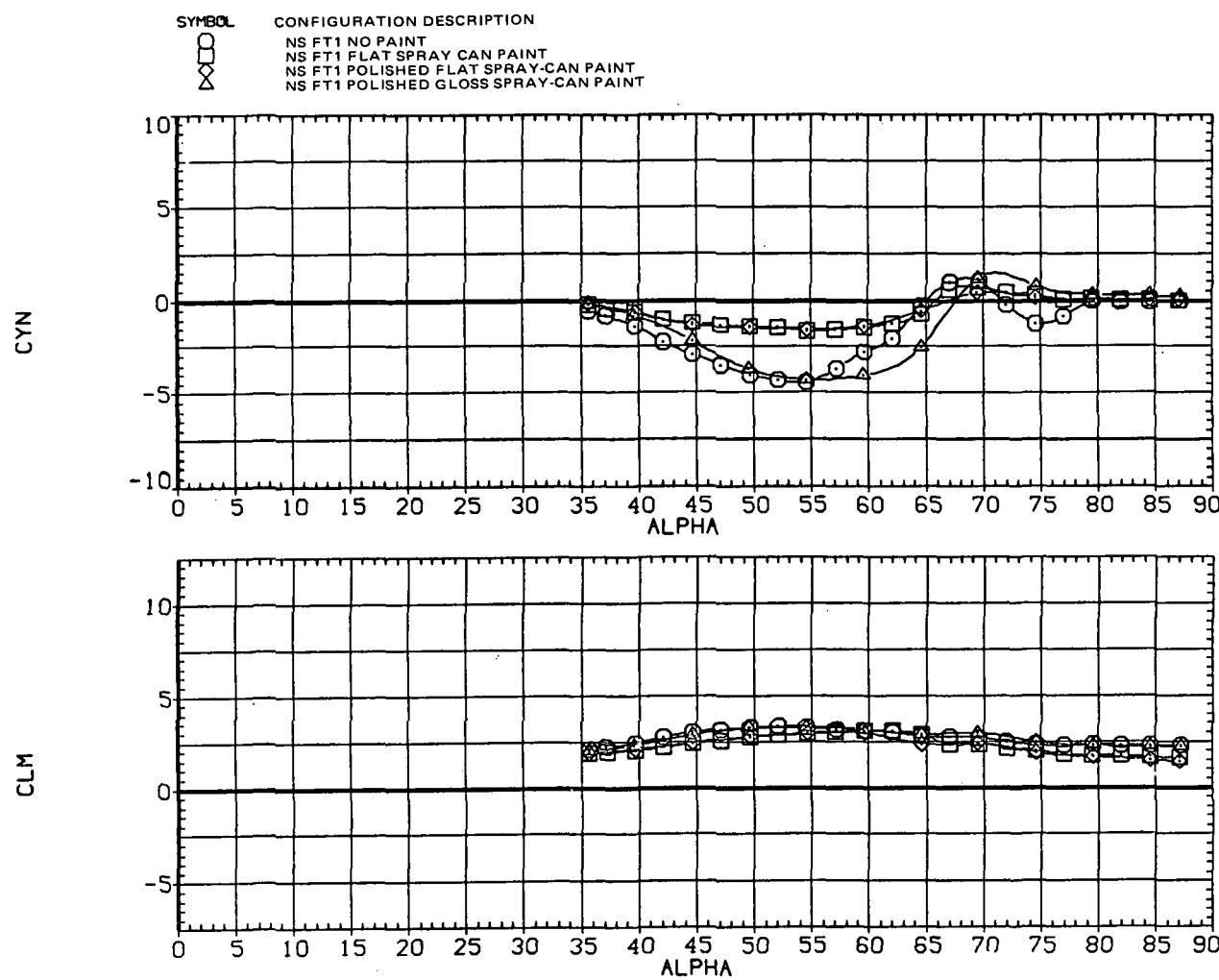
(c) C_n and C_m versus-α.

Figure 15.– Concluded.
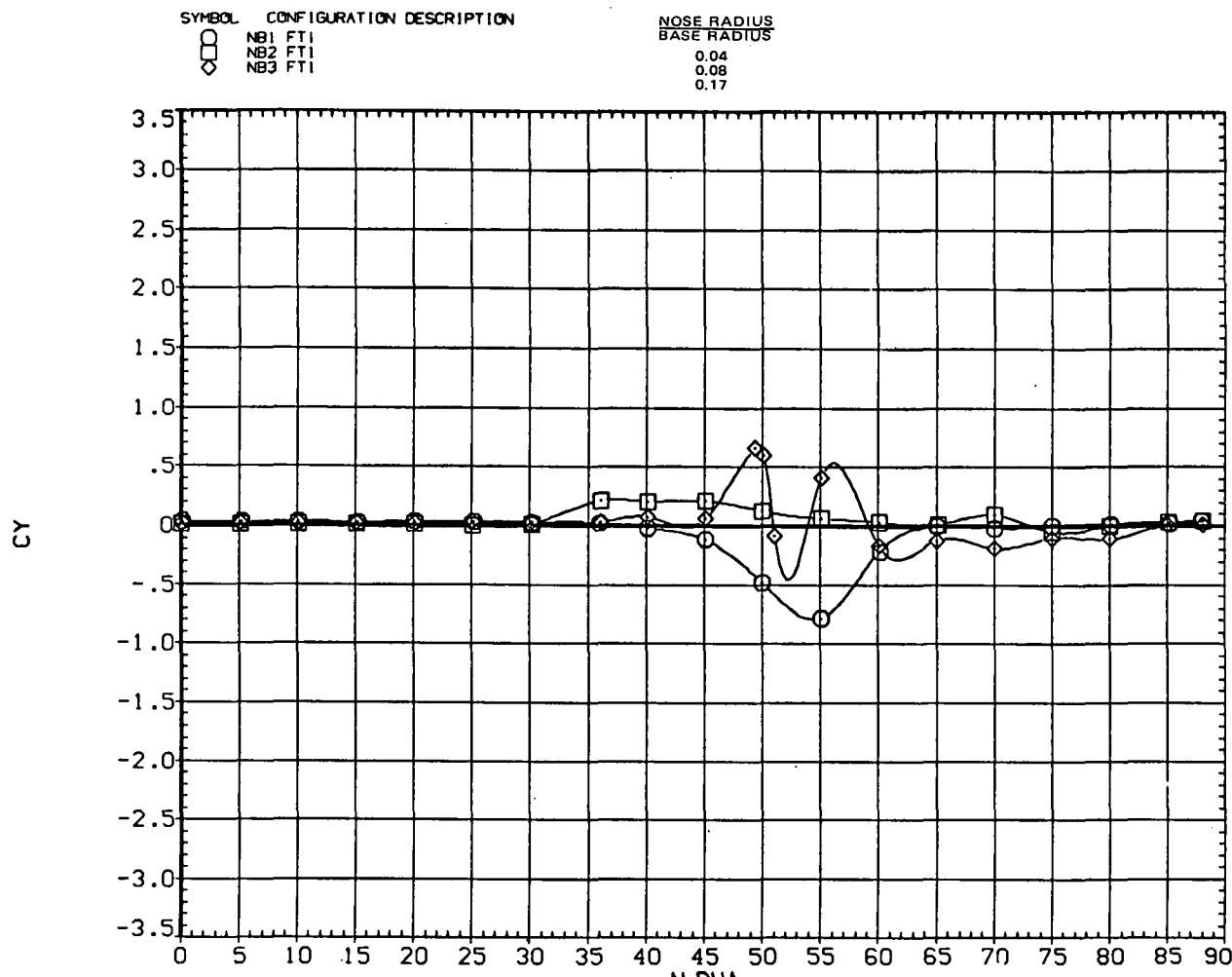
(a) C_Y versus α.

Figure 16.– Effect of nose radius; $M = 0.25, R_d = 0.8 \times 10^6$.
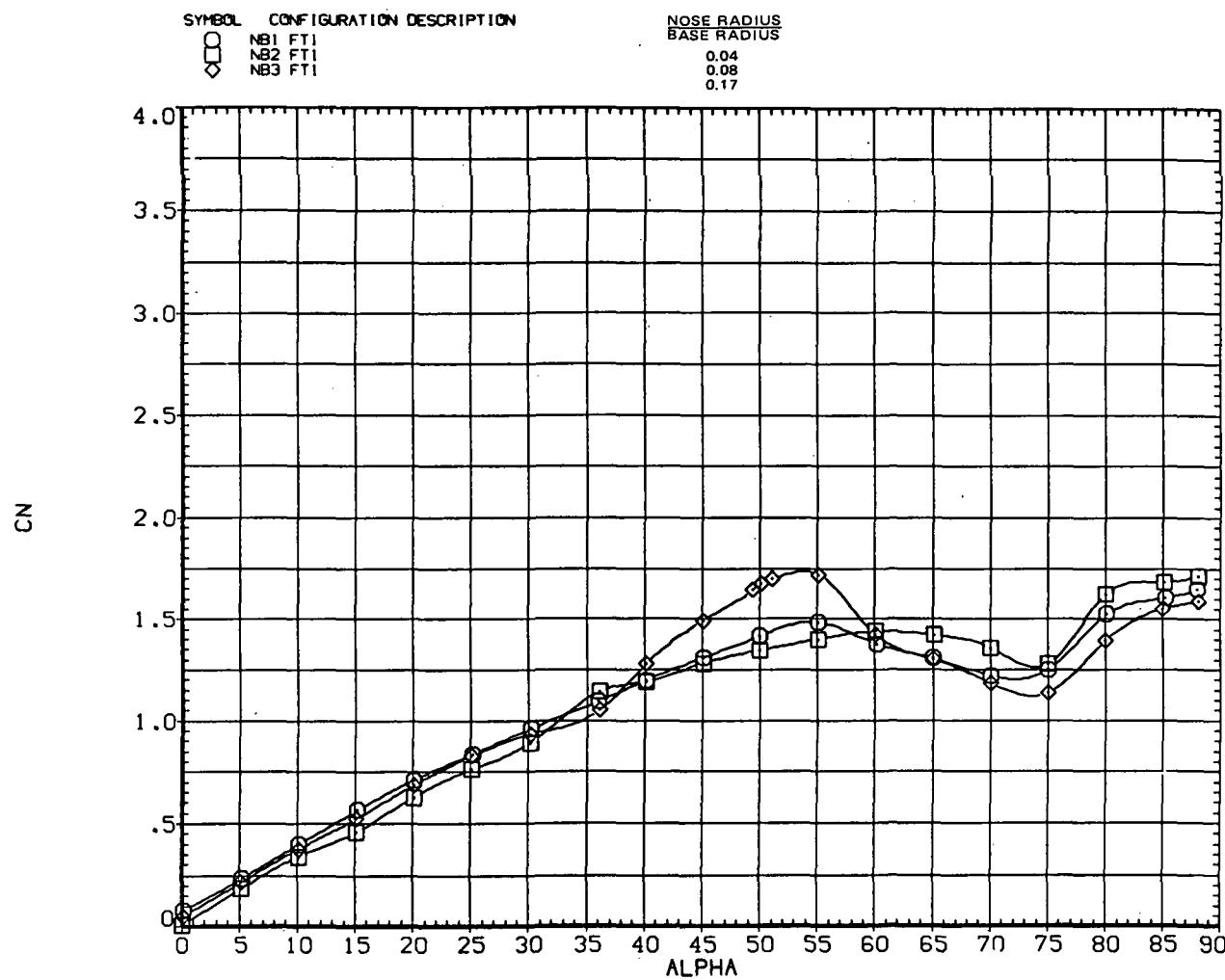
(b) C_N versus α.

Figure 16.— Continued.

CYN

ALPHA

CLM

ALPHA
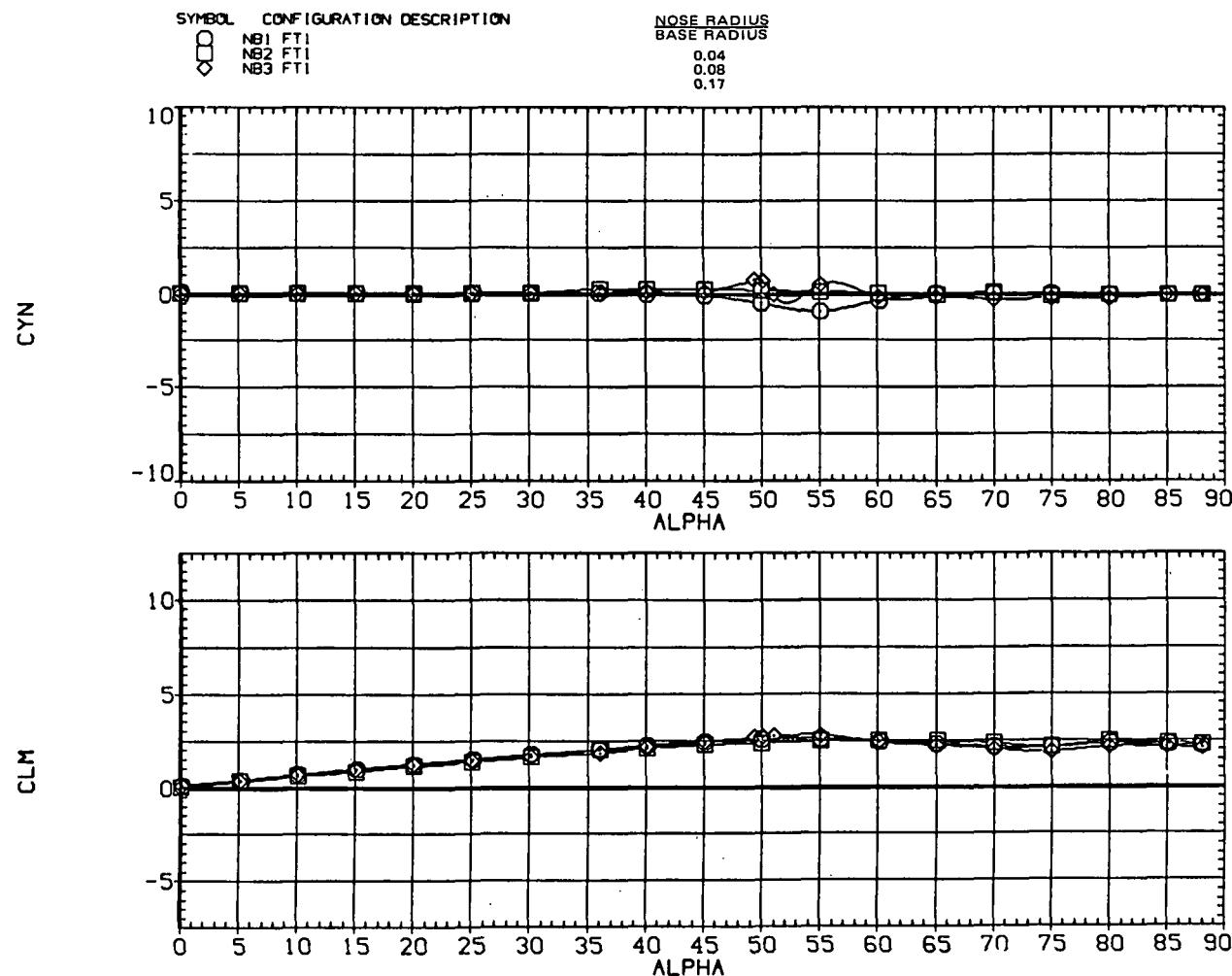
(c) C_n and C_m versus α.

Figure 16.– Concluded.
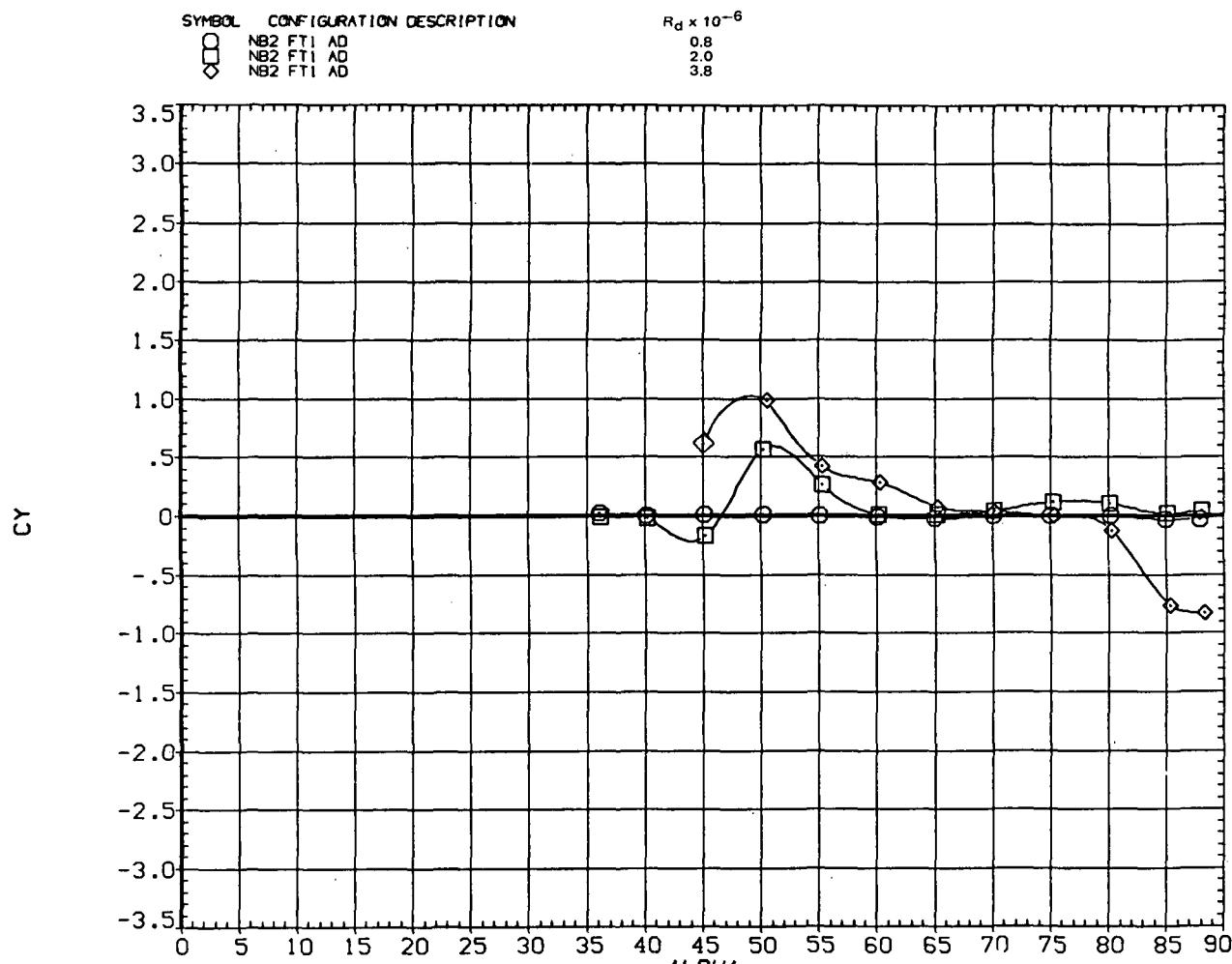
(a) C_Y versus α.

Figure 17.– Effect of Reynolds number with nose bluntness; $M = 0.25$, $R_d = 0.8 \times 10^6$, (nose radius/base radius) = 0.08.
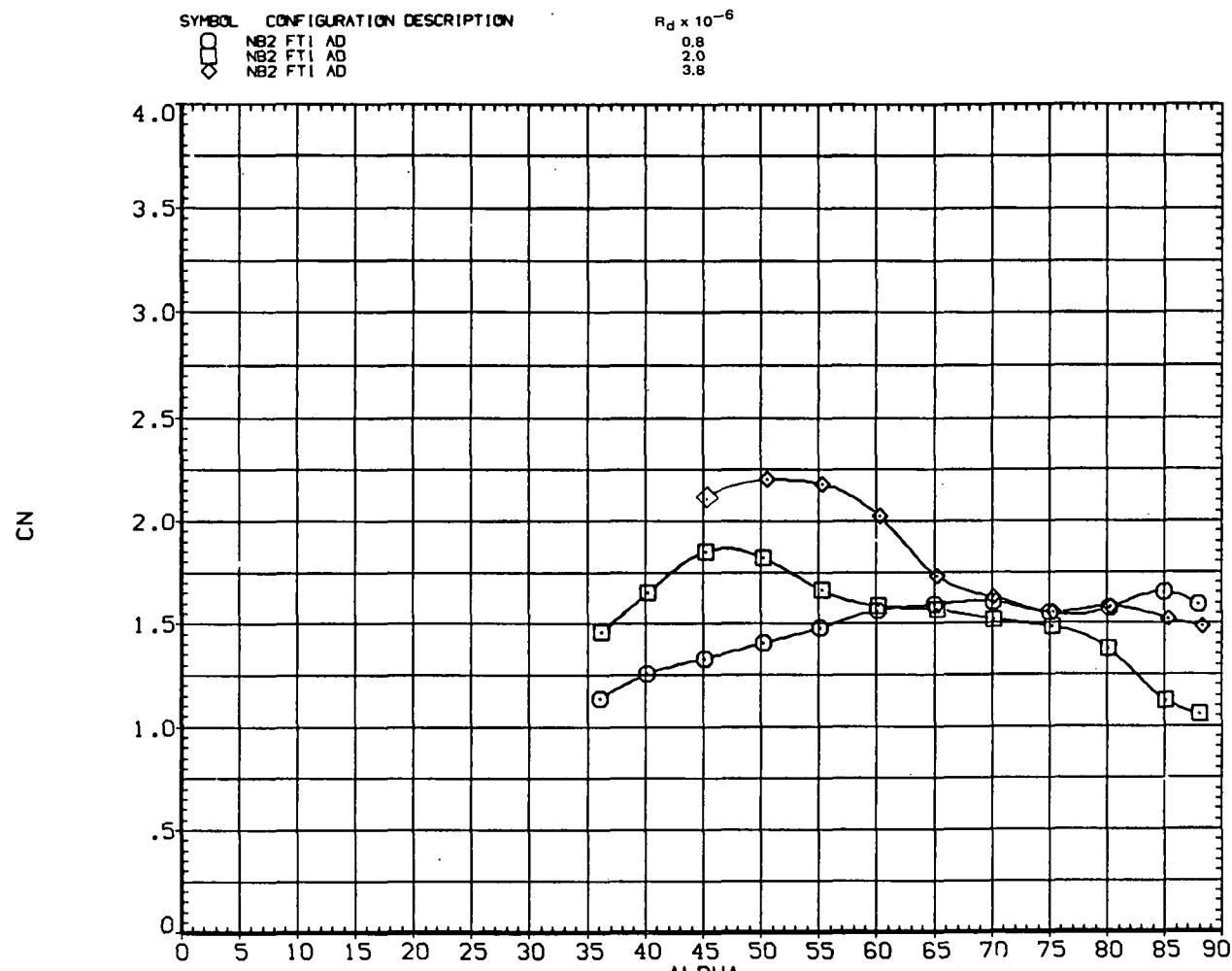
(b) C_N versus α.

Figure 17.– Continued.
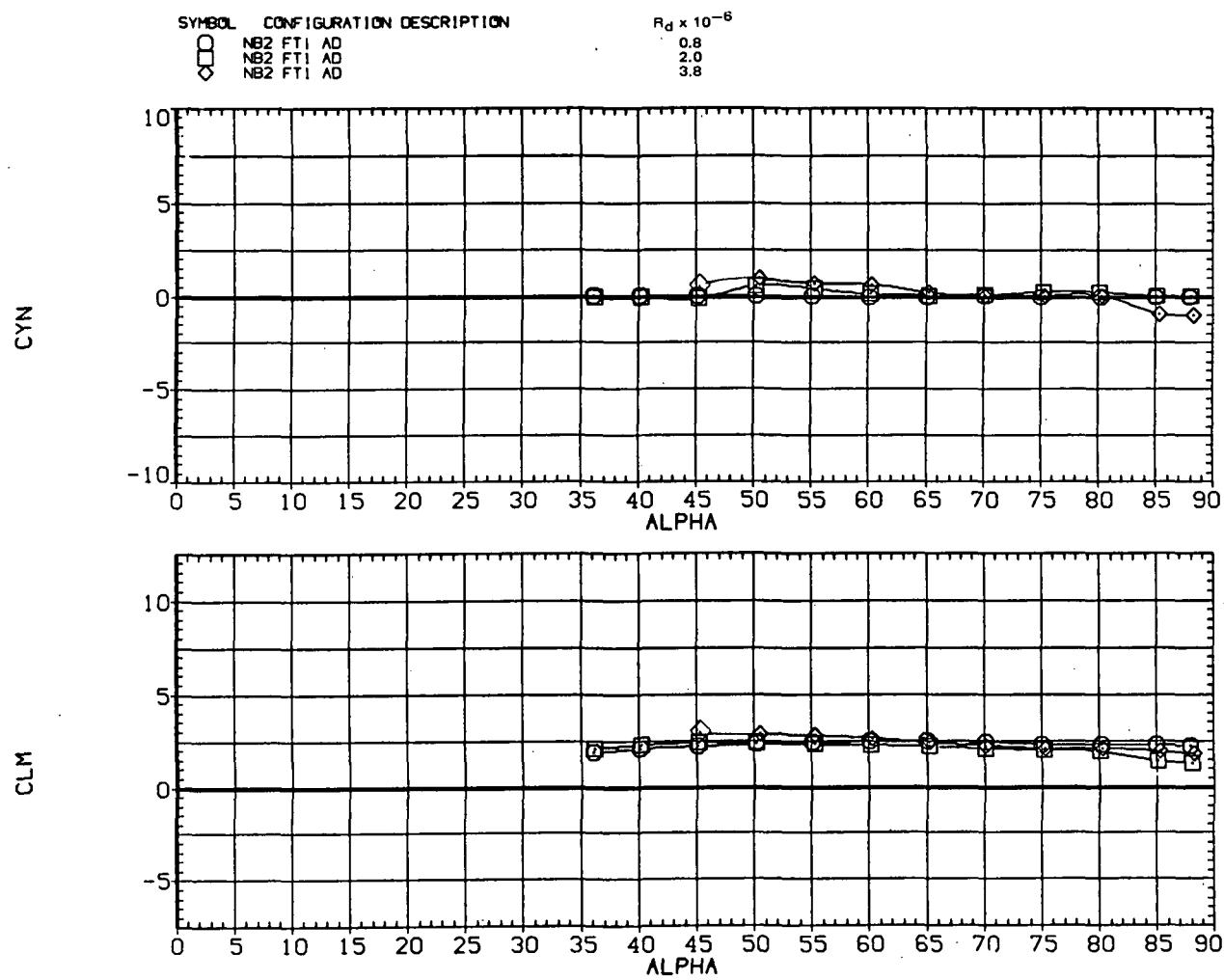
(c) C_n and C_m versus α.

Figure 17.– Concluded.
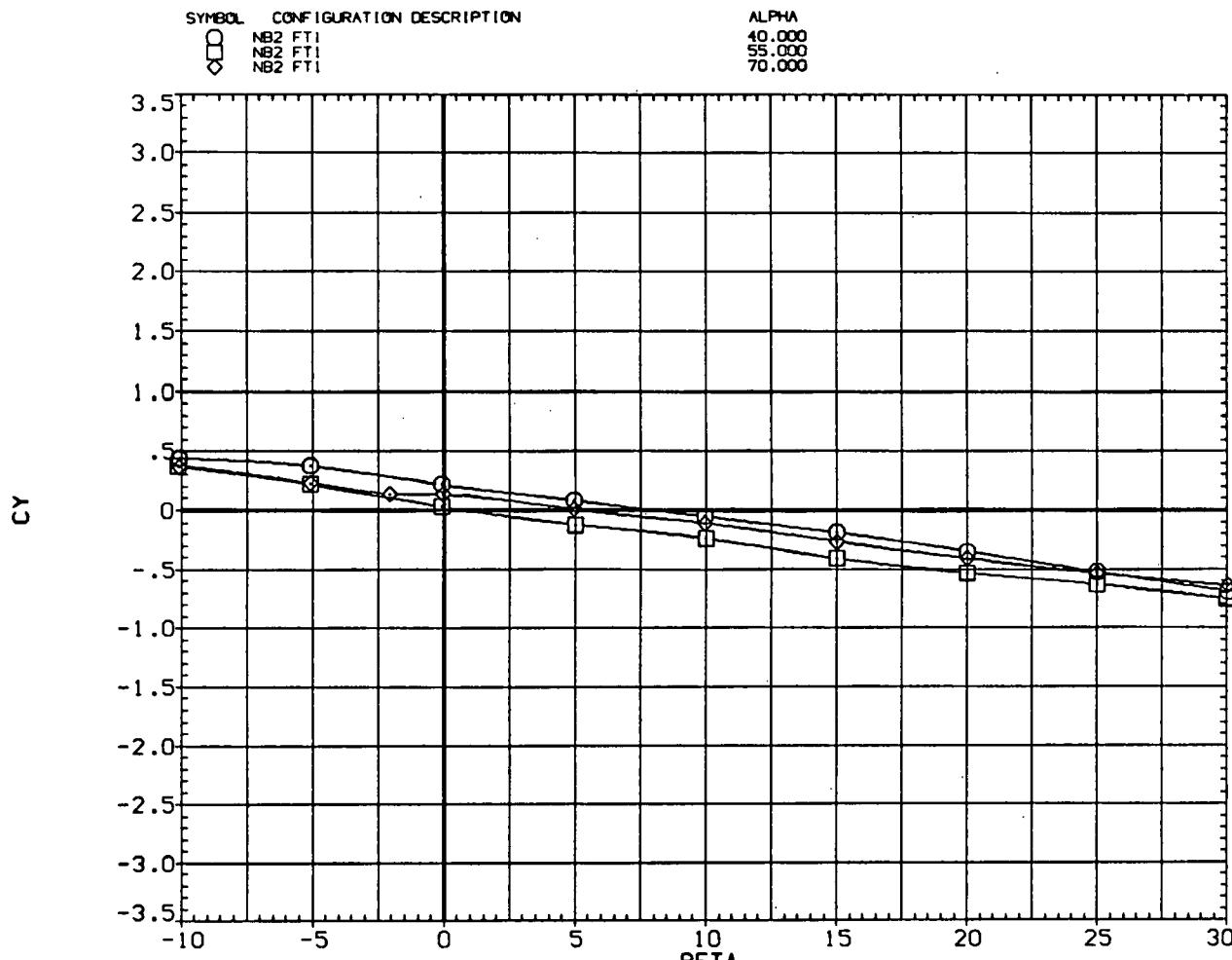
(a) C_Y versus α.

Figure 18.— Effect of sideslip with nose bluntness; $M = 0.25$, $R_d = 0.8 \times 10^6$, (nose radius/base radius) = 0.08.
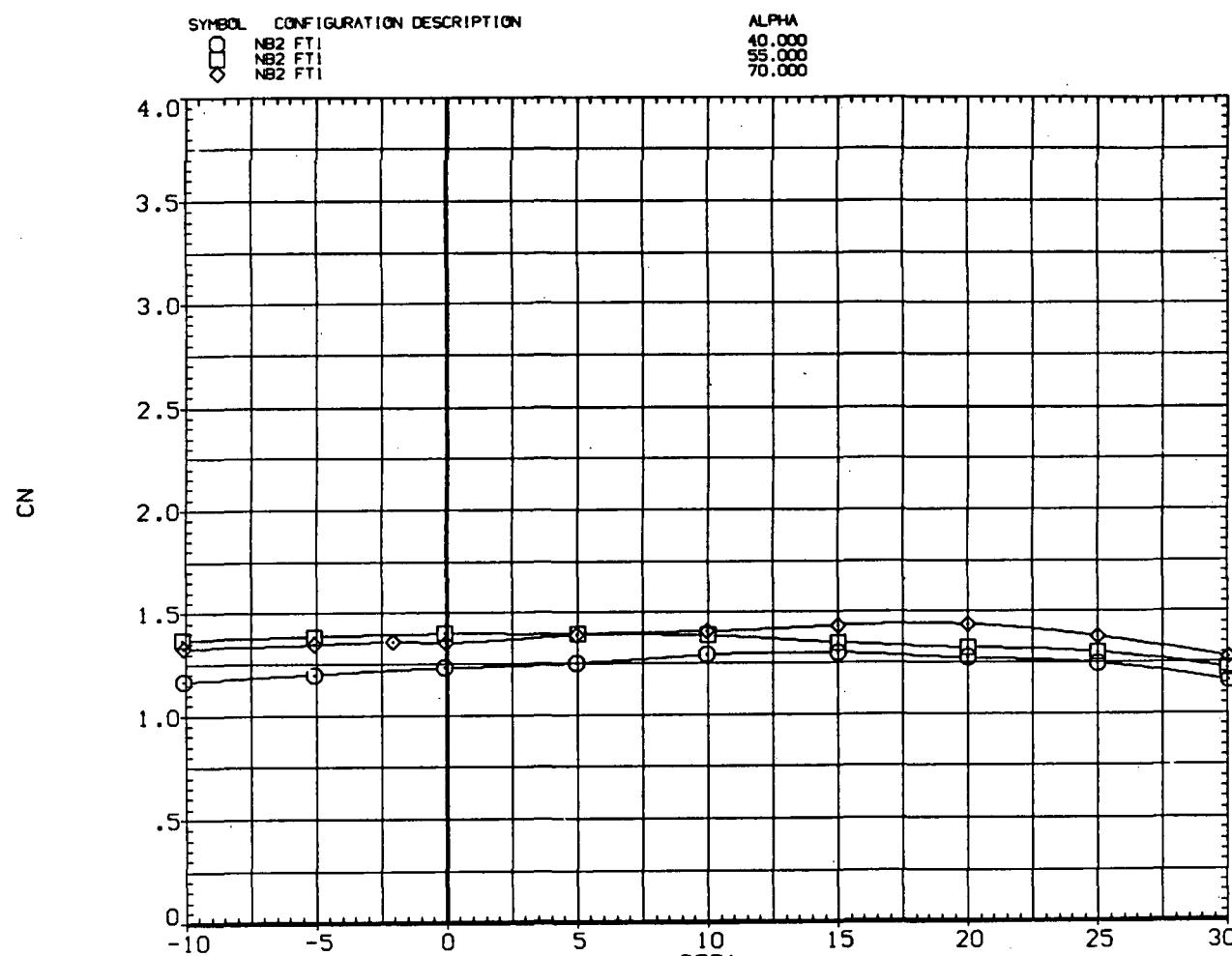
(b) C_N versus α.

Figure 18.— Continued.

(c) C_n and C_m versus α.

Figure 18.– Concluded.

SYMBOL   CONFIGURATION DESCRIPTION   EXPOSED
                                            WIDTH, cm
          NST1 FT1 AD   0.32
          NST2 FT1 AD   0.64
          NST3 FT1 AD   1.27
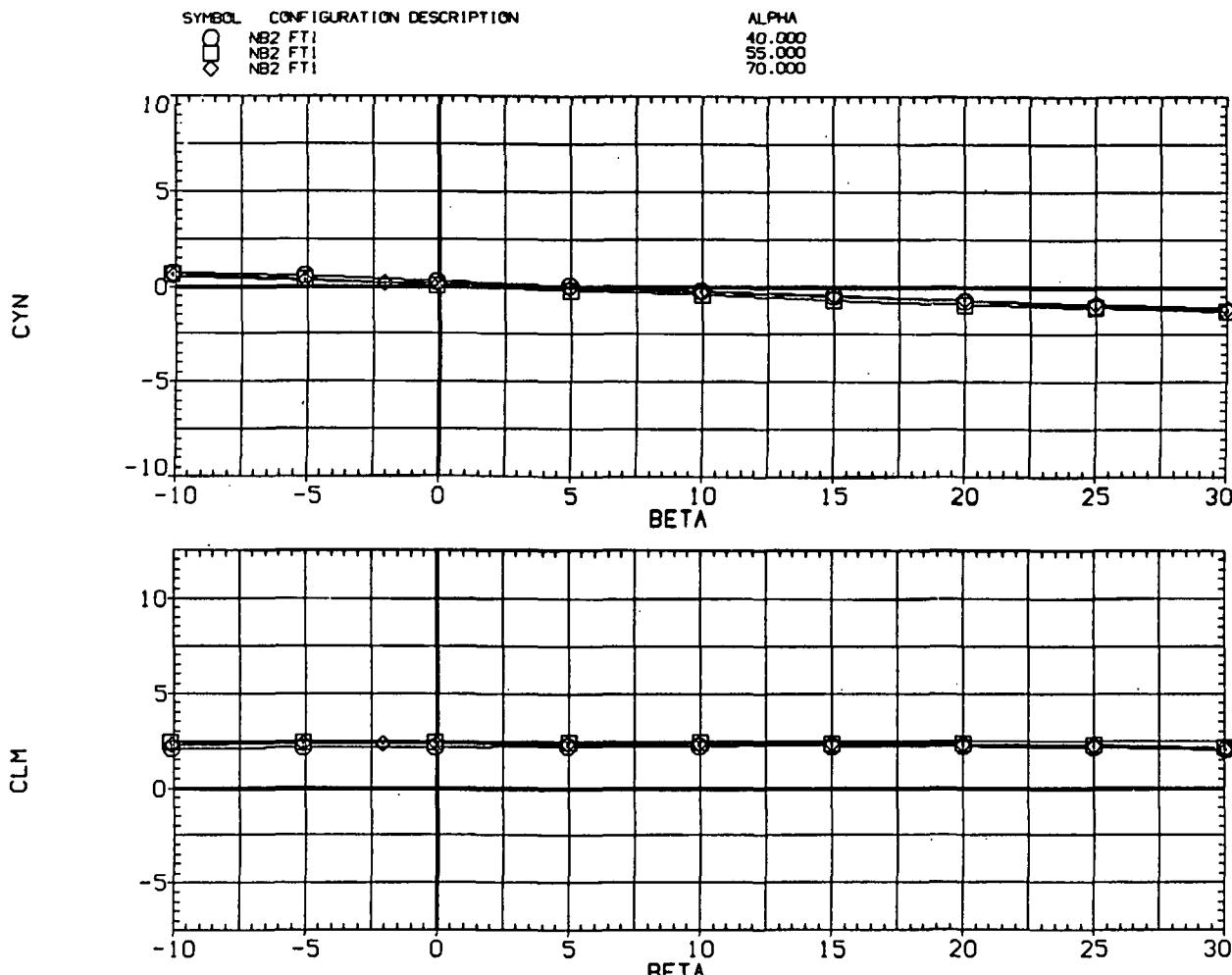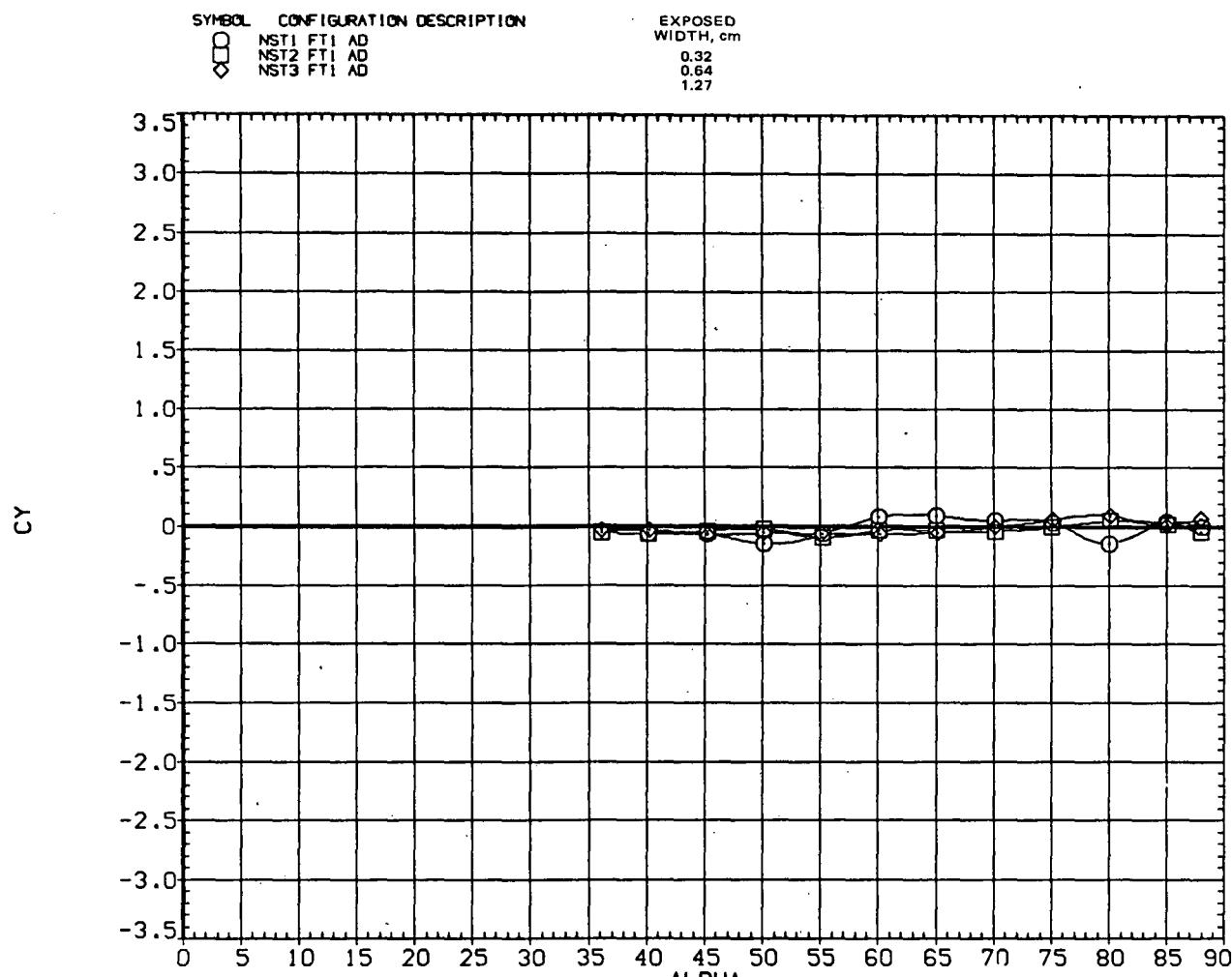
(a) C_Y versus α.

Figure 19.– Effect of nose strakes having various widths; $M = 0.25$, $R_d = 0.8 \times 10^6$.

(b) C_N versus α.

Figure 19.– Continued.

SYMBOL   CONFIGURATION DESCRIPTION   EXPOSED
                                            WIDTH, cm
○   NST1 FT1 AD   0.32
⬡   NST2 FT1 AD   0.64
◇   NST3 FT1 AD   1.27

(c) C_n and C_m versus α.

Figure 19.– Concluded.

SYMBOL	CONFIGURATION DESCRIPTION	$R_d \times 10^{-6}$
□	NST1 FT1 AD	0.3
○	NST1 FT1 AD	0.8
⊗	NST1 FT1 AD	2.0
△	NST1 FT1 AD	3.0
◁	NST1 FT1 AD	3.8
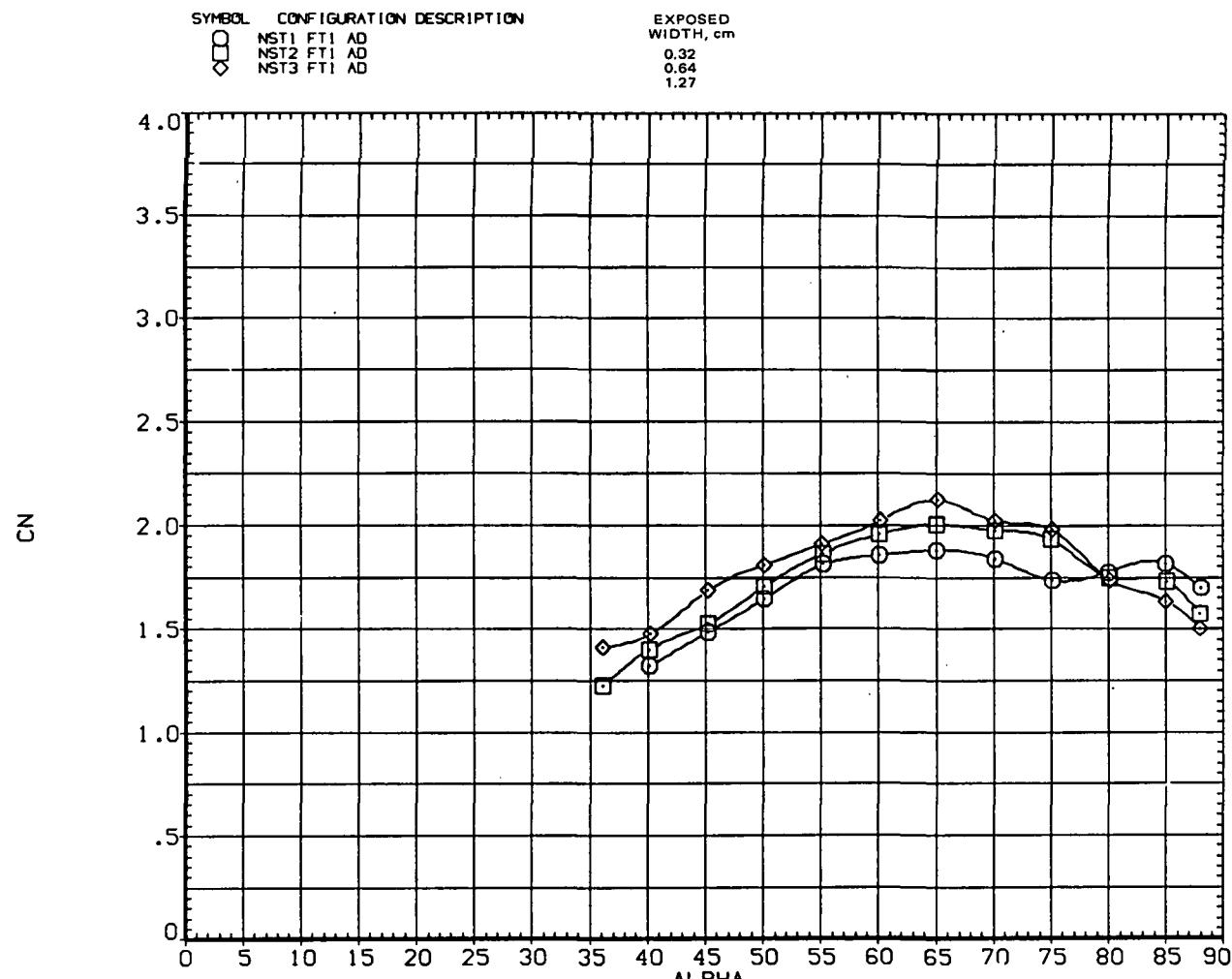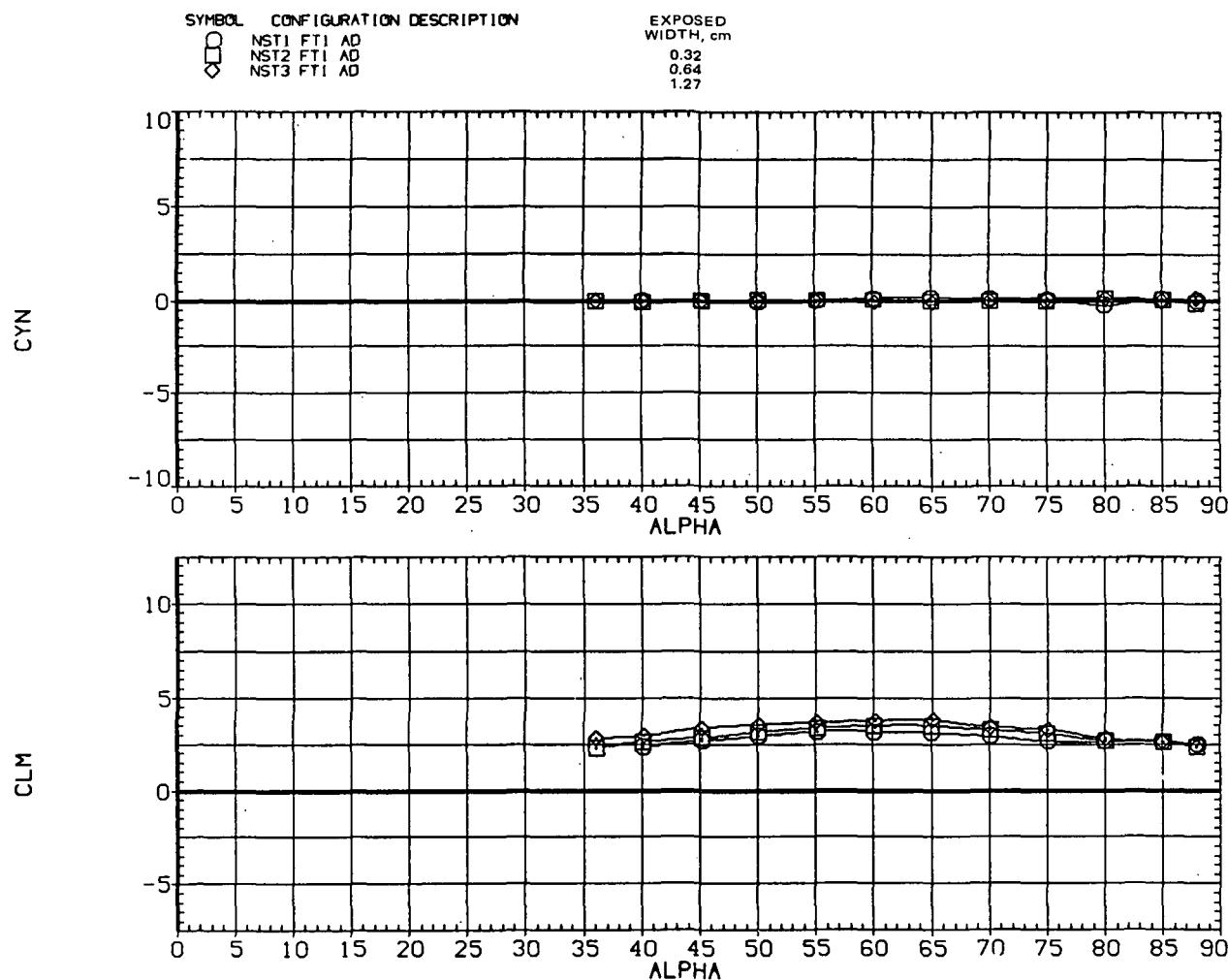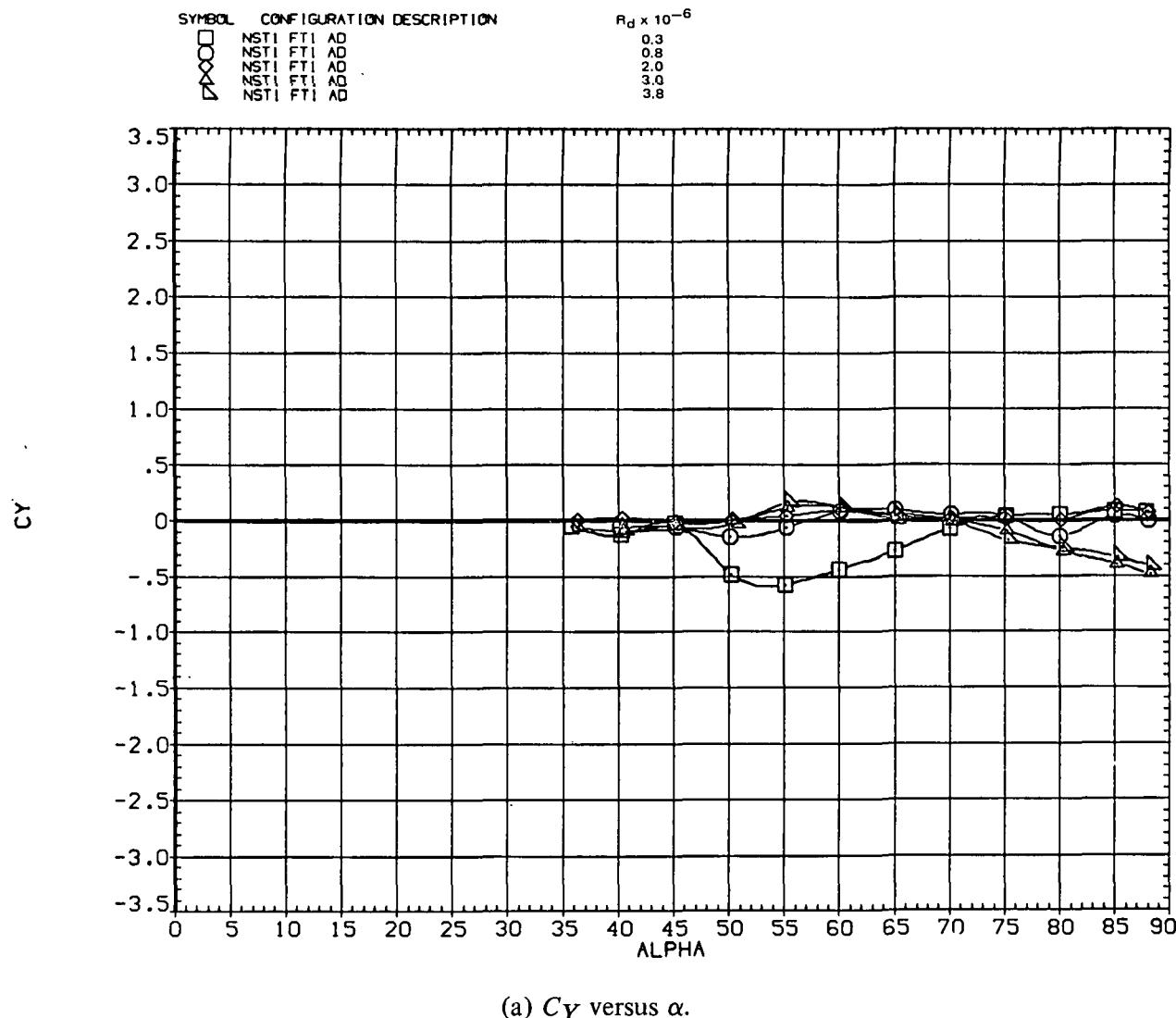
(a) C_Y versus α.

Figure 20.— Effect of Reynolds number with nose strakes; $M = 0.25$, exposed width = 0.32 cm.
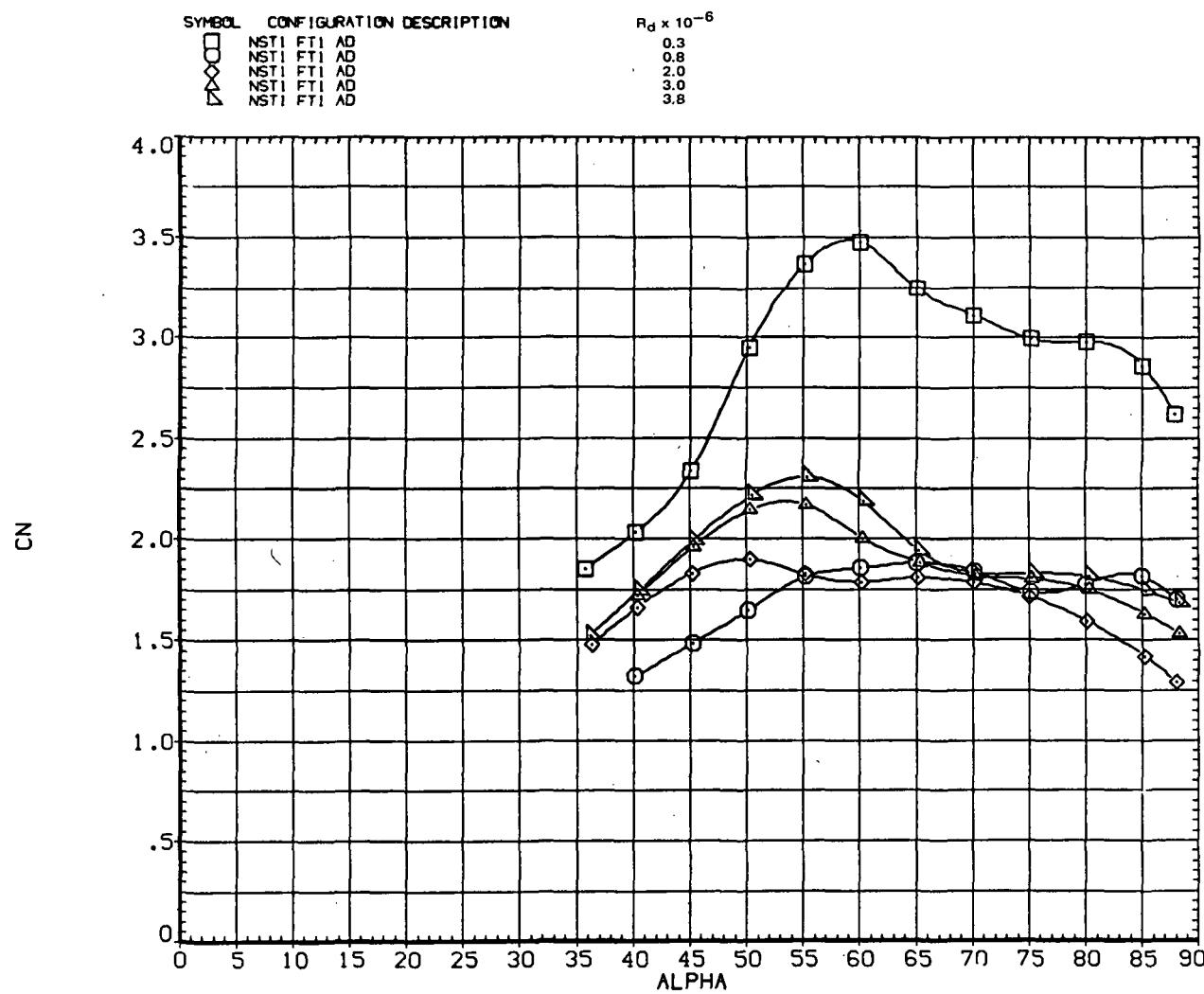
(b) C_N versus α.

Figure 20.– Continued.
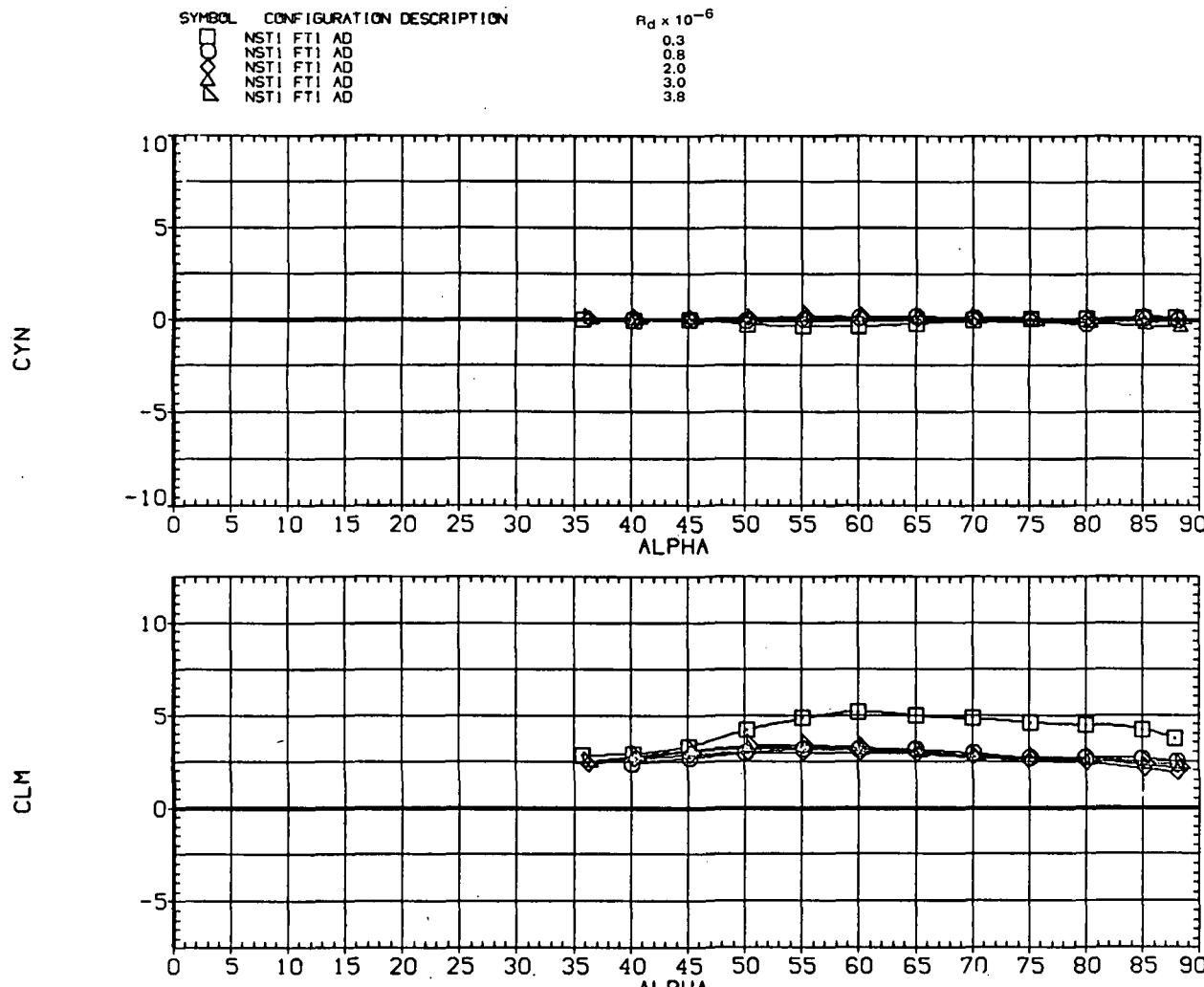
(c) C_n and C_m versus α.

Figure 20.– Concluded.
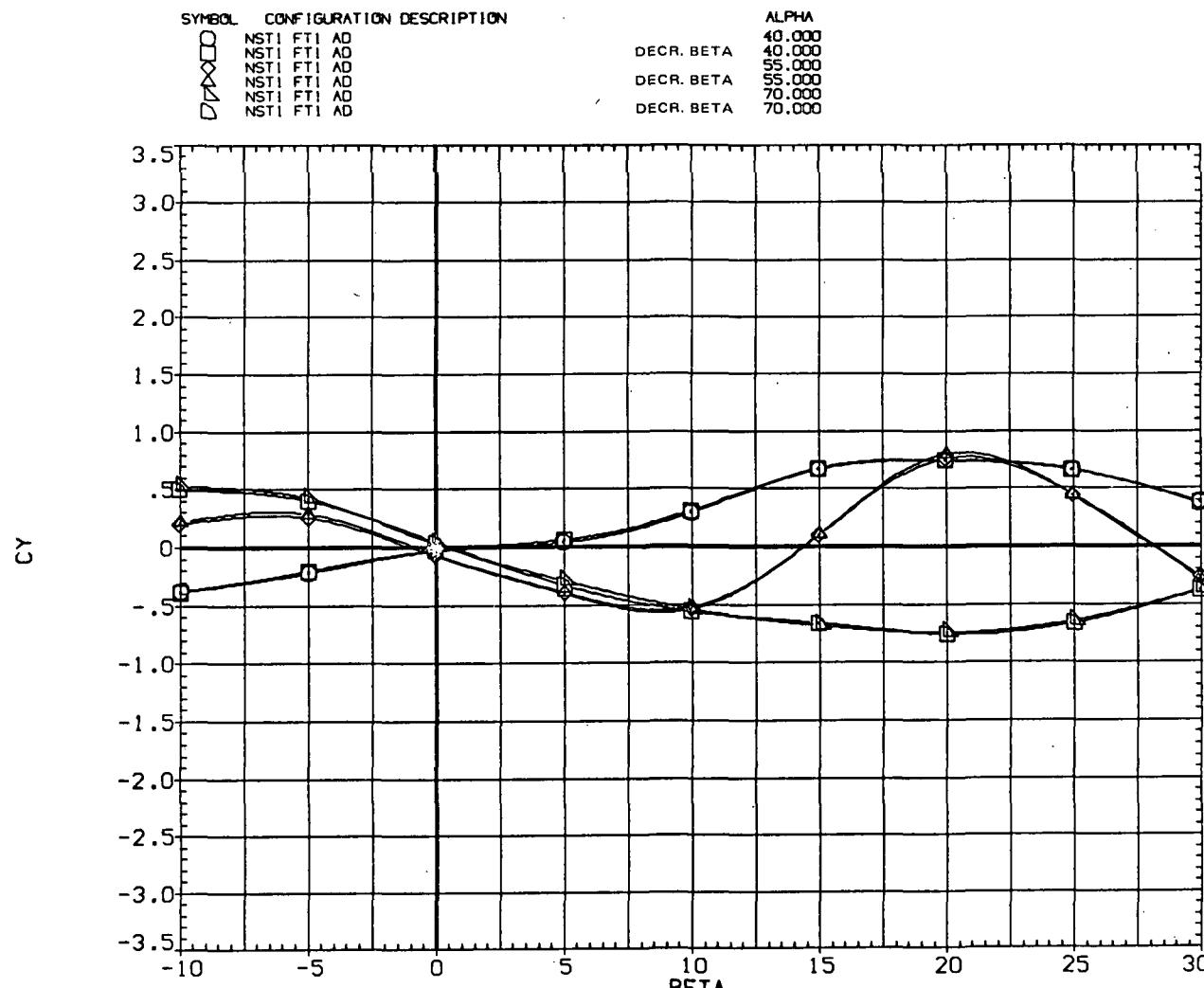
(a) C_Y versus α.

Figure 21.— Effect of sideslip with nose strakes; $M = 0.25$, $R_d = 0.8 \times 10^6$, exposed width = 0.32 cm.

SYMBOL	CONFIGURATION DESCRIPTION		ALPHA
	NST1 FT1 AD		40.000
	NST1 FT1 AD	DECR. BETA	40.000
	NST1 FT1 AD		55.000
	NST1 FT1 AD	DECR. BETA	55.000
	NST1 FT1 AD		70.000
	NST1 FT1 AD	DECR. BETA	70.000
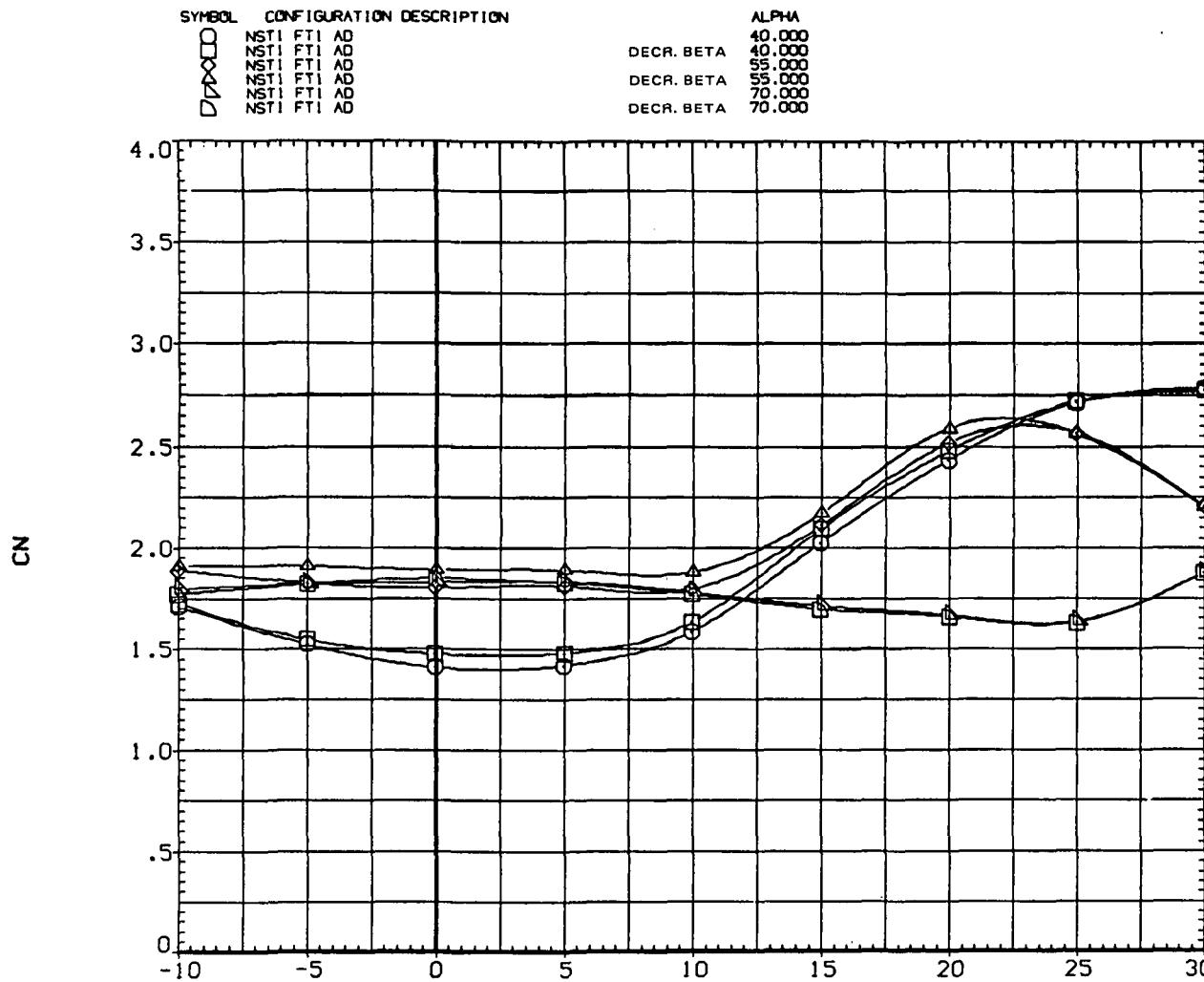
(b) C_N versus α.

Figure 21.– Continued.

(c) C_n and C_m versus α.

Figure 21.– Concluded.

SYMBOL	CONFIGURATION DESCRIPTION	PHI-N	PHI-B
○	NST1 FT1	.000	.000
□	NST1 FT1	15.000	.000
◇	NST1 FT1	30.000	.000
△	NST1 FT1	45.000	.000
◁	NST1 FT1	60.000	.000
◻	NST1 FT1	90.000	.000
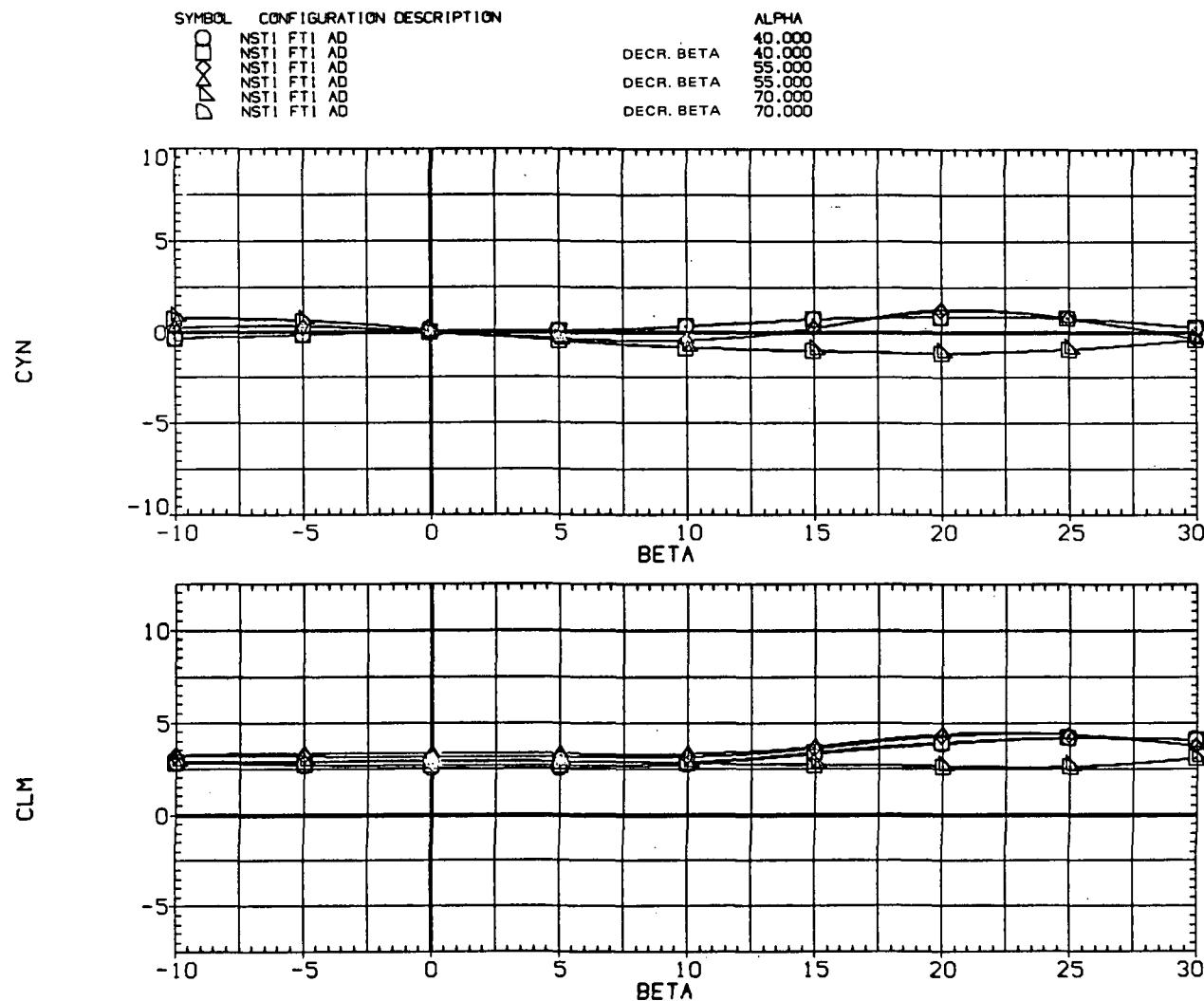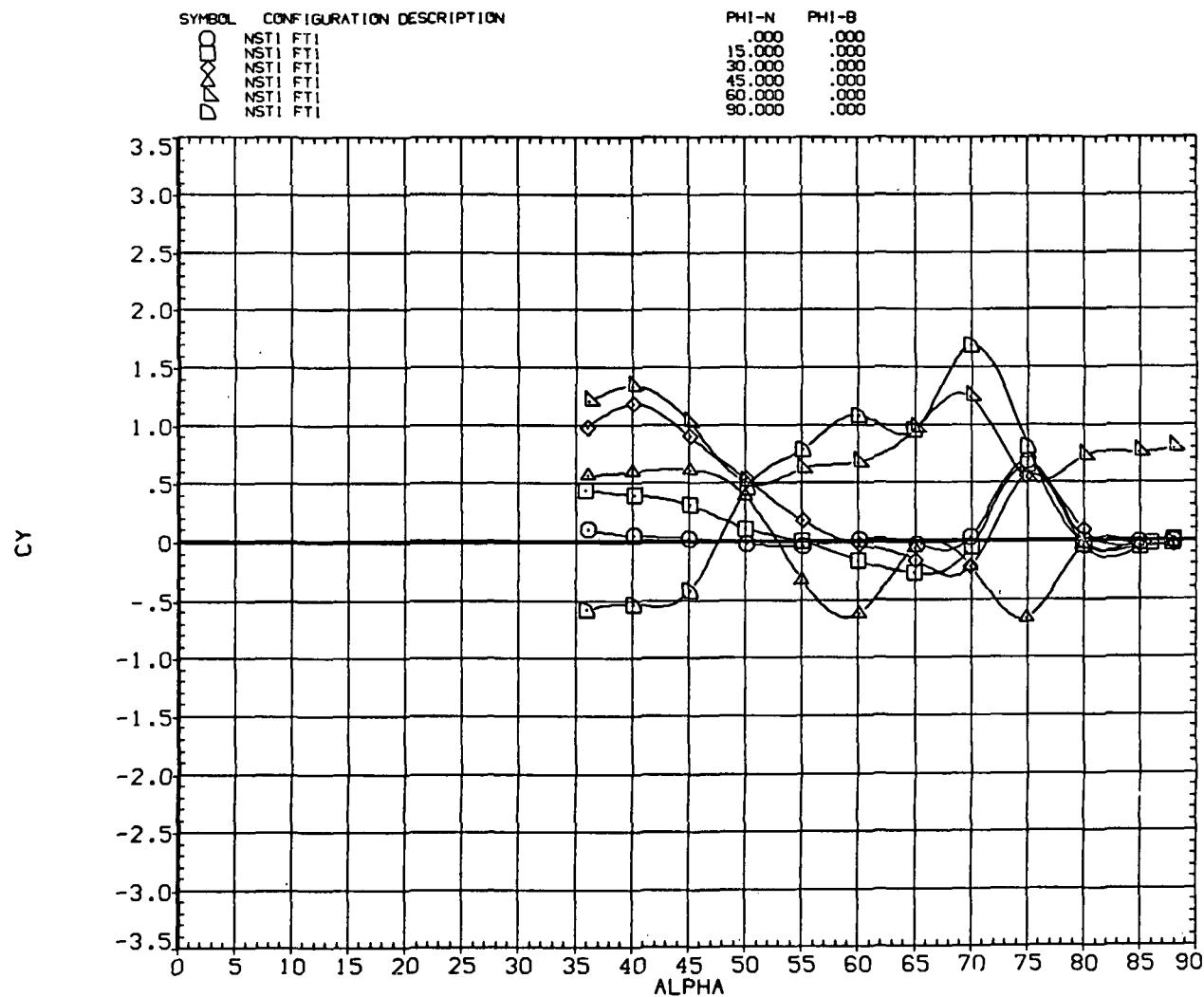
(a) C_Y versus α.

Figure 22.— Effect of roll angle of nose section with strakes; $M = 0.25$, $R_d = 0.8 \times 10^6$, exposed width = 0.32 cm.
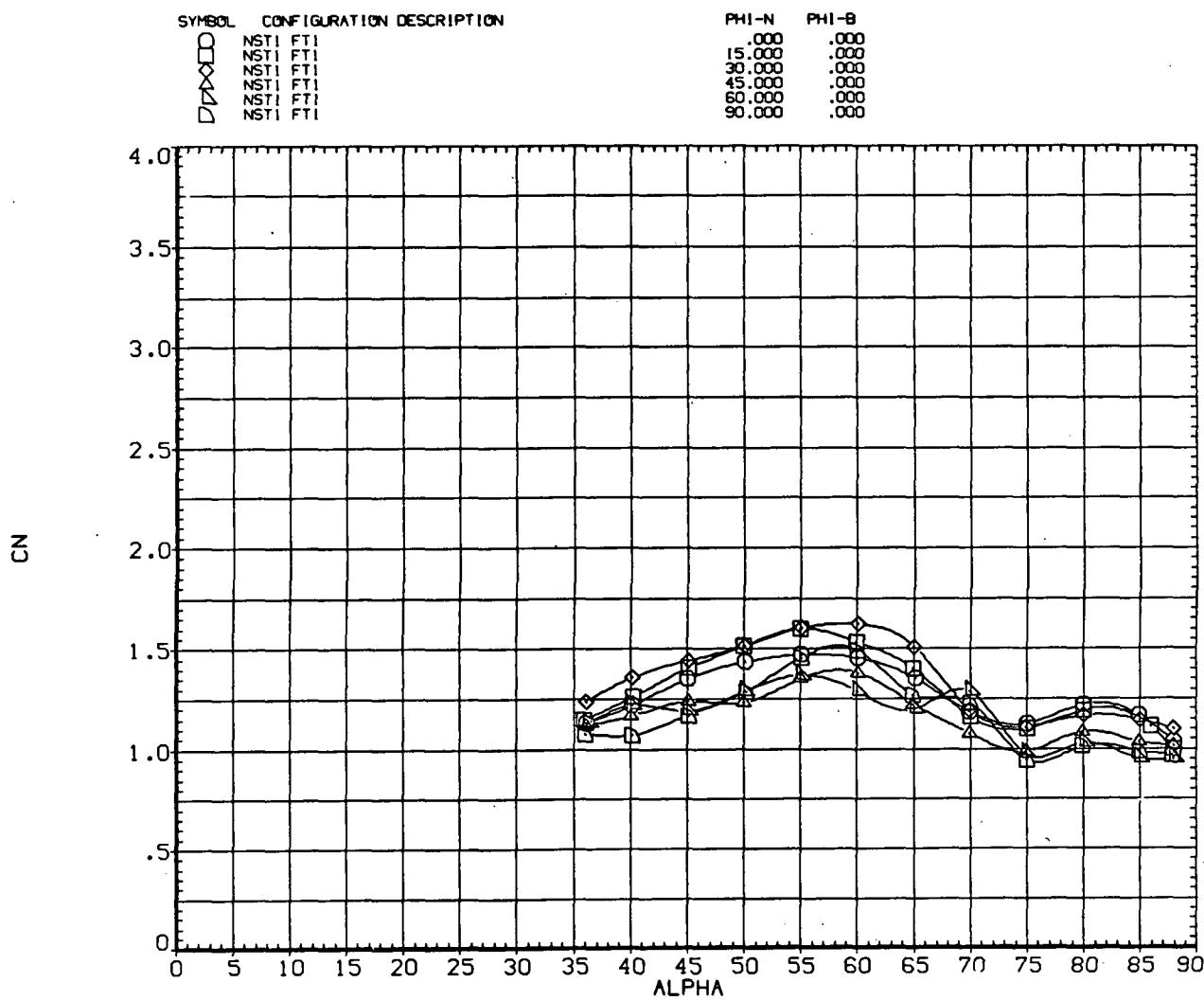
(b) C_N versus α.

Figure 22.– Continued.
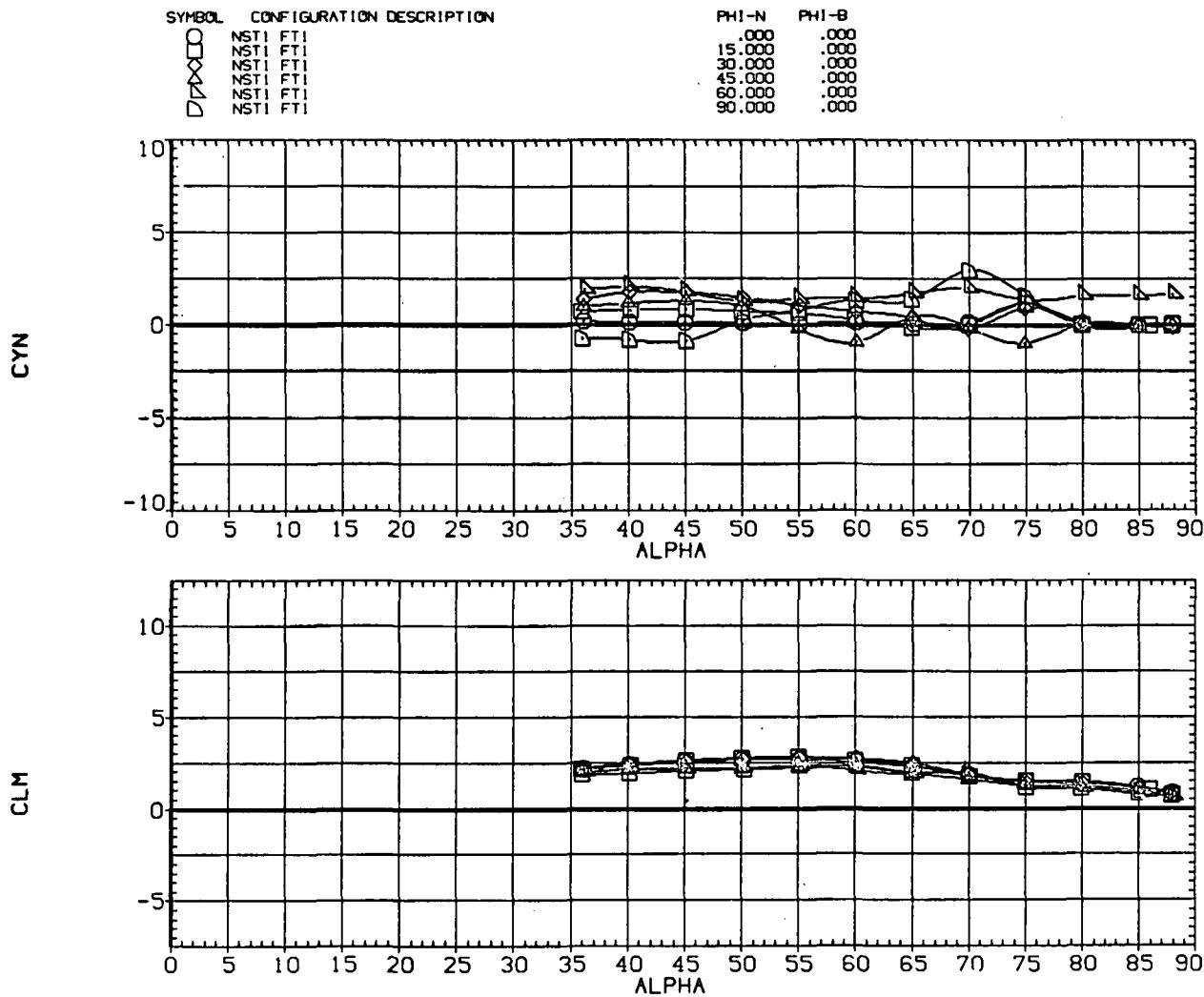
(c) C_n and C_m versus α.

Figure 22.– Concluded.
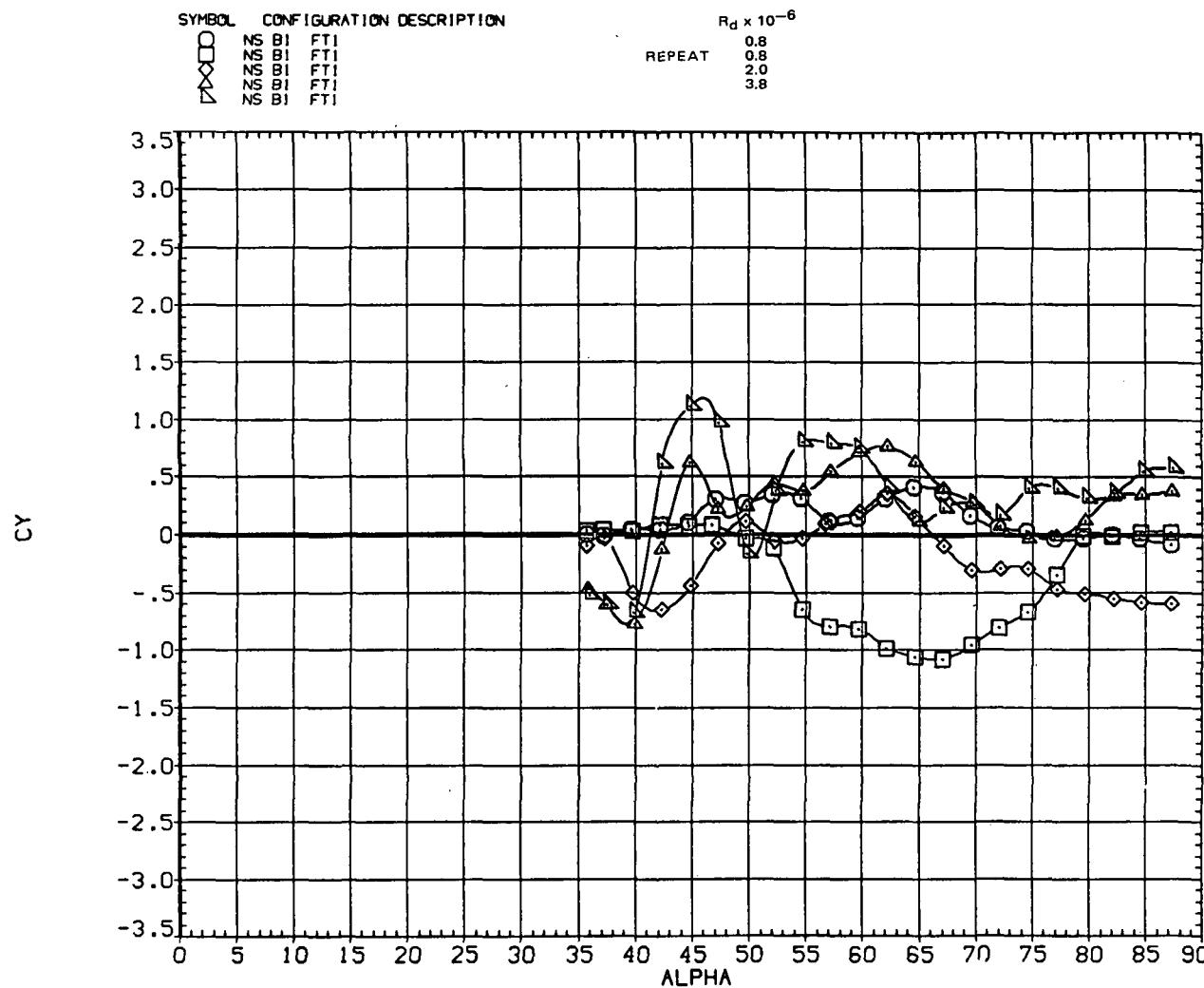
(a) C_Y versus α.

Figure 23.— Effect of nose boom; $M = 0.25, R_d = 0.8 \times 10^6$.

SYMBOL	CONFIGURATION DESCRIPTION			$R_d \times 10^{-6}$
⊖	NS	B1	FT1	0.8
⊟	NS	B1	FT1	REPEAT 0.8
◇	NS	B1	FT1	2.0
△	NS	B1	FT1	3.8
△	NS	B1	FT1	

(b) C_N versus α.

Figure 23.– Continued.

SYMBOL   CONFIGURATION DESCRIPTION $R_d \times 10^{-6}$

NS B1 FT1   0.8
NS B1 FT1   REPEAT   0.8
NS B1 FT1   2.0
NS B1 FT1   3.8
NS B1 FT1
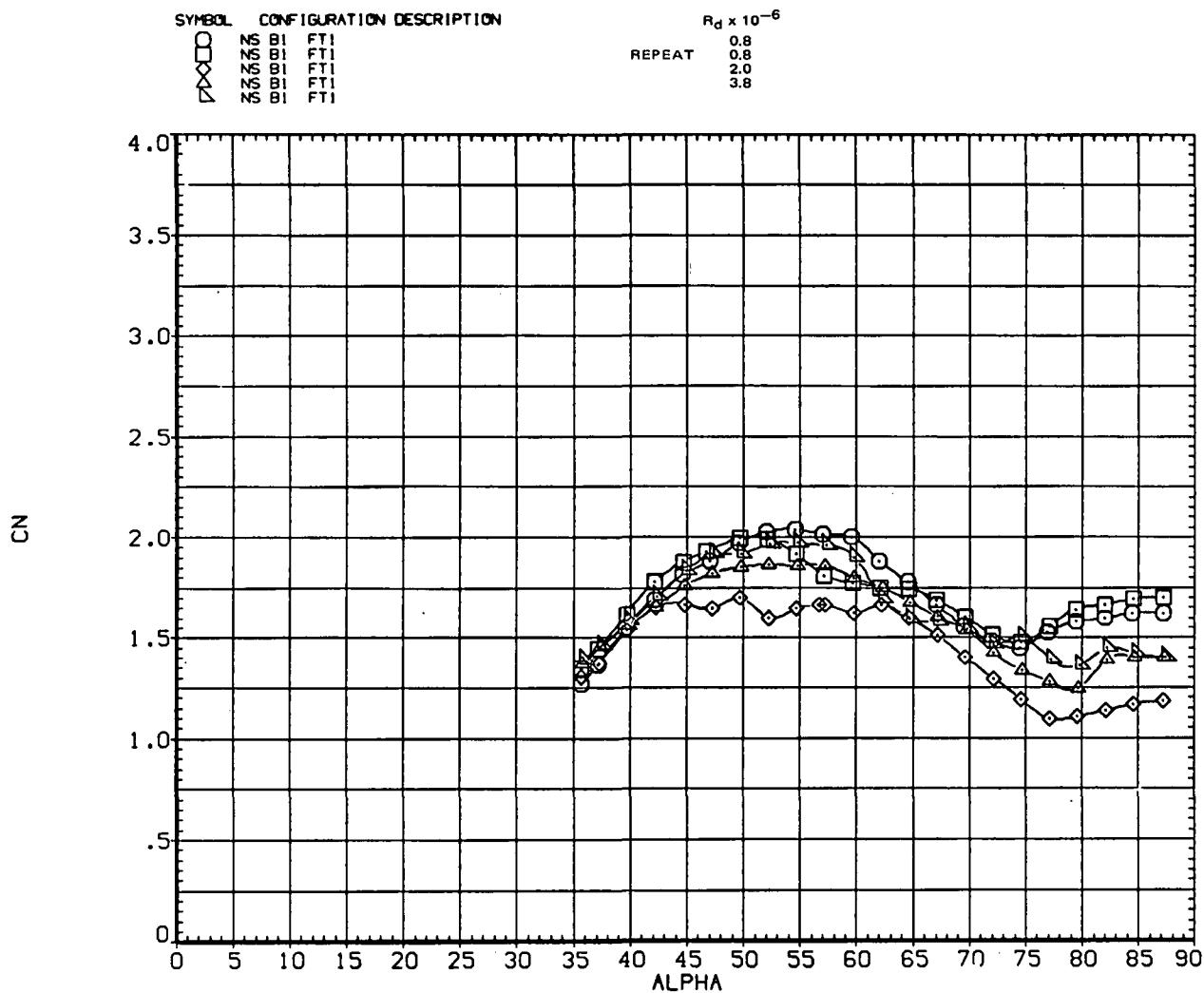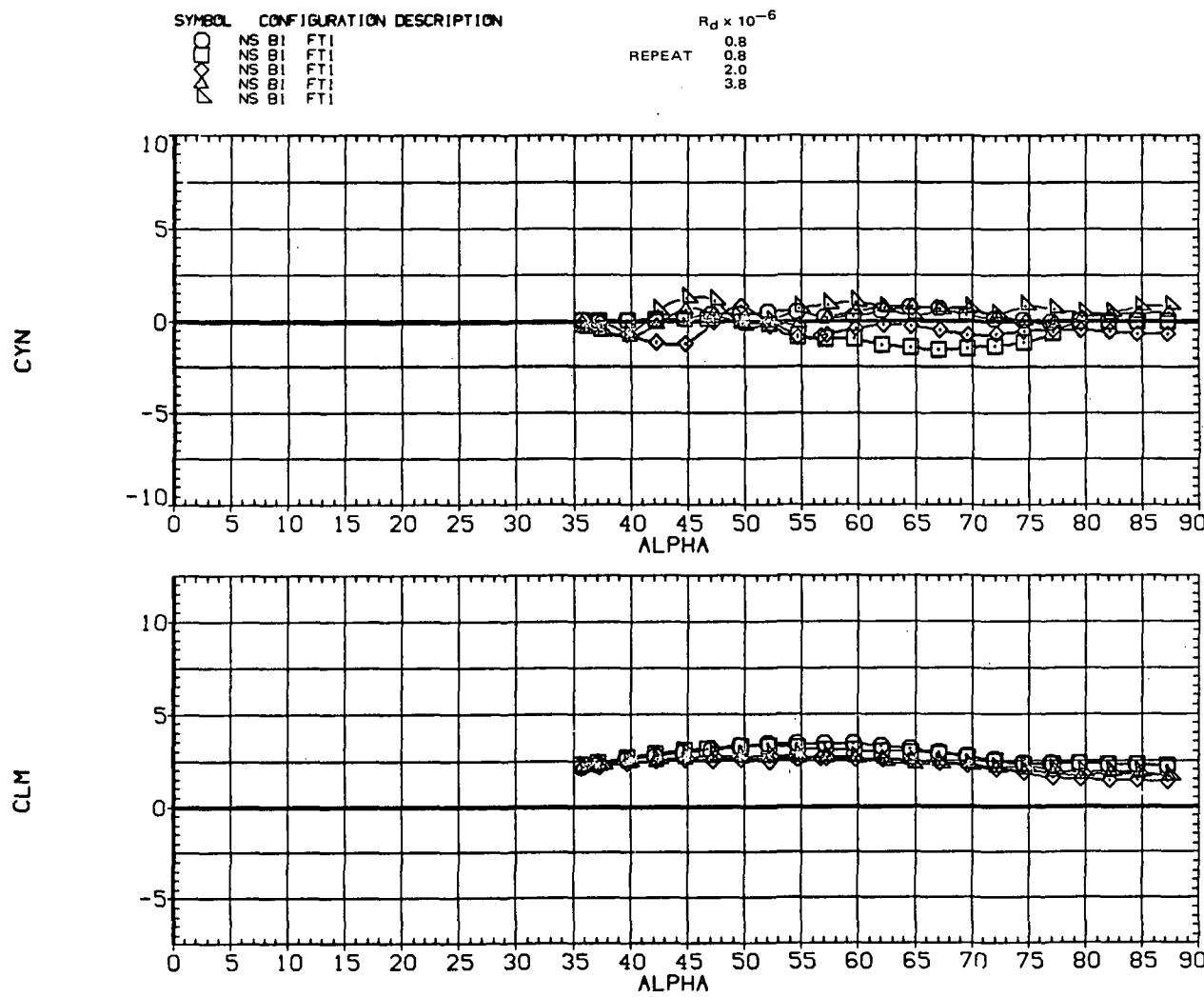
(c) C_n and C_m versus α.

Figure 23.– Concluded.

(a) C_Y versus α.
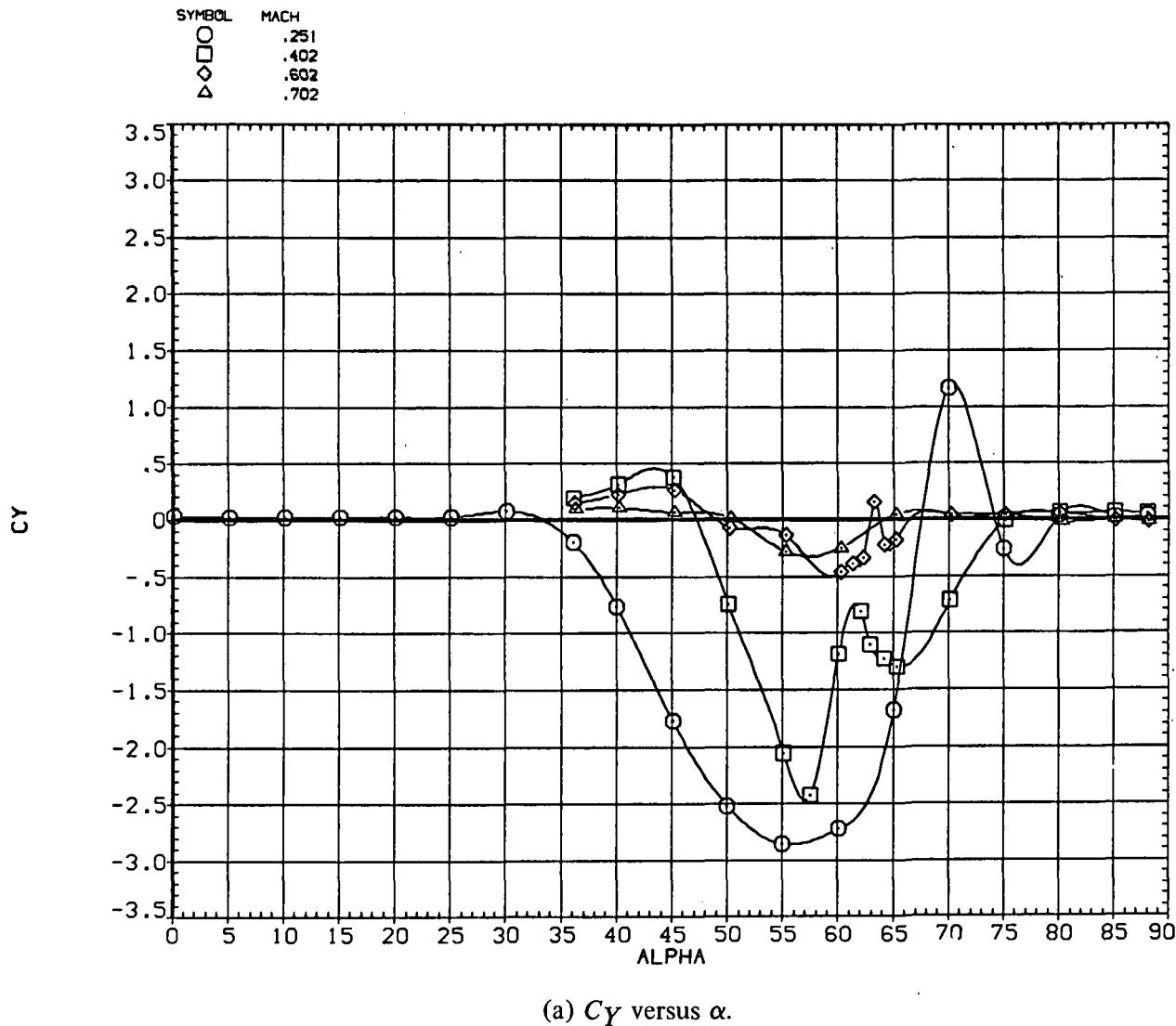
Figure 24.– Effect of Mach number; $R_d = 0.8 \times 10^6$.
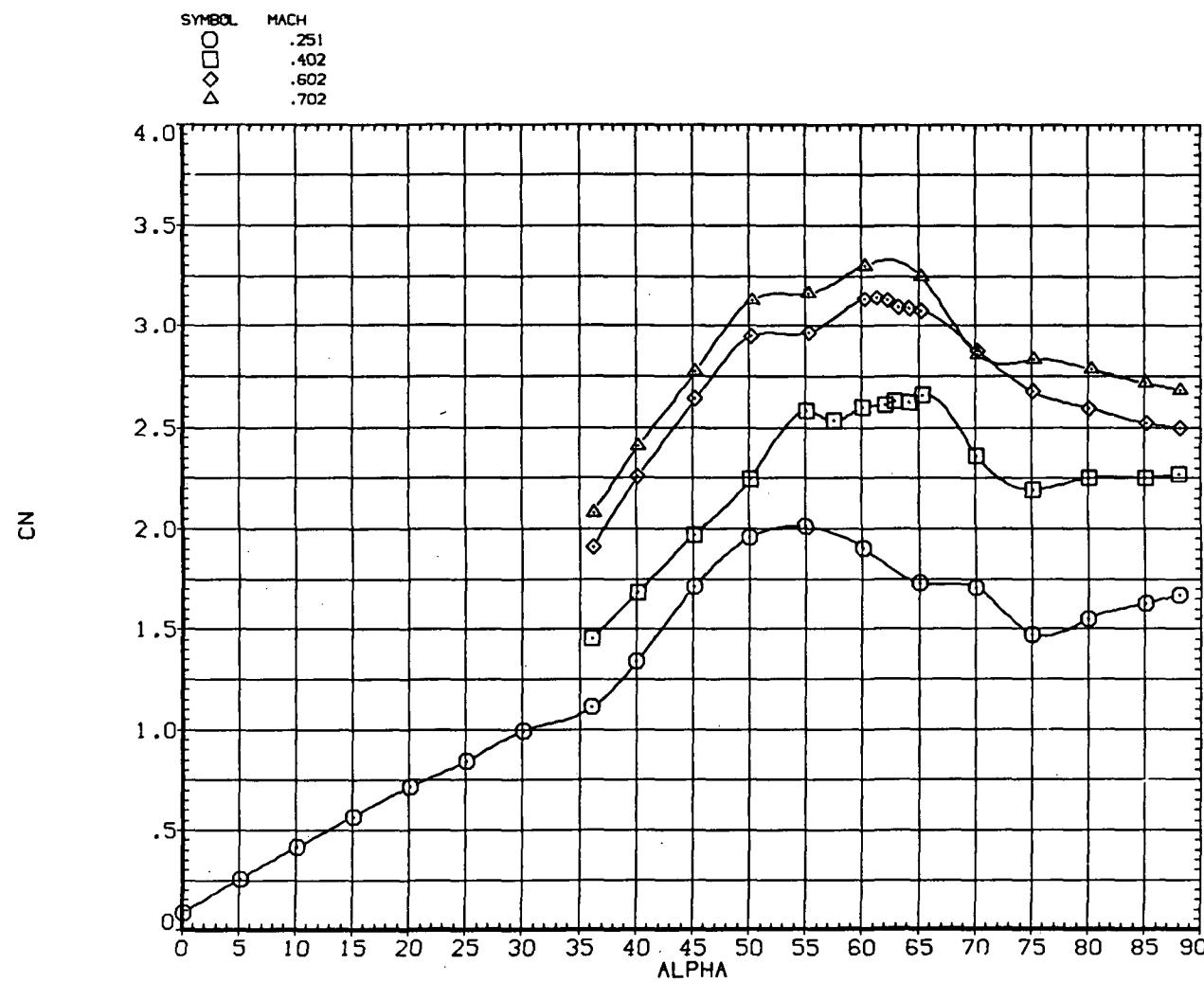
(b) C_N versus α.

Figure 24.– Continued.

(c) $|C_Y|/C_N$ and $C_R - C_N$ versus α.

Figure 24.– Continued.

SYMBOL   MACH
○   .251
□   .402
◇   .602
△   .702

(d) CP_R and Ψ versus α.
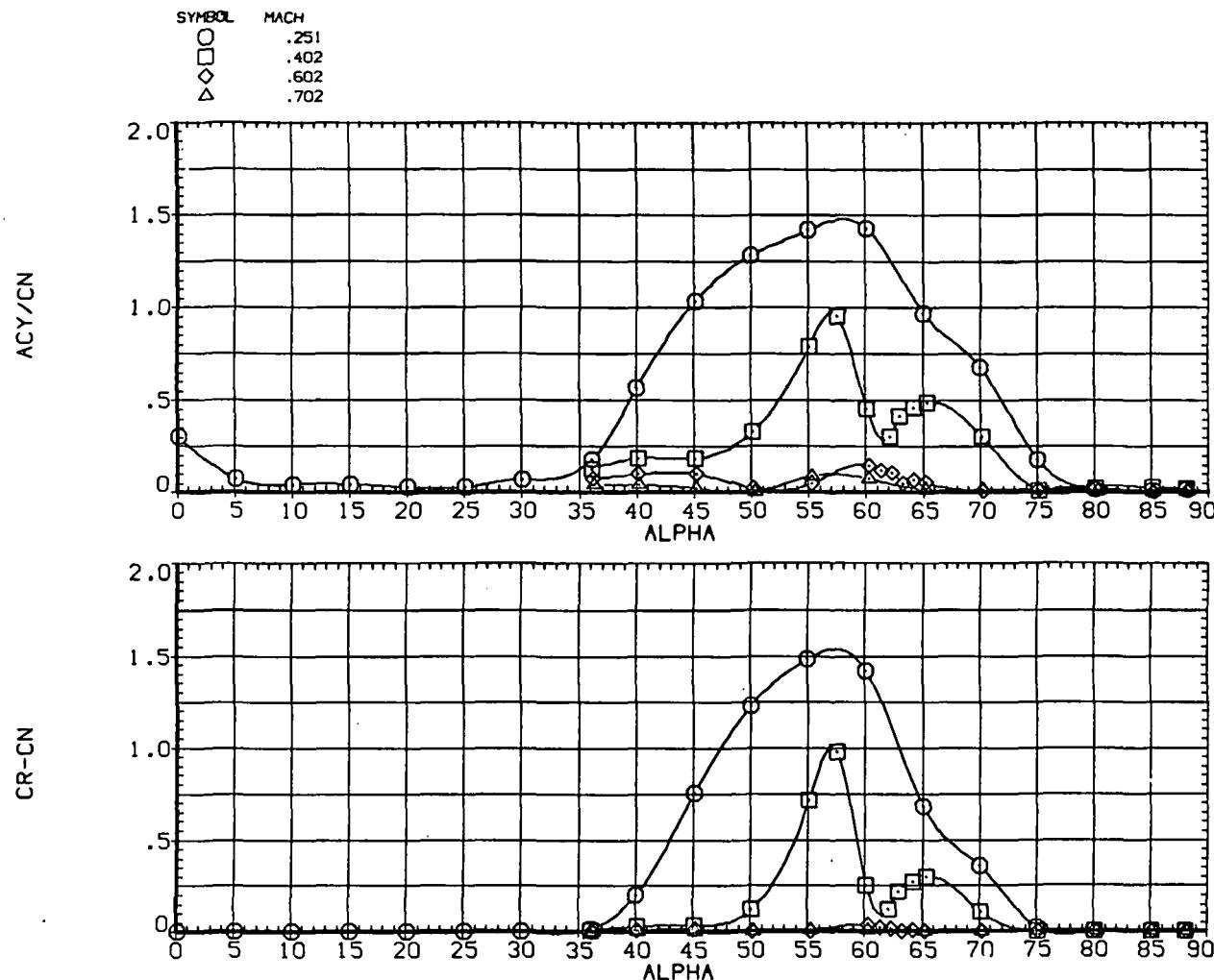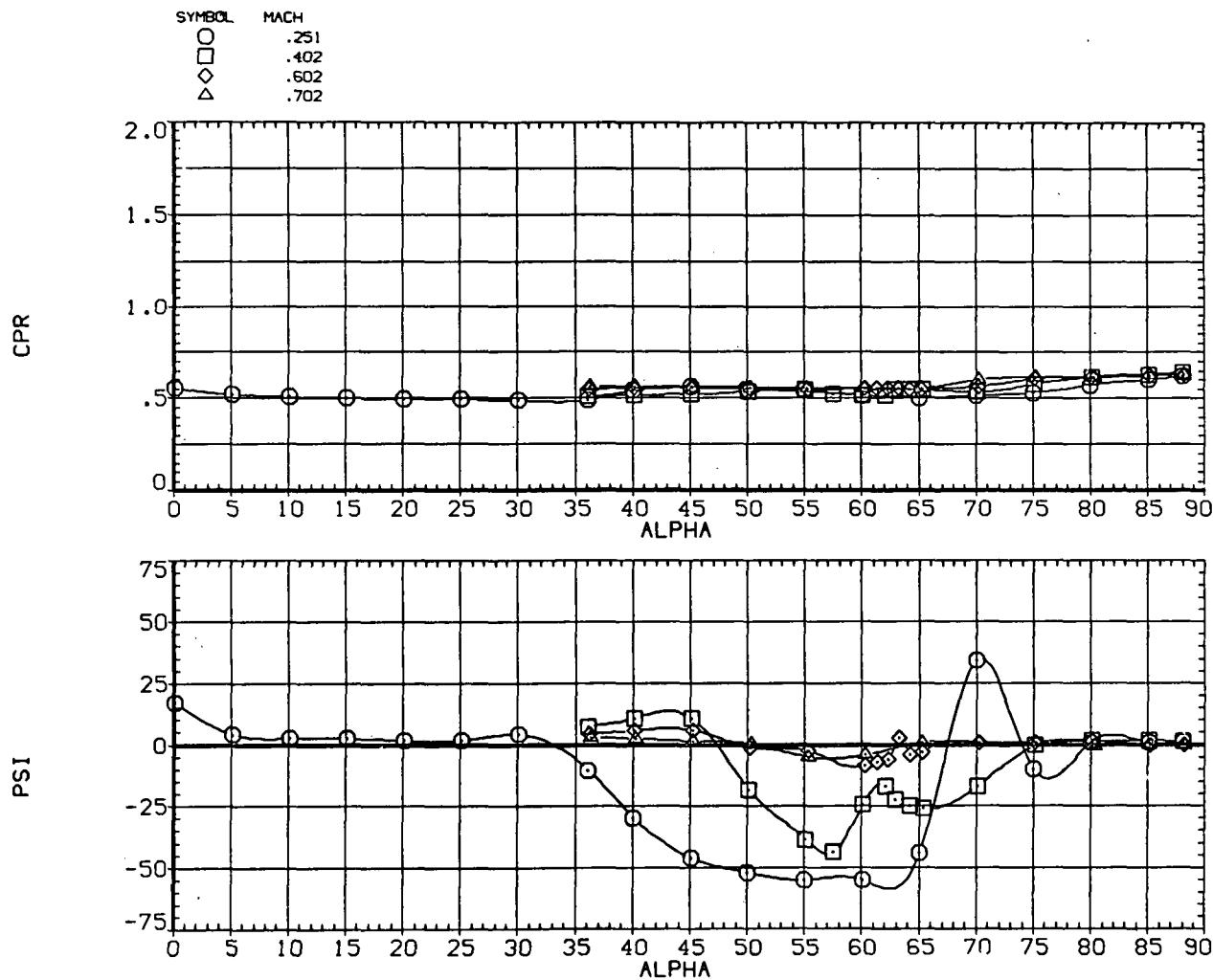
Figure 24.– Continued.
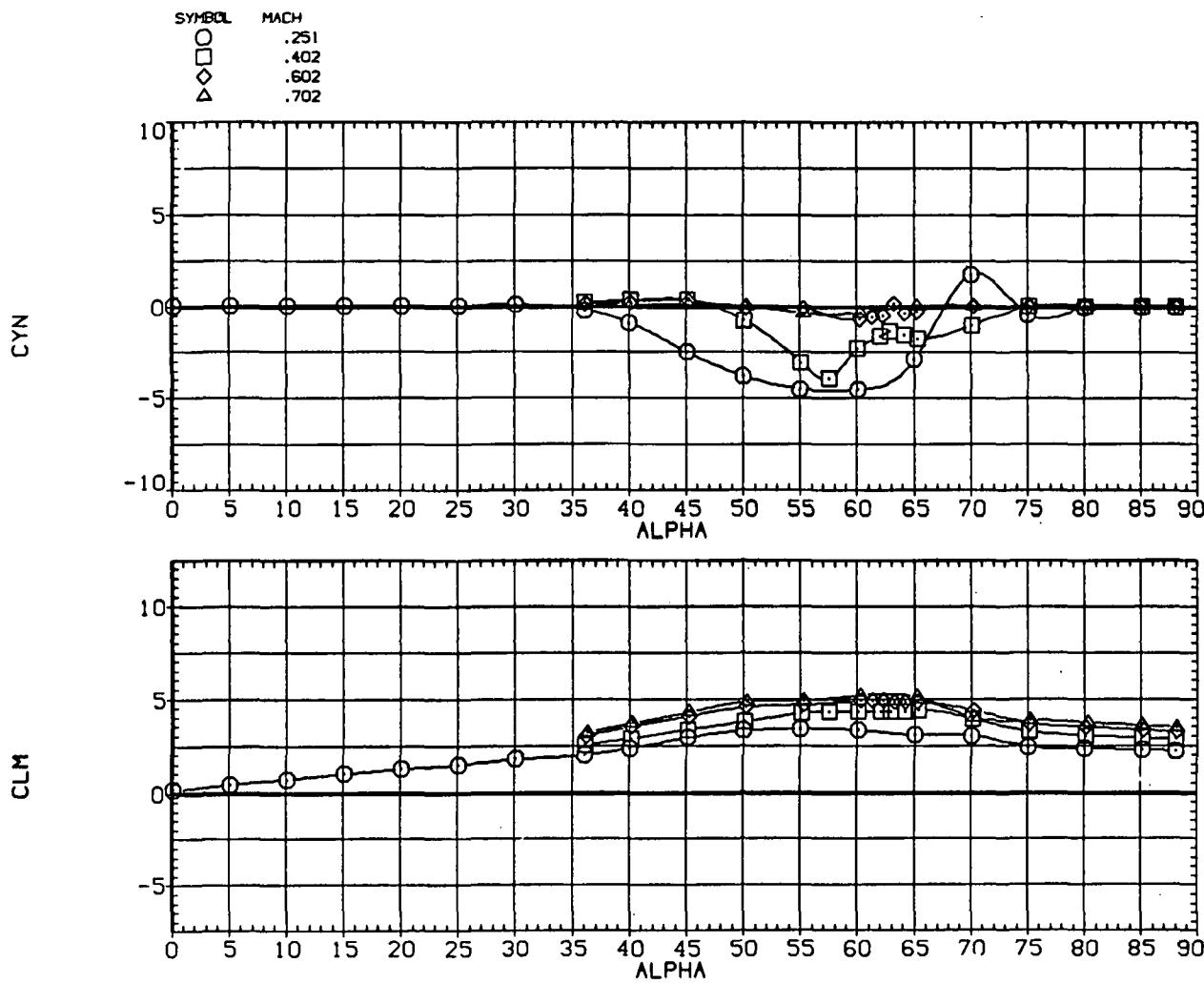
(e) C_n and C_m versus α.

Figure 24.– Continued.

(f) $C_{m,R}$ versus α.
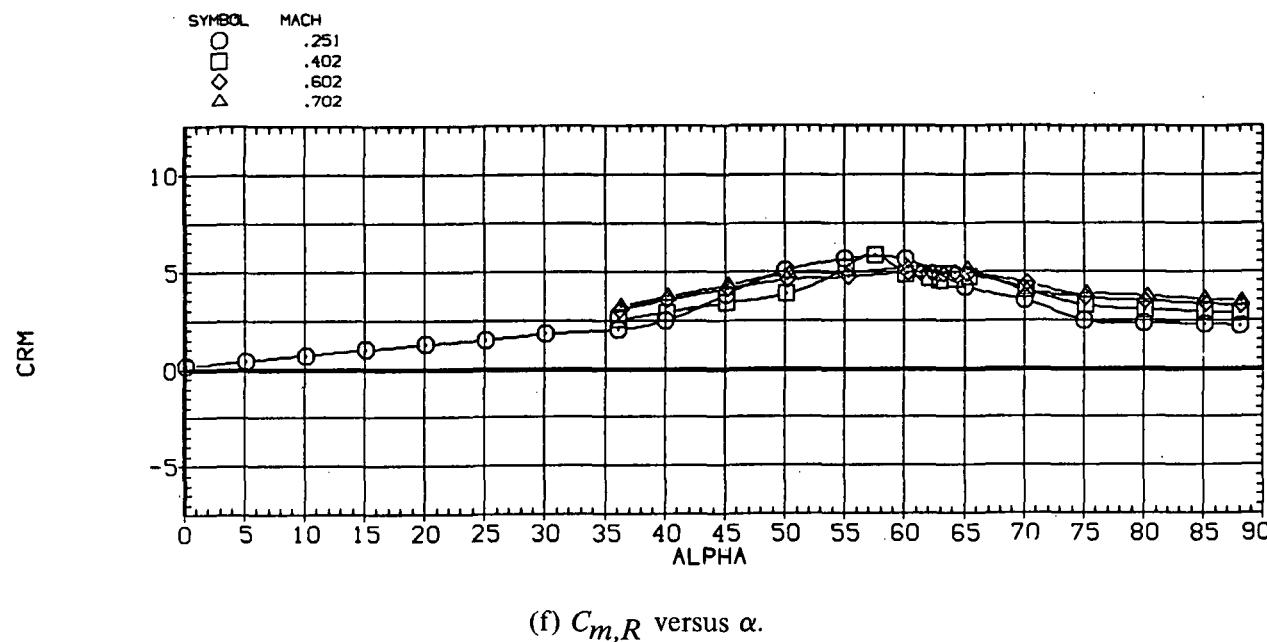
Figure 24.– Continued.

(g) $C_{p,b}$ and C_{AF} versus α.

Figure 24.— Concluded.

SYMBOL	CONFIGURATION DESCRIPTION	$R_d \times 10^{-6}$
	NS FT1 AA	0.3
	NS FT1 AA	0.8
	NS FT1 AA	1.1
	NS FT1 AA	2.0
	NS FT1 AA	3.0
	NS FT1 AA	3.8
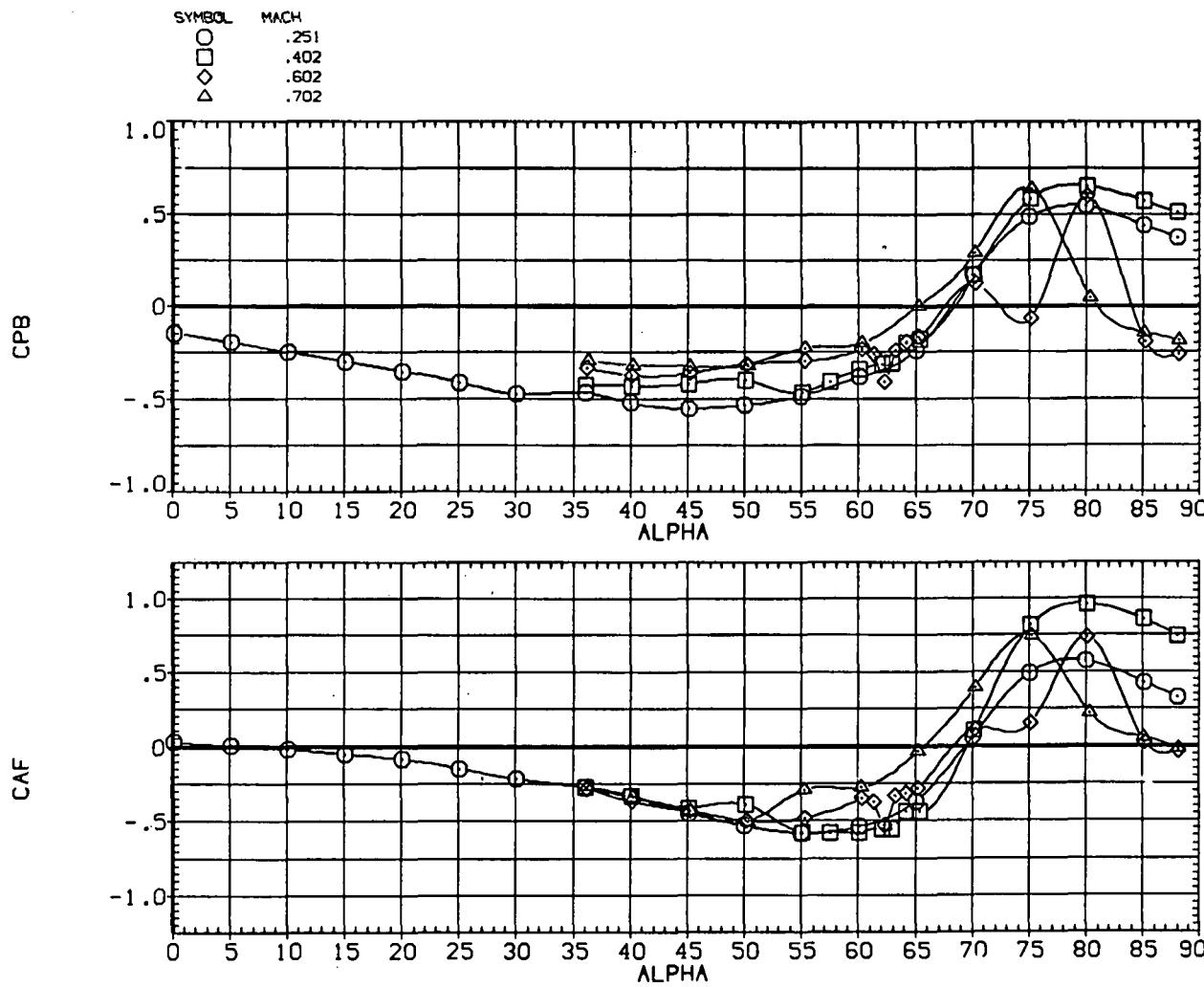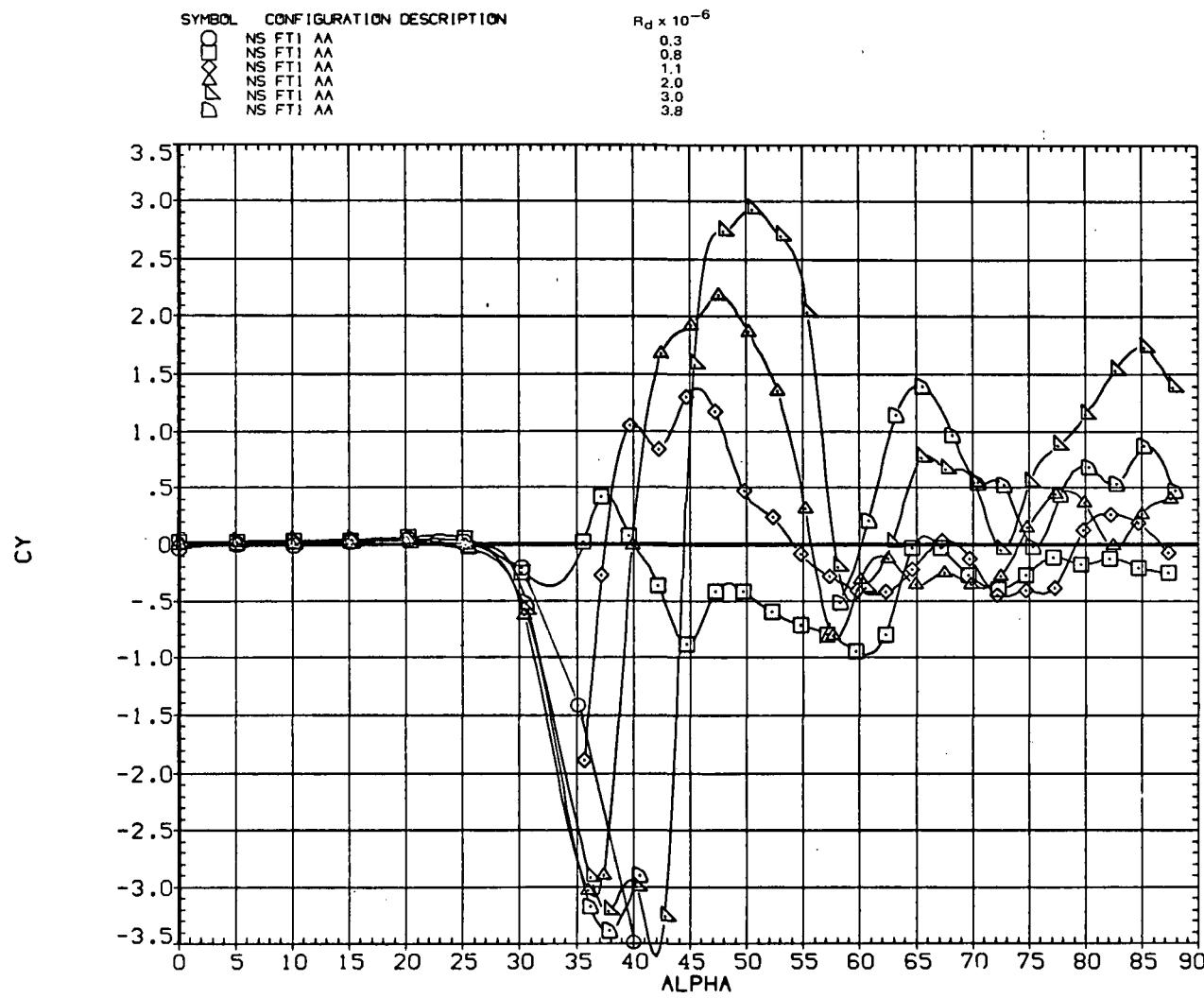
(a) C_Y versus α.

Figure 25.— Forebody with afterbody: effect of Reynolds number; $M = 0.25$.

(b) C_N versus α.

Figure 25.– Continued.

SYMBOL   CONFIGURATION DESCRIPTION $R_d \times 10^{-6}$

SYMBOL		CONFIGURATION DESCRIPTION	$R_d \times 10^{-6}$
○	NS FTI AA		0.3
□	NS FTI AA		0.8
◇	NS FTI AA		1.1
△	NS FTI AA		2.0
△	NS FTI AA		3.0
▽	NS FTI AA		3.8
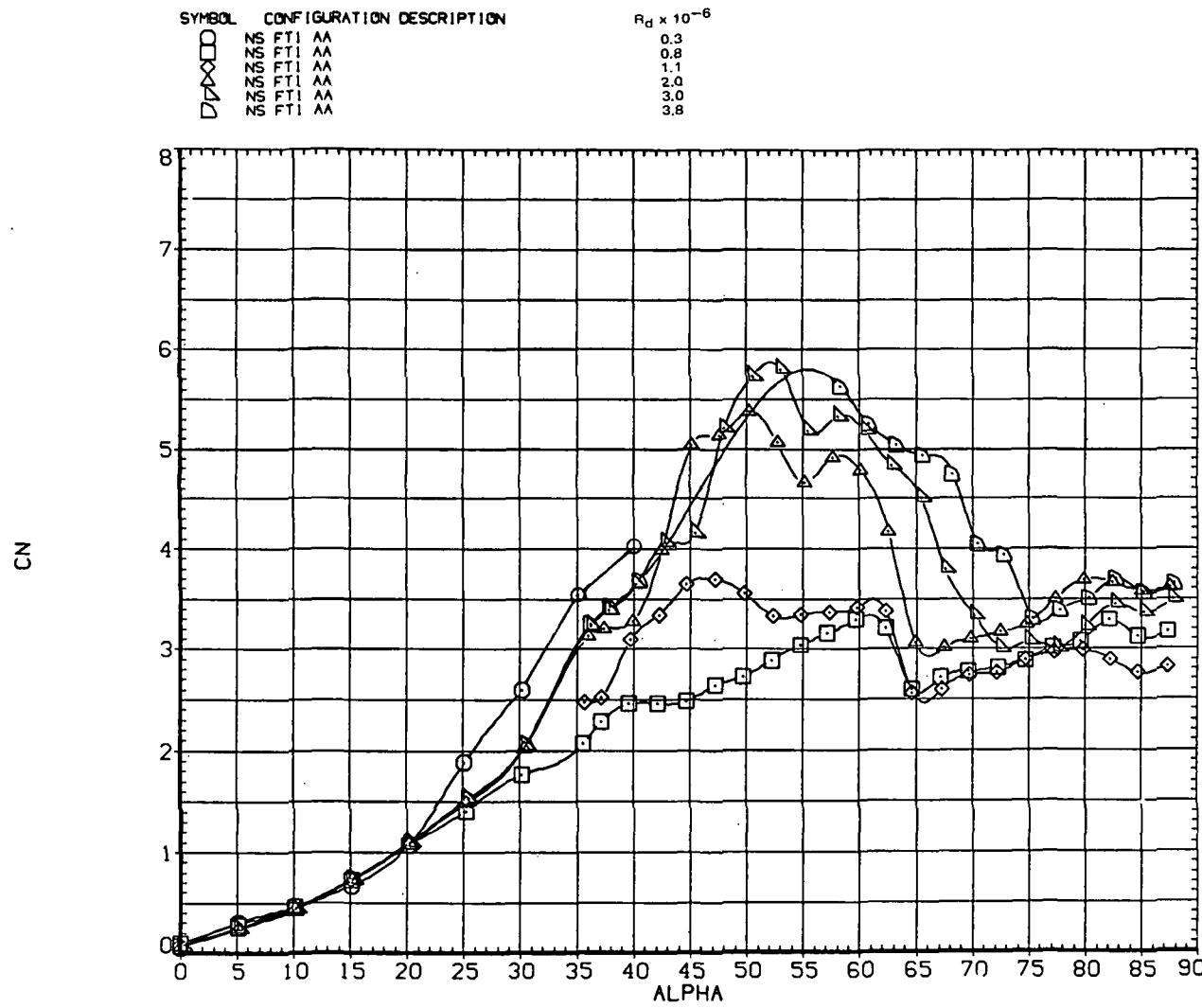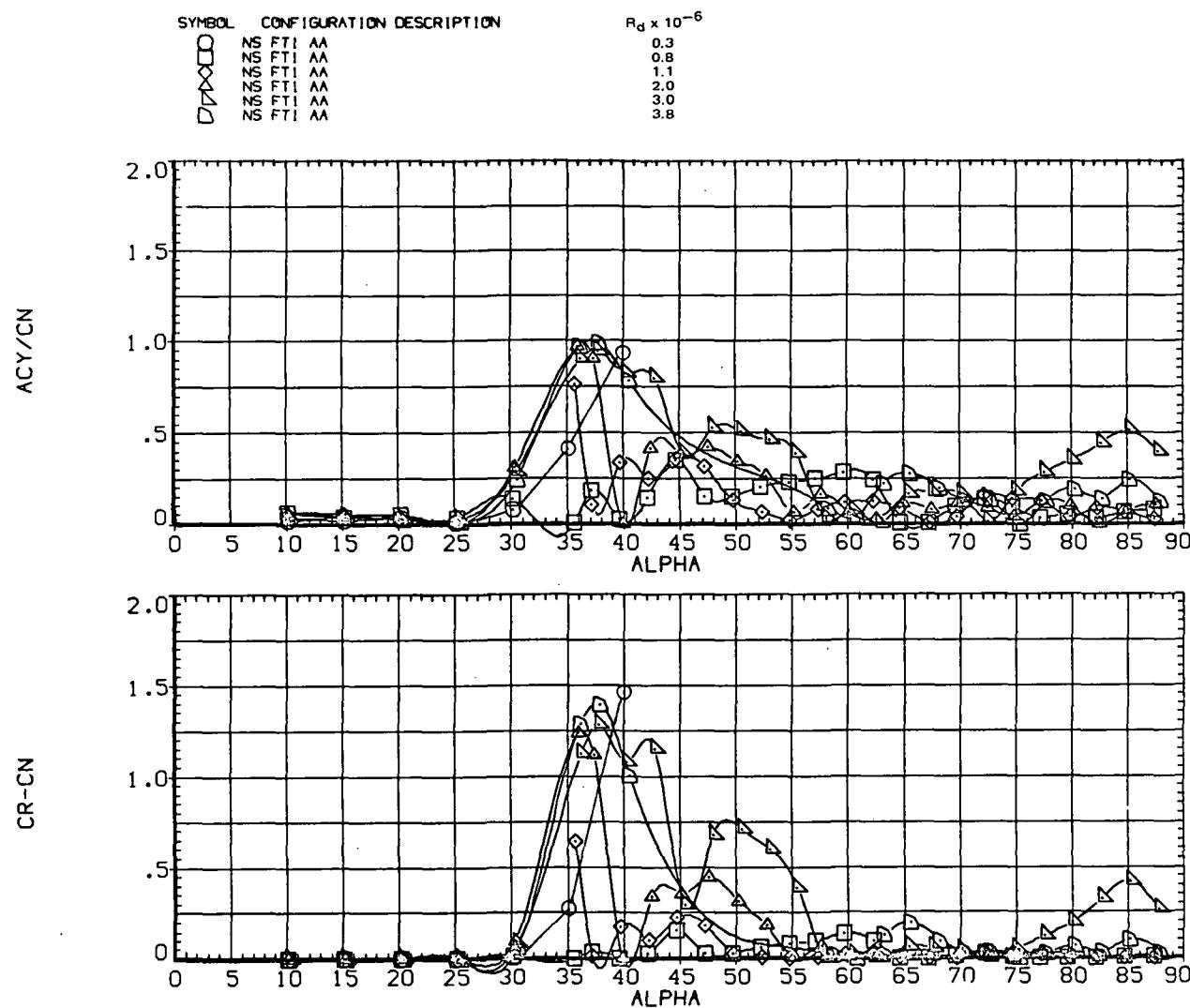
(c) $|C_Y|/C_N$ and $C_R - C_N$ versus α.

Figure 25.— Continued.

(d) CP_R and Ψ versus α.

Figure 25.– Continued.

SYMBOL	CONFIGURATION DESCRIPTION	$R_d \times 10^{-6}$
⬭	NS FT1 AA	0.3
⬜	NS FT1 AA	0.8
⨂	NS FT1 AA	1.1
△	NS FT1 AA	2.0
△	NS FT1 AA	3.0
◁	NS FT1 AA	3.8
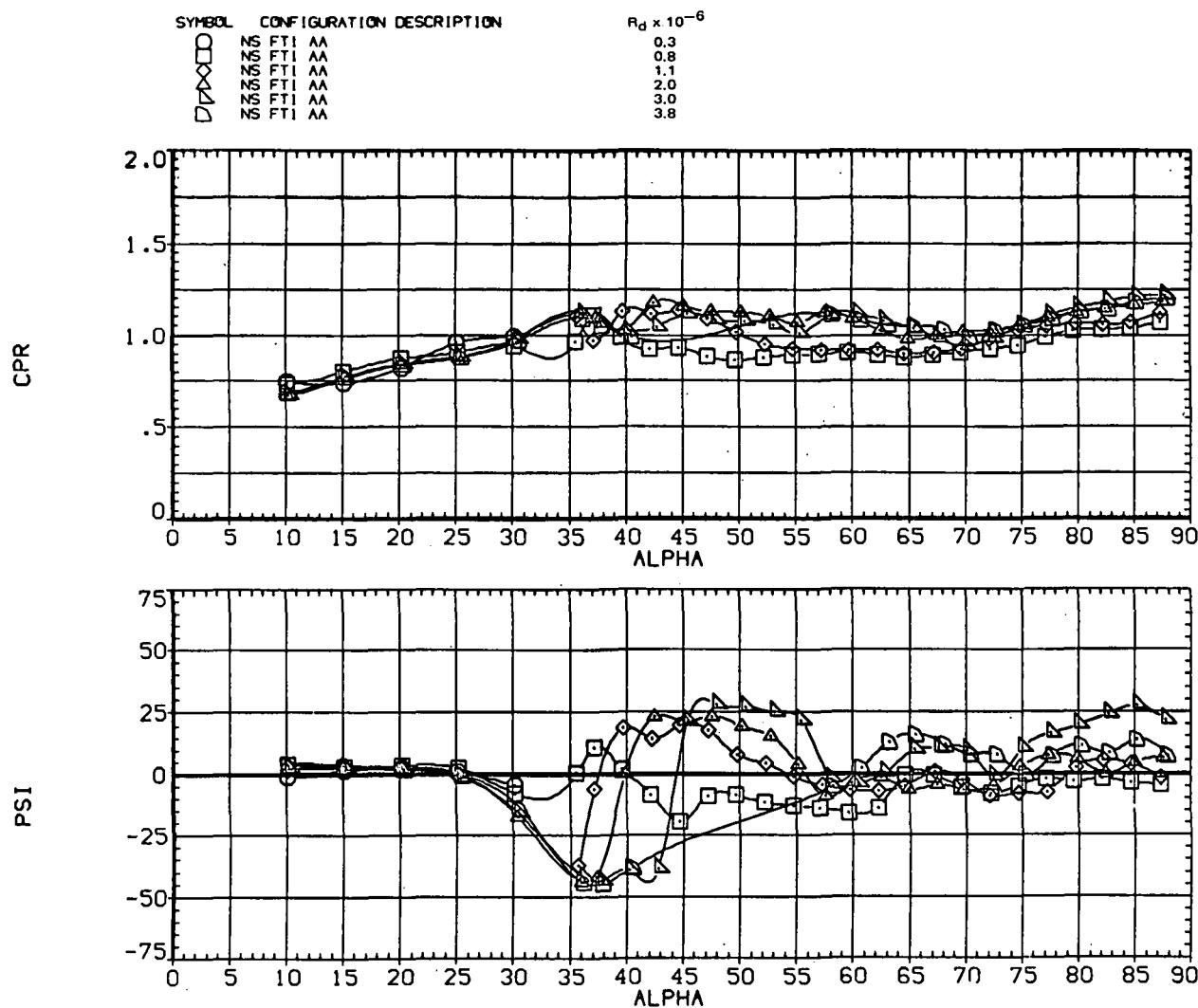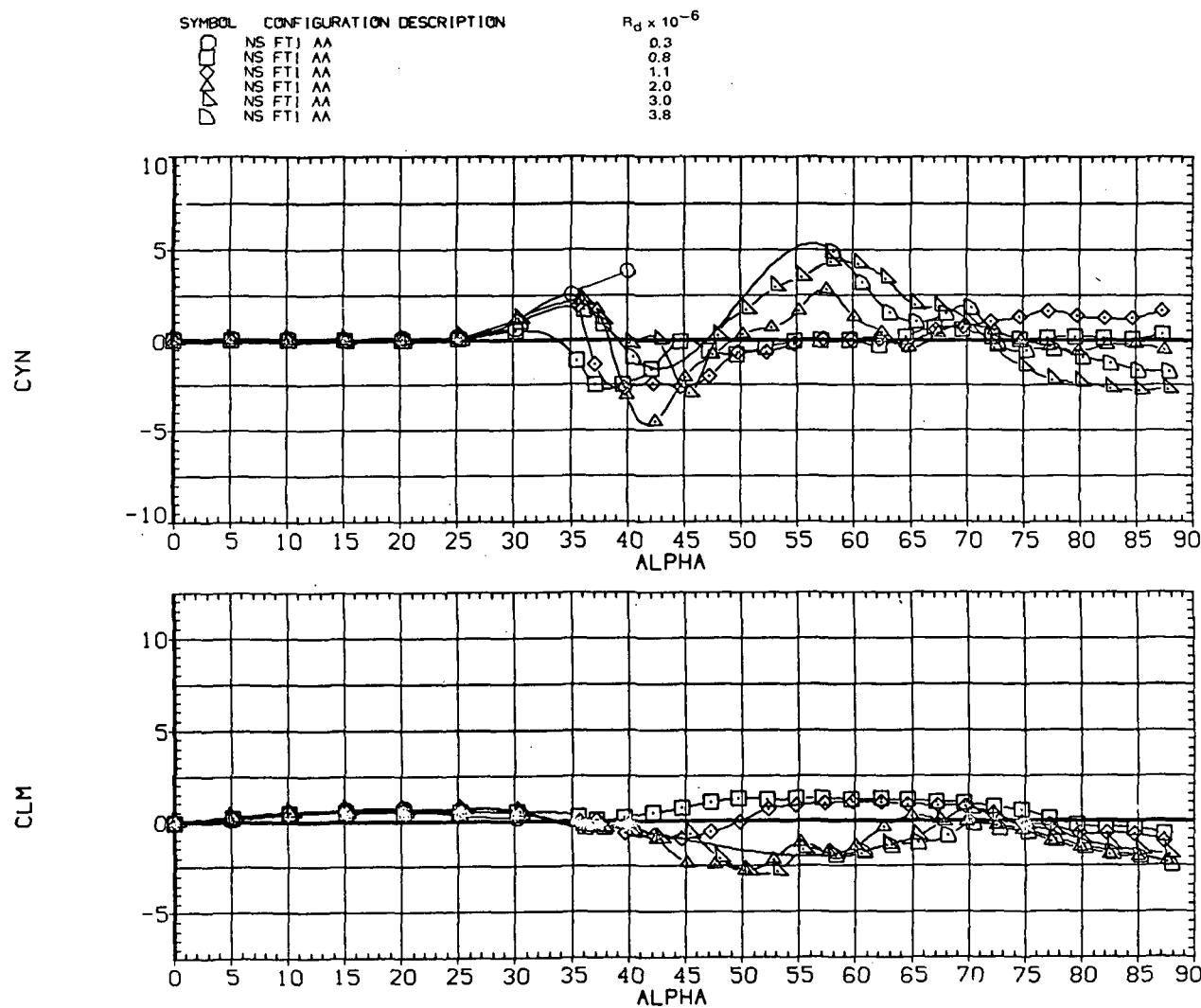
(e) C_n and C_m versus α.

Figure 25.– Continued.

(f) $C_{m,R}$ versus α.

Figure 25.— Continued.

SYMBOL	CONFIGURATION DESCRIPTION	$R_d \times 10^{-6}$
⊙	NS FT1 AA	0.3
⊟	NS FT1 AA	0.8
⊠	NS FT1 AA	1.1
◇	NS FT1 AA	2.0
△	NS FT1 AA	3.0
▷	NS FT1 AA	3.8

(g) C_{AF} versus α.

Figure 25.— Concluded.

SYMBOL	MACH
○	.100
□	.250
◇	.416
△	.622
◁	.723
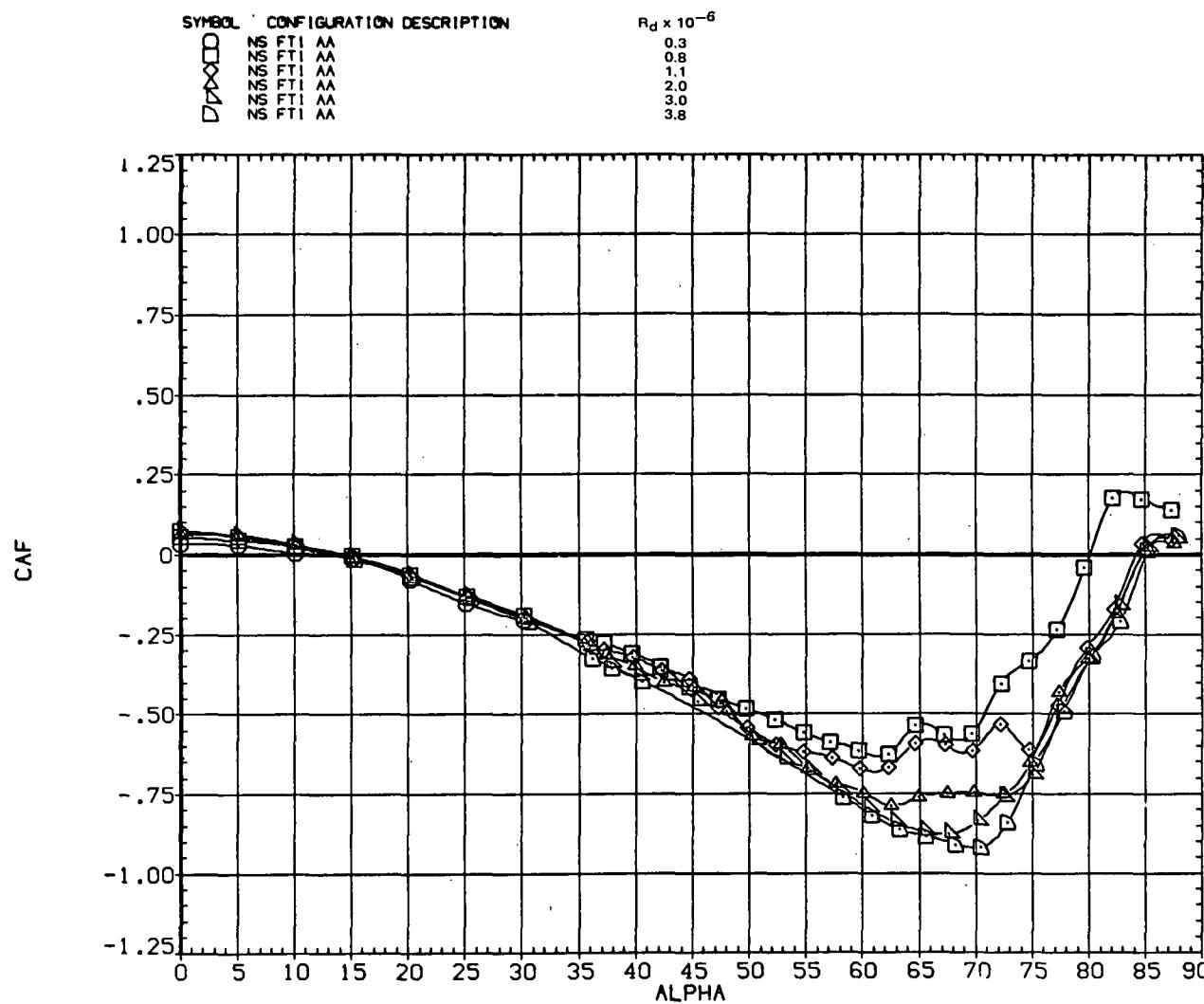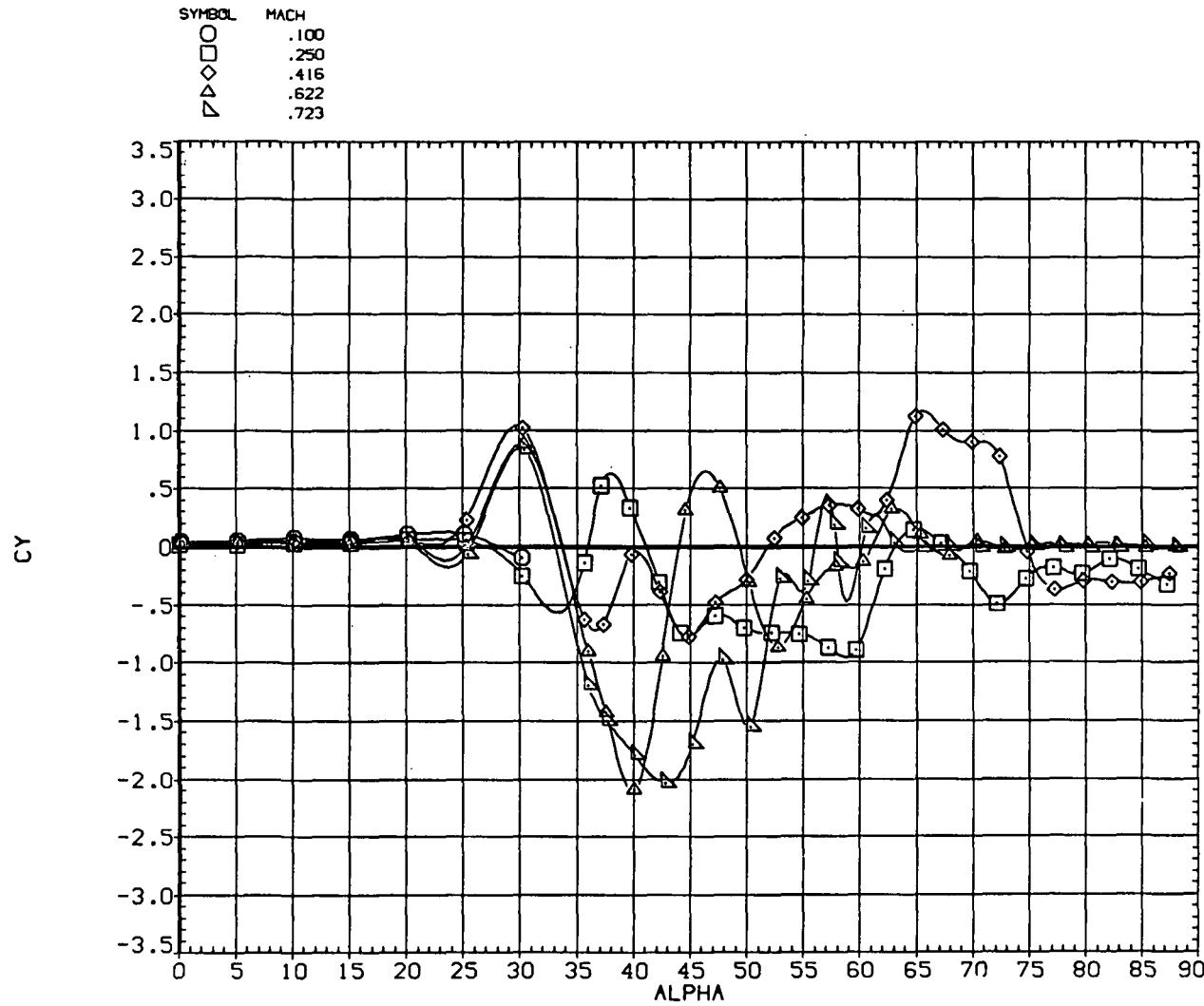
(a) C_Y versus α.

Figure 26.— Forebody with afterbody: effect of Mach number; $R_d = 0.8 \times 10^6$.

(b) C_N versus α.

Figure 26.– Continued.

SYMBOL MACH
○   .100
□   .250
◇   .416
△   .622
◁   .723
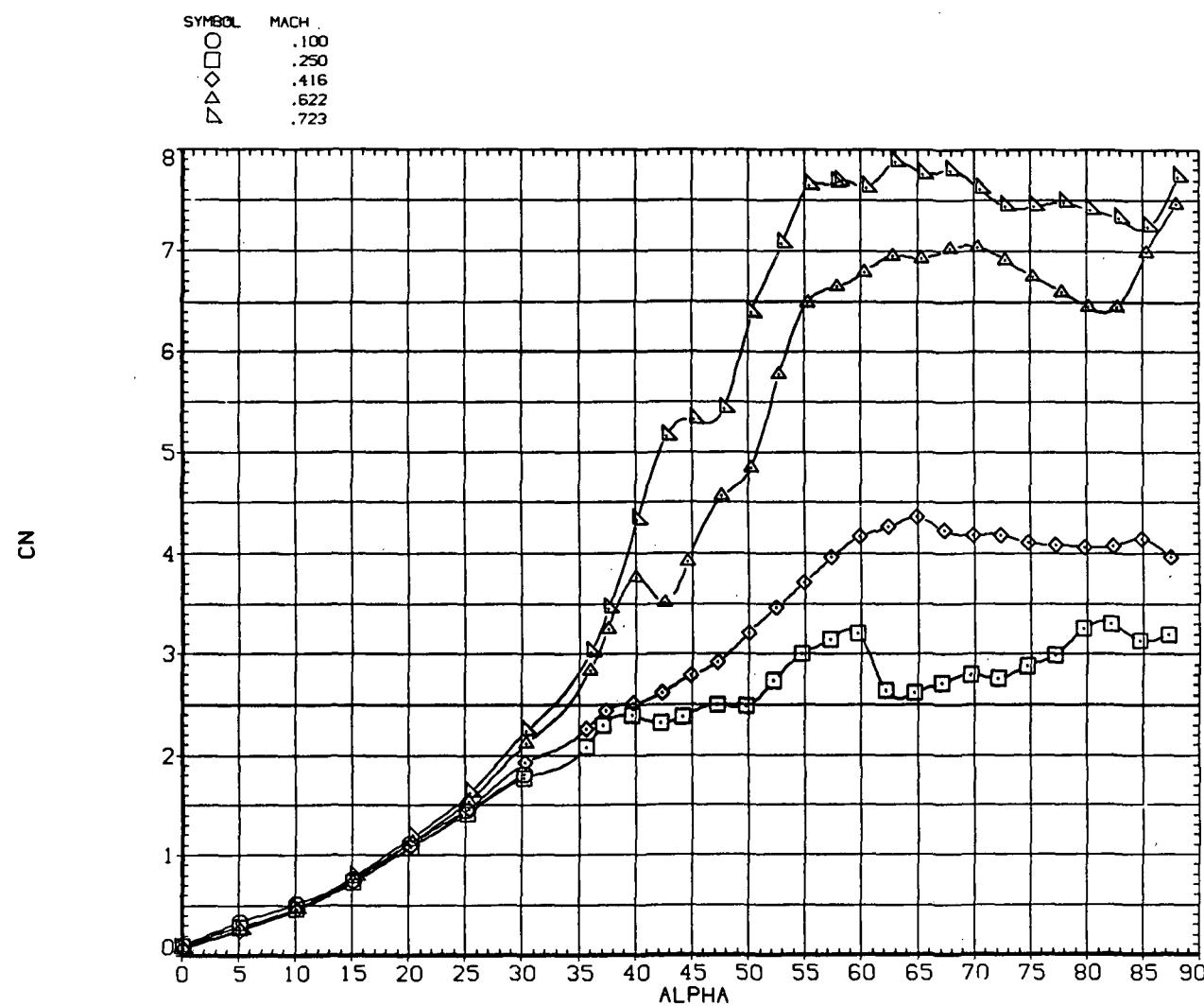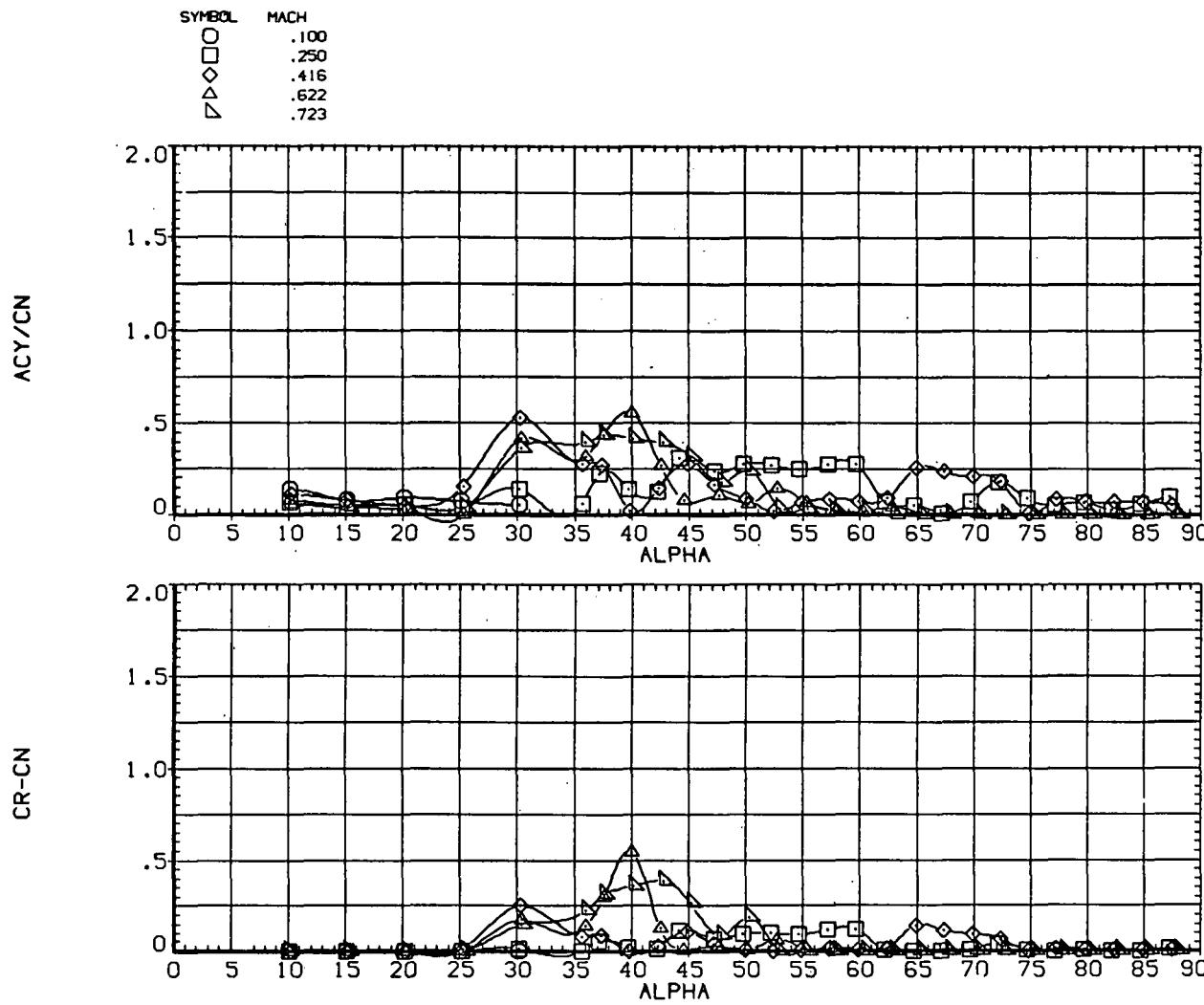
(c) $|C_Y|/C_N$ and $C_R - C_N$ versus α.

Figure 26.– Continued.

(d) CP_R and Ψ versus α.

Figure 26.– Continued.

(e) C_n and C_m versus α.
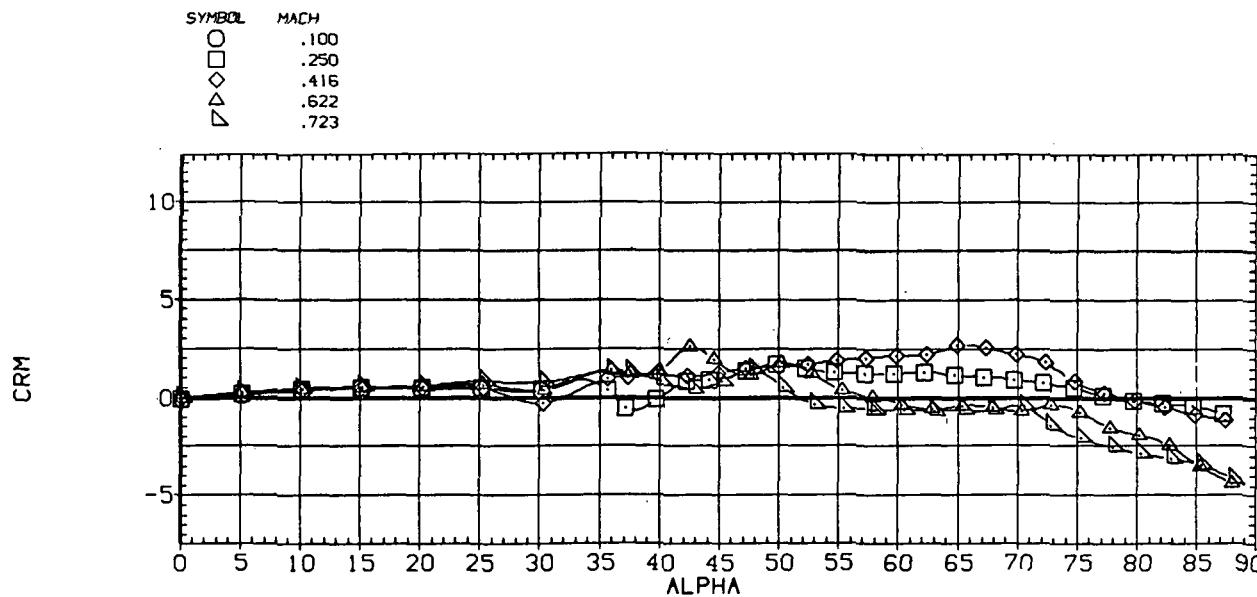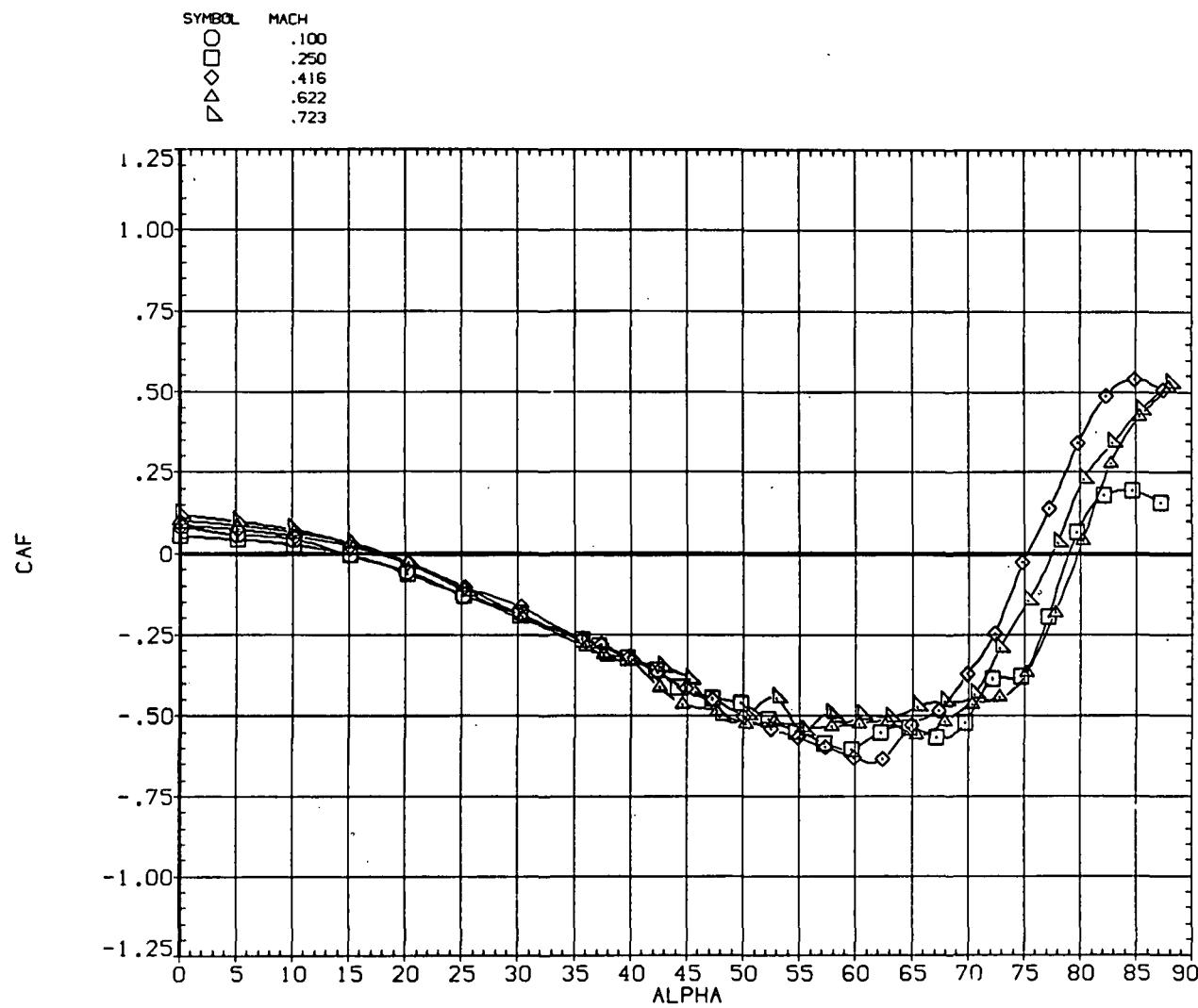
Figure 26.– Continued.

SYMBOL MACH
○   .100
□   .250
◇   .416
△   .622
◁   .723

(f) $C_{m,R}$ versus α.

Figure 26.– Continued.

SYMBOL	MACH
○	.100
□	.250
◇	.416
△	.622
◁	.723

(g) C_{AF} versus α.

Figure 26.— Concluded.

"The aeronautical and space activities of the United States shall be conducted so as to contribute . . . to the expansion of human knowledge of phenomena in the atmosphere and space. The Administration shall provide for the widest practicable and appropriate dissemination of information concerning its activities and the results thereof."
—NATIONAL AERONAUTICS AND SPACE ACT OF 1958

NASA SCIENTIFIC AND TECHNICAL PUBLICATIONS

TECHNICAL REPORTS: Scientific and technical information considered important, complete, and a lasting contribution to existing knowledge.

TECHNICAL NOTES: Information less broad in scope but nevertheless of importance as a contribution to existing knowledge.

TECHNICAL MEMORANDUMS: Information receiving limited distribution because of preliminary data, security classification, or other reasons. Also includes conference proceedings with either limited or unlimited distribution.

CONTRACTOR REPORTS: Scientific and technical information generated under a NASA contract or grant and considered an important contribution to existing knowledge.

TECHNICAL TRANSLATIONS: Information published in a foreign language considered to merit NASA distribution in English.

SPECIAL PUBLICATIONS: Information derived from or of value to NASA activities. Publications include final reports of major projects, monographs, data compilations, handbooks, sourcebooks, and special bibliographies.

TECHNOLOGY UTILIZATION PUBLICATIONS: Information on technology used by NASA that may be of particular interest in commercial and other non-aerospace applications. Publications include Tech Briefs, Technology Utilization Reports and Technology Surveys.

Details on the availability of these publications may be obtained from:

SCIENTIFIC AND TECHNICAL INFORMATION OFFICE

NATIONAL AERONAUTICS AND SPACE ADMINISTRATION
Washington, D.C. 20546